Towards Multi-Scale Transport of Sharp Plumes

Sakina Takache

To cite this version:

Sakina Takache. Towards Multi-Scale Transport of Sharp Plumes. Numerical Analysis [cs.NA]. Institut Polytechnique de Paris, 2021. English. NNT : 2021IPPAX123 . tel-03631013

HAL Id: tel-03631013
https://theses.hal.science/tel-03631013

Submitted on 5 Apr 2022

NNT : 2021IPPAX123

Towards Multi-Scale Transport of Sharp Plumes

Thèse de doctorat de l'Institut Polytechnique de Paris
préparée à l'Ecole Polytechnique

École doctorale n°626 École doctorale de l'Institut Polytechnique de Paris (ED IP Paris)
Spécialité de doctorat: Mécanique des fluides et des solides, acoustique

Thèse présentée et soutenue à Palaiseau, le 6 décembre, 2021, par

MME SAKINA TAKACHE

Composition du Jury :

Riwal Plougonven Professeur, École Polytechnique (LMD)	Président
Yelva Roustan Chargé de recherche, École des Ponts Paristech - EDF (CEREA)	Rapporteur
Frédéric Chevallier Directeur de recherche, Institut Pierre-Simon Laplace (LSCE)	Rapporteur
Christine Lac Directrice de recherche, Météo-France (CNRM)	Examinatrice
Emmanuel Audusse Maître de conférences, Université Sorbonne Paris Nord (LAGA)	Examinateur
Thomas Dubos Professeur, École Polytechnique (LMD)	Directeur de thèse
Sylvain Mailler Ingénieur des Ponts, des Eaux et Forêts, École des Ponts ParisTech (LMD)	Co-encadrant de thèse

Thèse de doctorat

Dedication

إلى كلّ يدٍ عتيقةٍ لم تساوم على مفتاح الدار، دارها في فلسطين الحبيبة

To every wrinkled hand still carrying a key to an unforgotten home in Palestine

Acknowledgments

I would like to acknowledge, first and foremost, my mother and father for their unfaltering support for my education over the course of the past 23 academic years. They were there for every moment, in every detail, and at each milestone. Truly, mom and dad,

أنتما الأصل وأنا الفرع، ولولا سقيا الجذع لم يزهر الغصن

Second, I thank my daughter, Fatima, for relentlessly reminding me that doctoral work is a piece of cake. Motherhood is the real rocket science. When you read this someday, Fatima, know that you taught me more than any doctoral program ever could have, and that I prize the equilibrium you (and your potential siblings) endow my life with more than any successful career without a family.

Third, Ali: The acknowledgment page is not enough. Words are not enough, in any language. I love you.

My late grandfather, Jiddo Naïm: you carried me on your shoulders throughout the whole thesis. Until we meet again, oh light of my eyes, rest in peace.

Saja (unfortunately for you, they're using my full name for the thesis, not just S. Takache), Alaa, and Kumayl: please note that the calculations presented in this work were made possible thanks to the use of the ClimServ computational center of Institut Pierre-Simon Laplace (IPSL) and the computational resources at TGCC and IDRIS obtained under grant GENCI N° 10274. I will always be the most annoying one.

On the professional side, I greatly acknowledge the efforts of Professor Thomas Dubos during the past 4 years, from the guidance preceding my enrolment, until the final publication of this thesis. Prof, I learned much from the details of your demeanour, in handling academic issues and time constraints with exactitude, while remaining liberal and extraordinarily kind. A similar acknowledgment goes out to Dr. Sylvain Mailler whose remarkable attentiveness to detail contributed to the finesse of the work in every aspect. Needless to say, I have you two to thank for the useful results in this thesis, and my academic growth throughout.

I thank Dr. Emmanuel Audusse and Dr. Yelva Roustan for being members of the thesis committee for the first- and second-year assessments. Your comments assisted with the advancement of the work, and its better-shaping.

Furthermore, I acknowledge the members of the thesis jury, Dr. Frederic Chevallier, Dr. Christine Lac and Dr. Riwal Plougonven, in addition to those above-mentioned. Your scrupulous comments, questions, and insight crowned my doctoral experience with invaluable wisdom.

Last, but not least, I thank my friends. Those at LMD and around: you made the experience all the more rich. Those in Lebanon and abroad: the will to continue came from you just as much as it did from me. May this thesis be but a droplet in this generation's sea of contributions.

“Every vessel becomes less spacious with (more) contents, except the vessel of knowledge; its capacity is expanded by its contents.”

Ali ibn Abi Taleb

كُلُّ وِعَاءٍ يَضِيقُ بِمَا جُعِلَ فِيهِ
إلا وِعَاءَ الْعِلْمِ ، فَإِنَه يَتَسِعُ بِهِ.

علي بن أبي طالب

Contents

Chapter 1

Introduction

Since the emergence of conscious life on Earth, the sky has been quite a wonder for the creatures below it. Even before they developed speech, intelligent beings were capable of contemplation, and were perhaps capable of unspoken *discussions*. Unvoiced questions, with assiduous pointing and expressions of awe, can probably be translated today as: How does the sky evolve? Are there patterns? How does it carry what it carries? Are there laws for what it does and how it looks? What is it, the sky? Today, we hope to answer some of these questions. The language we use is all the more dull than our ancestors' awe, but it is hopefully one that will awe the generations to come.

With time, many more elaborate questions developed in relation to the sky. Then the scientific method was perfected, and once-weak answers could be tested, completed, and considered well-established truth. It was official: Air is different from void—it is in fact a fluid; The Earth, with the surrounding gas, is round; The macroscopic physical world behaves in somewhat predictable ways (or at least we think it does.) The sky was later named *the atmosphere* and considered to have multiple levels. These were given names: the troposphere near the surface of the Earth and where the weather occurs, the stratosphere, mesosphere, and thermosphere, then the exosphere separating us from outer space. Questions developed at the level of each, the most numerous of which were at the most inhabited level: the troposphere. And that brings us to our domain.

Observations at this level guided curiosity even further: Wind was observed to lift dust from the ground, and carry it far away—how? Smoke from fire would rise up in the air—why? Volcanoes released plumes which would disperse to invisibility in only a few days—what process was this? These are issues we aim to address—actually, model—in satisfactory detail.

1.1 Context

1.1.1 Sharp plumes

Many compounds can be transported by the wind in the atmosphere, a process which we will refer to as *advection*. Even though our focus will exclusively be on gas-phase compounds hereinafter, it is worth mentioning that matter in liquid and solid phases can be advected in the atmosphere as well. With the exclusion of liquid and solid water in clouds, these particles, with a size typically ranging from $\simeq 1\,\mathrm{nm}$ to $\simeq 10\,\mu\mathrm{m}$ [Twomey, 1977], are generally called particulate

Figure 1.1: The *sharp* plume of the Puyehue Cordon-Caulle volcanic eruption, June 4, 2011 (Ivan Alvarado/Reuters). During an eruption, a volcano releases a mixture of gases. The primary constituent of these is water—mainly as vapor—(50-90%), followed in decreasing order by carbon dioxide (1-40%), sulfur dioxide (1-25%), hydrogen sulfide (1-10%), hydrogen chloride (1-10%), and other gases (Textor et al. [2004]). The sharp plume formed of these gases is expelled from the volcanic crater and rises into the air above it. As the vertical speed of the ejected gas decreases, the plume begins to spread in an *umbrella* form. While the bulk of the plume usually remains in the tropopause, depending on the magnitude of the eruption, teragrams of gases and particulate matter can reach the stratosphere (Robock [2000]).

matter, or atmospheric aerosols. Such particles are subject to gravitational forces that prevent them from behaving like passively advected tracers. If we restrain our discussion to gas-phase compounds, we find a wide variety of these chemical species advected in the atmosphere. These include water vapour, gases such as ozone, carbon dioxide and monoxide, nitrogen oxides, sulphur dioxide and dozens of species of volatile organic compounds, among many other natural and anthropogenic gases. These trace gases are carried by the wind, along with the major components of dry air, namely nitrogen (79%), oxygen (20%), and argon (0.9%). Some of the above-mentioned gases have a very active and fast chemistry, as is the case of nitrogen oxides, non-methane volatile organic compounds and—to a lesser extent—ozone, so that their advection in the atmosphere is limited by their relatively short lifetime. Other compounds, like carbon monoxide and sulphur dioxide, have relatively weak background atmospheric concentrations, but have a long chemical lifetime that opens the possibility to observe *plumes* of such gases and follow them using space-borne observation methods over several days or even weeks.

Such plumes can arise from volcanic eruptions or massive biomass burning events: while the main observable gas-phase species in volcanic plumes is sulphur dioxide ($\mathrm{SO_2}$)[1], biomass burning plumes are often characterized by strong concentrations of carbon monoxide (CO) as well as secondary ozone and other trace gases. In the rest of this manuscript, we will refer to such plumes as *sharp plumes* as they are often characterized by concentrations that differ strongly from the atmospheric background and by sharp gradient concentrations at the plume edges. Fig. 1.1 shows one example of the formation of such a plume in sharp contrast with background air.

Sharp plumes containing strong concentrations of species with a relatively long lifetime are perfect real-world test-cases for atmospheric *advection*. The American Meteorological Society defines the latter as “the process of transport

---

[1] We will not discuss the case of volcanic ash nor sulphates in this study, as they are made of condensed matter and are not gas-phase compounds.

of an atmospheric property solely by the mass motion (velocity field) of the atmosphere" [2]. Furthermore, any "chemical or thermodynamic property of the flow that is conserved during advection" can be considered a tracer, with the main requirement of having a lifetime "substantially longer than the transport process under study" [3]. For example, the atmospheric lifetime of carbon monoxide is typically 1 to 4 months, while that of sulphur dioxide is about one week under dry conditions in the free troposphere [Seinfeld and Pandis, 1997]. Atmospheric plumes, such as those of biomass burning and volcanic eruptions in the free troposphere, usually persist for a couple of days to weeks[4].

1.1.2 The advection equation

As discussed earlier—by definition of both tracers and advection—the quantities and distributions of tracers evolve essentially under the influence of advection by the wind. Before formulating the advection equation—for which we will examine ways to obtain numerical solutions in the rest of this manuscript—we introduce quantities that can describe tracer abundance as a function of space. This can be done as tracer *quantity* per unit volume, or per quantity of carrier fluid, where what we call *carrier fluid* is composed of all the gas-phase compounds present in a certain volume, including the major components of air as well as the tracers and trace gases.

As *quantity* can be understood as mass or number of molecules, the tracer quantity per unit volume can, on one hand, be described in mass per unit volume (e.g. $\mathrm{kg\,m^{-3}}$ or, more frequently for trace gases, $\mu\mathrm{g\,m^{-3}}$), which is referred to as mass concentration. On the other hand, it can be described by the number of molecules per unit volume ($\mathrm{molecules\,m^{-3}}$), which is known as number concentration.

In the case where we express the quantity of tracer per quantity of carrier fluid as mass of tracer per mass of fluid, we speak of the mass mixing ratio (in, eg., $\mathrm{kg} / \mathrm{kg}$). Taking the number of molecules of tracer per number of fluid molecules, we speak of number mixing ratio, or, indifferently, volume mixing ratio. For trace gases, this dimensionless quantity falls by construction between 0 and 1, but is often expressed in parts per billion (ppb).

If we annotate by ρ the density of the carrier fluid (in mass per unit volume), by ϕ the (dimensionless) mass mixing ratio of the tracer, and $\boldsymbol{u}$ the three-dimensional wind vector, then the advection equation—which is the Eulerian translation of the Lagrangian conservation of tracer mixing ratio along any trajectory, $\frac{\mathrm{d}\phi}{\mathrm{d}t} = 0$—can be written as:

$$\frac{\partial \phi}{\partial t} + \boldsymbol{u} \cdot \nabla(\phi) = 0. \tag{1.1}$$

We call Eq. 1.1 the *advective form* of the advection equation, which also admits a *flux form*:

$$\frac{\partial \rho\phi}{\partial t} + \nabla \cdot (\rho\phi\boldsymbol{u}) = 0. \tag{1.2}$$

The advective form describes the evolution of tracer mixing ratio in time, while the flux form describes the evolution of its concentration, $\rho\phi$. These two forms are equivalent if, and only if, the carrier fluid density, ρ, verifies the *continuity equation*, which guarantees the conservation of mass:

$$\frac{\partial \rho}{\partial t} + \nabla \cdot (\rho\boldsymbol{u}) = 0. \tag{1.3}$$

---

[2] Advection entry in the AMS Glossary of Meteorology

[3] Tracer entry in the AMS Glossary of Meteorology

[4] For this reason, we fix the length of our academic test cases at 12 days, as [Meloen et al., 2003] and [Lauritzen et al., 2012] do, in Chapter 3.

Figure 1.2: The plume of the Puyehue Cordon-Caulle volcanic eruption, beginning to be advected by the wind (Claudio Santana/AFP/Getty Images)

1.2 Methods for the numerical resolution of the advection equation

In its general form, the advection equation does not have a straightforward analytical solution. Even though analytical solutions may be obtained for some particular cases and under specific restrictions (e.g. [Perez Guerrero et al., 2009], [Zoppou and Knight, 1997], [ECMWF, 2002]), these methods are not of general and practical use. As such, there is a strong need for numerical solutions of discretized forms of the advection equation, either in the advective (Eq. 1.1) or flux form (Eq. 1.2).

Precursors of modern calculus, Gottfried von Leibniz and Isaac Newton, were the first to address the fact that some differential equations lack analytical solutions. Consequentially, they were also the first to introduce different approaches to deal with this problem. While Leibniz resorted to geometry to find new forms of analytical solutions by introducing novel trigonometric functions, such as the inverse tangent (Leibniz [1684, 1693]), these newly introduced functions only suited some specific forms of differential equations. Newton then discussed approximate solutions to some of these equations by series expansion in his treatise on differential calculus [Newton, 1736]. These ideas, along with with the work of Brook Taylor—the Taylor series—set the theoretical bases for the numerical solution of differential equations, which then awaited the era of computers. Focusing on equations whose solution depends on space and time, such as the advection equation, we can be more precise regarding the discretization process.

Usually—if we omit spectral methods based on Fourier (or spherical harmonic) expansions and the domain of *mesh-free methods* [Fasshauer, 2007]—obtaining approximate numerical solutions for a partial differential equation (PDE) such as the advection equation (Eq. 1.1 or 1.2) requires the domain of definition to be divided into small sub-domains. Accordingly, we suppose that the studied variable (in our case, the mixing ratio ϕ) can be correctly approximated in each of the sub-domains by a low-order multivariate polynomial expansion (e.g. constant, linear, quadratic, etc.). Each of these elementary spatial subdomains is called a *cell*, and together they form a discretization of the domain called a *mesh*, or *grid*. Numerical methods can be designed to build approximations of the exact solution in each cell in such a way that the merging of these *finitesimal* solutions converges towards the exact solution of the PDE as the grid becomes finer. Such numerical methods are called *numerical schemes*.

Having discussed the discretization in terms of space, we now turn to time as the advection equation also incorporates the time dimension. In such equations, both time and space are discretized, with one to three dimensions of space discretized following a mesh as discussed above, and one dimension of time discretized by a partition into finite intervals. The latter intervals often have a (conditionally) constant length called a *time step*.

Numerical strategies for solving the advection equation therefore involve two essential steps which we examine below: designing a mesh that fits the geometry of the domain, and designing the numerical schemes which permit to obtain approximate solutions of the equation for each mesh cell and each time step. In the present section, we first examine different existing strategies to build meshes covering an entire sphere, and then we move on to some of the main numerical schemes designed to obtain numerical solutions of the advection equation on these meshes.

1.2.1 Cartesian grid formulations on the sphere

Whether René Descartes was the first to propose the classical Cartesian coordinate system in his book *La Géométrie* [Descartes, 1637], or simply developed its use in localization therein, it came to carry his name. From this coordinate system derives a type of mesh called the *Cartesian mesh* or—more prevalently—the *Cartesian grid*. These grids are made up of the set of squares or rectangles obtained by splitting each of the two coordinate axes of the plane into intervals and—for each axis—constructing the lines parallel to the other axis, passing through interval boundaries. The same method is applied for the meshing of n-dimensional spaces as well.

Even though this type of mesh is not directly applicable to a sphere—which does not admit a Cartesian coordinate system, as its points cannot be described as a pair of coordinates along two orthogonal axes—meshes with a structure comparable to the Cartesian meshes of the plane can be built on the sphere. They are traditionally called Cartesian, or *rectilinear*, grids and can cover the entire sphere or a part of it. Rectilinear grids can be obtained readily from any map projection of the sphere: if we choose a map projection associating a point X on the sphere to a point (x_1, x_2) of the plane[5], then any Cartesian mesh of the plane can be mapped onto a corresponding rectilinear mesh covering the sphere (or a part of it). The properties of such rectilinear meshes depend on the properties of the map projection.

The latitude-longitude grid

The latitude-longitude (lat-lon) grid derives from the latitude-longitude Geographic Coordinate System (GCS), in which each point, X, on the sphere is mapped to a longitude, λ, and a latitude, θ, where θ is the angular distance from X to the equatorial plane, and λ is the angular distance between the plane containing the meridian of Greenwich and the orthogonal projection of X onto the equatorial plane. Lines of constant latitude are called *parallels*, and lines of constant longitude are called *meridians*. From this coordinate system derives immediately the construction of the lat-lon grid (Fig. 1.3): when dividing the $[0, 2\pi]$ interval of of longitudes into n sub-intervals, and the $[-\pi/2, \pi/2]$ interval of latitudes into m sub-intervals, one obtains a lat-lon grid such as the one shown in Fig. 1.3. Lat-lon grids are frequently used for global models of the atmosphere, with the advantage of simplicity in their construction and in the discretization of the equations of motion upon them. A major drawback of such meshes, however, is the non-uniform area of grid cells over the mesh, with extremely small areas close to the poles (Fig. 1.3).

---

[5] The function mapping the point X to a point (x_1, x_2) in a plane is called a *map projection*

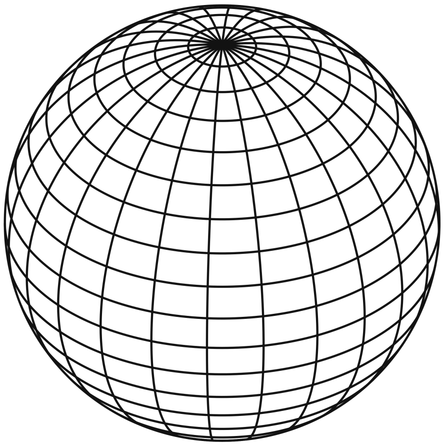

Figure 1.3: A lat-lon grid covering the globe, with a visible singularity close to the pole

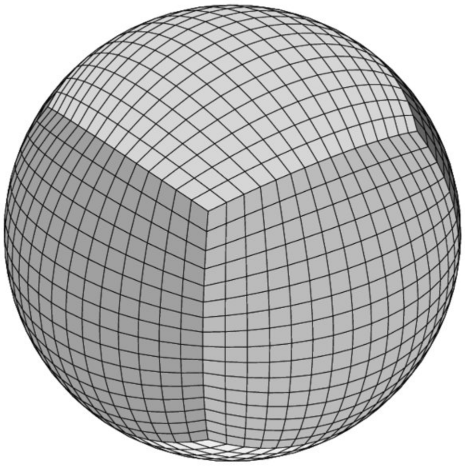

Figure 1.4: A cubed-sphere meshing of the globe [Ullrich, 2014]

Other discretizations of the sphere with Cartesian grids

To avoid such sharp differences between cell areas at the poles and at the Equator, various ways to discretize the sphere into two or more partial Cartesian-grids have been designed and used in atmospheric science. They derive from quilting together multiple coordinate systems, each of which is used to costruct a Cartesian grid covering a part of the sphere. Such constructions include cubed-sphere meshes (Fig. 1.4) and Yin-Yang meshes (Fig. 1.5).

Cubed-sphere Cartesian-based meshes arise from a method of dividing the sphere into 6 identical faces, by projecting the sides of a circumscribed cube onto a sphere's surface. In each face, a Cartesian-type mesh is built, resulting in 6 coordinate systems quilted together to cover the entire sphere, with no singularities at the poles [Ronchi et al., 1996]. However, it endues some difficulty in remapping the values from one convex face to its neighbours at the common boundaries. Also, the accuracy of finite difference methods on the cubed sphere is poor due to these boundaries, relative to other grids such as the triangular and hexagonal ones detailed in Section 1.2.2 [Thuburn et al., 2014].

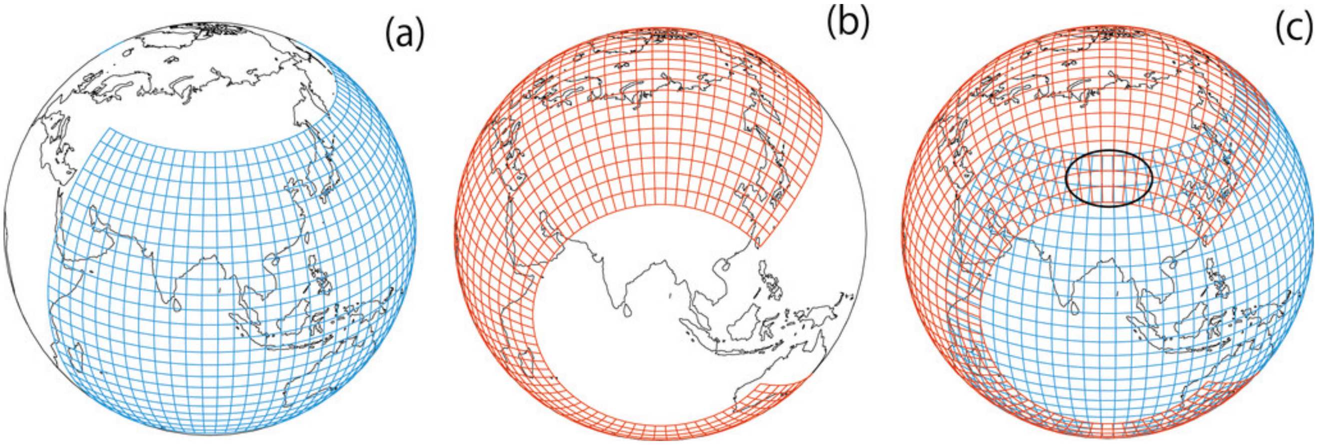

Figure 1.5: The Yin (a), the Yang (b), and the Yin-Yang mesh (c) over the globe with the overset region (pointed out by the black oval) which is the cause of the Yin–Yang grid's disadvantage [Baba et al., 2010]

Meanwhile, the Yin-Yang grid, proposed in [Chesshire and Henshaw, 1990], is formed of two intertwined curved rectangles—each discretized as a limited-domain Cartesian grid—placed at a 90 degree rotation relative to each other. The overlapping parts are removed to form one continuous boundary between the two partial grids. The resultant *knitting* is similar to that of a tennis ball (Fig. 1.5). As with the cubed sphere, the use of the Yin-Yang mesh poses computational difficulties due to the existence of sub-domains separated by a boundary, which induces singularities. In the case of the Yin-Yang mesh, the problem resides particularly in the interpolation needed in the overlapping region between the two sub-domains [Baba et al., 2010].

1.2.2 Triangular and polygonal meshes

To overcome the problems of singularities at the pole, as well as those resulting from quilting together various limited-area grids, alternatives to Cartesian meshes have been designed. Instead of a construction from a checkerboard-like array of cells arranged in the shape of a regular matrix, tessellations of the sphere can be constructed using other systematic approaches based on either Delaunay triangulations (for triangular meshes) or Voronoi diagrams (for polygonal meshes). The use of such grids to overcome the abovementioned difficulties for global-scale atmospheric models was explored by a number of groups in the last few decades [Williamson, 2007]. Quasi-uniform grids with triangular and hexagonal-pentagonal cells can be built in such a way to have reduced singularities compared to the typical lat-lon grid. However, the first attempts in this direction (e.g. [Sadourny et al., 1968], [Sadourny, 1972]) failed at delivering important numerical properties which could be achieved on Cartesian longitude–latitude grids (Arakawa [1966], Sadourny [1975b,a], Arakawa and Lamb [1981]). Subsequently, these ideas fell into disgrace among atmospheric scientists for some decades, leading to the development of most general circulation models (GCMs) on lat-lon grids. However, recent advances (see, e.g., Dubos et al. [2015], Satoh et al. [2014a] and references therein) have resulted in successful attempts at overcoming the limitations of Cartesian grids through the use of such quasi-uniform meshes.

Voronoi diagrams and Delaunay triangulations

Voronoi diagrams, which we also call *Voronoi meshes*, are generated using a set of points called *generators* scattered in a domain—in our case, on the surface of a sphere—and associating to each generator all the points in the domain that are closer to it than to any other generator in the set. Each resulting association of points is called a *cell*. An example of such a diagram on the Earth surface is shown in Fig. 1.6. The resulting cells can take the shape of any polygon, depending on the initial point distribution.

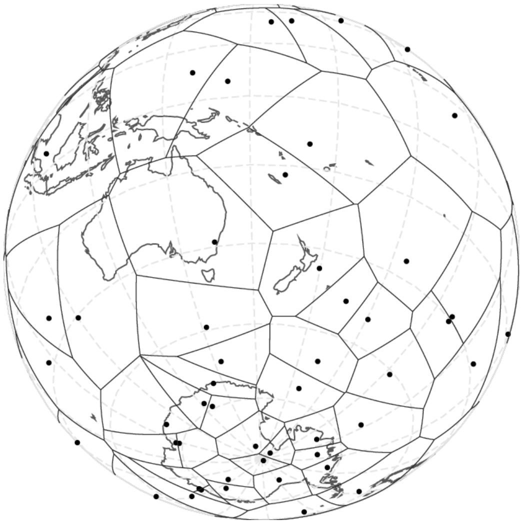

Figure 1.6: An example of a Voronoi mesh over the entire Earth (Fig. by Debayle and Sambridge [2004])

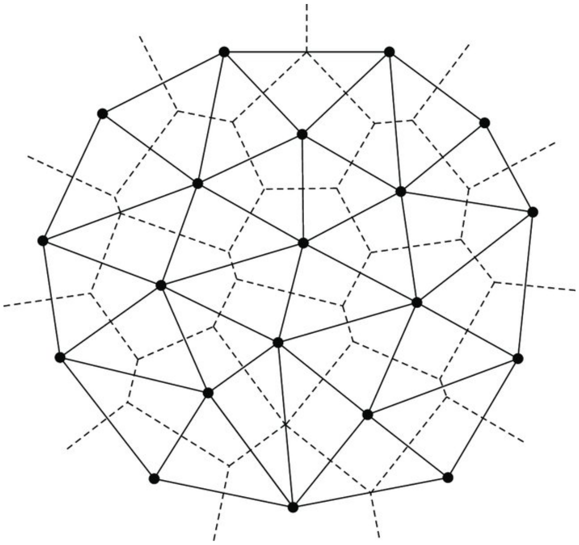

Figure 1.7: A Delaunay mesh (triangular) on a Voronoi mesh (polygonal) (Fig. from Uwitonze et al. [2018]). Here, the Delaunay triangulation is the dual mesh of the Voronoi primal mesh.

Taking the dual mesh of a Voronoi mesh—the mesh obtained using the generators of Voronoi cells as vertices—a

Delaunay triangulation is obtained (Fig. 1.7). A Delaunay triangulation of a domain is a tessellation of this domain by triangles such that the circumscribed circle of each triangle does not contain vertices of other triangles.

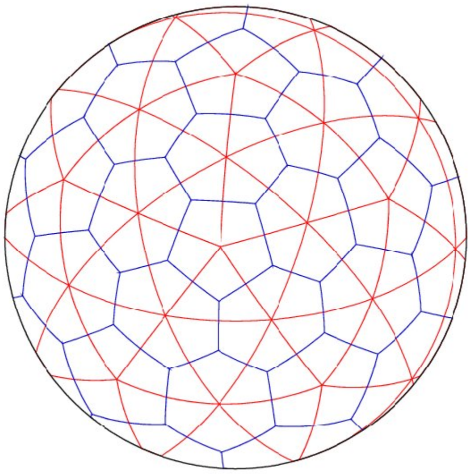

Figure 1.8: A hexagonal-pentagonal Voronoi mesh (blue) and its dual Delaunay mesh (red) obtained from one dyadic refinement step of the regular icosahedron (fig. from [Ripodas et al., 2009]).

Icosahedral meshes

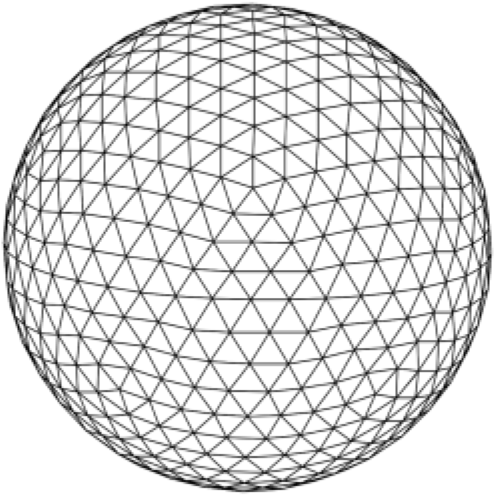

Figure 1.9: A triangulation of a sphere, from a refinement of a spherical icosahedron. (Fig. from Suarez et al. [2013])

The *icosahedral mesh* described in [Sadourny et al., 1968] starts from the tessellation of the sphere into 20 identical spherical equilateral triangles following the structure of a regular icosahedron. The latter is one of the Platonic solids, which has 20 triangular faces, separated by 30 edges, connected at 12 vertices, each of which is the confluence of 5 faces and 5 edges. Each of these 20 triangular faces can thereafter be divided into smaller triangles, yielding a relatively uniform tessellation of the sphere into small spherical equilateral triangles (Fig. 1.9). Such triangular tessellations of the sphere are the base of the icosahedral meshes which we use in this work. If each of the vertices of a tessellation such as the one shown in Fig. 1.9 is used as a Voronoi generator as described in Sadourny et al. [1968], the obtained Voronoi diagram is a hexagonal-pentagonal tessellation of the sphere, mainly comprised of hexagons, with exactly 12 pentagons corresponding to the 12 vertices of the icosahedron (Fig. 1.8).

Meshes defined following the procedure defined above are not Cartesian, but they have a repetitive and organized structure. For example, a hexagonal-pentagonal mesh as defined in Sadourny et al. [1968] is the dual of the mesh obtained by dividing the sphere into 20 triangles (or 10 *rhombi*), each rhombus being regularly divided into n^2 elementary triangles). Despite this regularity, each cell of this structure has a unique set of geometric properties such as angles, areas, and edge lengths. As a result, numerical schemes on such meshes will be the same as schemes supporting the unstructured, variable-resolution meshes which we discuss below.

Variable-resolution meshes and unstructured meshes

The overall resolution of the meshes mentioned in the parts above can be changed according to the needs, where a higher resolution means—in theory—better results, at the expense of a heavier computational cost. However, lat-lon Cartesian grids or icosahedral grids do not permit to obtain a variable resolution in a flexible way, permitting the modeller to *zoom* in on particular areas without a general increase in resolution. On the contrary, it is possible to generate Voronoi meshes with a variable resolution, with higher resolution over one or several areas of interest, and lower resolution elsewhere. Variable resolution on different mesh types can be obtained through several techniques, some of which we mention below:

- Gradual local refinement of Voronoi meshes
- Nested cell-division of Cartesian meshes
- Generation of Voronoi meshes with non-uniform generator density.

Gradual local refinement consists of choosing a region of interest, and performing a local increase in resolution until the target resolution is reached over the desired area. This can be applied to patches in Voronoi and Delaunay meshes to resolve local perturbations, due to mountains, for example. However, this poses a risk of degrading global accuracy [Weller et al., 2009].

In Cartesian grids, variable resolution can be attained by subdividing mesh cells into 2 or more sub-cells. These subdivided cells can, in turn, be recursively subdivided as many times as necessary to reach the desired refinement (Fig. 1.10). It is possible to refine only some cells, in select regions, or the entire mesh if necessary. Another, less flexible, approach consists of building a non-uniform lat-lon grid, as is made possible in the LMDZ model (Z standing for *Zoom*), with a finer resolution in a user-defined latitude/longitude region (applied, e.g., by Vadsaria et al. [2020] to the Mediterranean region). This has the advantage of preserving the native grid structure and cell indexing, but the inconvenience of having extremely elongated grid cells outside the target region.

Voronoi meshes offer an even greater flexibility in generating fully unstructured grids with—almost—arbitrary variations in resolution. In principle, any initial distribution of generators on the surface of a sphere, with a user-specified surface density-function for generators, permits the construction of a Voronoi diagram with its corresponding triangular dual mesh. Even though, in practice, iterative processes must be applied—to avoid unwanted features such as the

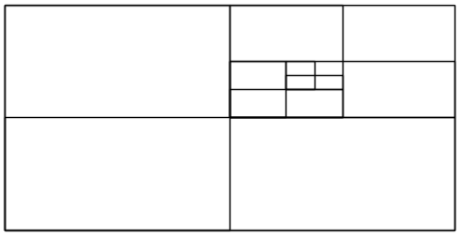

Figure 1.10: Nested cell division of Cartesian mesh cells in a select region

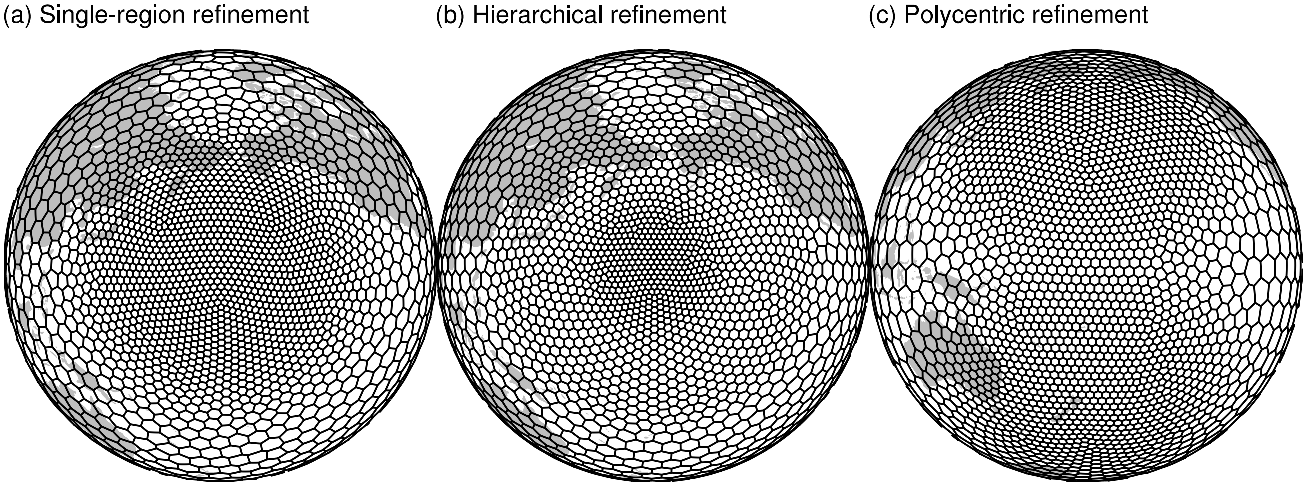

(a) Single-region refinement (b) Hierarchical refinement (c) Polycentric refinement

Figure 1.11: Example types of non-uniform mesh refinement using different density functions, [Zhou et al., 2020]

presence of polygons with an elevated number of neighbours, and to ensure mathematical properties such as coincidence between centroids and circumcenters—this is a very promising way of generating variable-resolution grids with a flexible refinement (e.g. Du et al. [1999, 2003], Zhou et al. [2020]).

1.2.3 Numerical schemes

To study the efficacy of using the above-defined Voronoi icosahedral (or unstructured) meshes for solving the advection problem on the sphere, numerical schemes for the solution of Eq. 1.1 on Voronoi meshes are needed. In the rest of this manuscript, we use both method-of-lines schemes (based on uncoupling the space and time dimensions) and semi-Lagrangian schemes (which treat space and time in a coupled way, using Lagrangian ideas and a knowledge of the specific properties of advection). While the details of the numerical schemes used in this thesis are given later on, some ideas are presented here. For example, spatial discretization schemes depend strongly on the particular form of the equation and mesh, and are a main focus of the rest of this work. Two main classes of spatial discretization schemes can be designed for the advection equation, namely *finite volume schemes* and *finite difference schemes*. While finite difference schemes aim at evaluating the values of the exact solution at particular points, finite volume schemes aim at evaluating the average of the exact solution over one particular element, or mesh cell (either an interval, an area, or a volume, depending on the dimension of the problem). In the following, we prioritize finite-volume methods, which easily allow an exact mass-conservation and are more adapted to the flux-form of the advection equation (Eq. 1.2), as explained in Section 2.3.4.

Desirable properties

The exact, continuous form of the advection equation has several properties which should, if possible, be preserved by the numerical schemes aimed at providing approximate solutions on a discrete grid. The main properties which may be derived from Eq. 1.1, or equivalently from Eq. 1.2 provided that the carrier fluid verifies the continuity equation 1.3, are the following:

- Eq. 1.2 implies the conservation of tracer mass during advection. This should be verified by the numerical solutions as well.
- From Eq. 1.1, we see that the tracer mixing ratio, ϕ, is conserved along Lagrangian trajectories. This implies, in particular, that, if the mixing ratio, ϕ, is initially contained within an interval $[\phi_{\text{min}}, \phi_{\text{max}}]$ at the initial time in the entire domain, it must stay within this exact same interval throughout advection. Such a property is called *monotonicity*. It also implies positivity, which is a weaker property than monotonicity: if ϕ is initially positive, it should stay so.
- Lagrangian conservation of the mixing ratio also implies that all the relationships between tracers should be preserved during advection: if tracers $\phi_1,\ \phi_2,\ \ldots, \phi_n$ are initially linked by a relationship $f\left(\phi_1,\ \phi_2,\ \ldots, \phi_n\right) = 0$ and advected by the same wind field $\mathbf{u}$, then, at any later time, the relationship $f\left(\phi_1,\ \phi_2,\ \ldots, \phi_n\right) = 0$ should still be verified.

Some of these properties can, and, if possible, should be verified exactly by the approximate solutions of the advection equation. This is notably the case of the conservation of tracer mass, positivity, and monoticity. Other properties can only be approximately verified by numerical solutions obtained through numerical methods, as is the case of the preservation of non-linear relationships between tracers, and, as we discuss later, the conservation of entropy. Other desirable properties of numerical schemes include a good order of accuracy, *i.e.* a fast convergence of the approximate solutions towards the exact solution when grid resolution increases. More practical considerations [Freitas et al., 2011] include computational properties such as a relatively low cost-to-performance ratio, in terms of time, memory space, and computational power, for the numerical scheme's implementation.

Obtaining one of these properties is not a difficult task: for example, the most simple—and most fundamental—scheme of Godunov [1959] guarantees mass conservation and monotoniticy along with a very small computational cost, and even an exact preservation of linear tracer relationships. However, this comes at the expense of accuracy and performance in preserving non-linear relationships between tracers. Schemes with a high-order convergence rate would naturally not preserve monotonicity, such that it is necessary to apply *slope-limiting* to these schemes to restore monotonicity during their implementation, at the expense of a loss in accuracy (Van Leer [1977], Colella and Woodward [1984], Dukowicz and Kodis [1987]).

Generally, monotonicity of the numerical advection schemes can be guaranteed only if the time step is short enough to avoid numerical instabilities. This is usually guaranteed by the Courant-Friedrichs-Lewy (CFL) condition: for most numerical schemes, stability and monotonicity hold only if the Courant number:

$$C = \frac{U\Delta t}{\Delta x} \tag{1.4}$$

(where U is the scale of flow speed, Δt is the time step, and Δx is the spatial resolution) is smaller than an upper bound, typically close to 1 [Courant et al., 1928]. This condition implies that the spatial resolution cannot be improved without also reducing the time step, at the expense of computational cost. For unstructured meshes, the meaning of Δx is not straightforward. In this work, we take the distance between two neighboring cell centers, the latter detailed in Chapter 2.

If several space dimensions are treated separately, then a particular Courant number may be calculated for each space dimension, in which case monotonicity is guaranteed only if each of these partial Courant numbers respects the stability condition.

1.2.4 Applications

Chemistry transport models (CTMs)

A chemistry transport model (CTM) is used to simulate atmospheric advection and the chemistry of gas-phase and particulate species in the atmosphere. Apart from chemical processes, these models, used for research and forecast, numerically solve the advection equation for realistic three-dimensional wind fields. One limitation of such models is the difficulty they face in appropriately resolving the problem of the long-range advection of sharp plumes, due to excessive numerical diffusion [Eastham and Jacob, 2017], [Zhuang et al., 2018]. Accordingly, studies which examine new strategies to numerically solve the advection equation may naturally find applications in CTMs (e.g. Lachatre et al. [2020]). To illustrate the diversity present in chemistry-transport models, we highlight some of them below.

Modèle de Chimie Atmosphérique de Grande Echelle (MOCAGE) is the CTM used by the French national meteorological service, Météo-France [CNRM, 2014]. Its primary use is to determine the atmosphere's content in aerosols and trace gases. These are used for different purposes, from forecasting daily air quality, up to determining the impact of climate change. Also notable—relative to this study—is the ability of MOCAGE to monitor volcanic ash clouds [Sič et al., 2015], making it one of the commonly used models in a similar domain to ours.

In continuous development since 1997 at LMD in collaboration with other institutes, CHIMERE is an Eulerian off-line CTM, run with external forcings. This CTM has been used for forecasts of atmospheric pollution in France and abroad [Menut et al., 2013, Mailler et al., 2017]. This three-dimensional CTM is based on Cartesian meshes of adjustable resolution in the horizontal dimension, from 1 km at the urban scale, up to 100 km at the regional scale. As in other chemistry-transport models, physico-chemical processes include anthropogenic and natural emissions of gases and particulate matter, photolysis, reactivity, sedimentation and others. Horizontal transport is resolved using the Van Leer [1977] scheme or the Piece-wise Parabolic Method (PPM) [Colella and Woodward, 1984], depending on the user's choice, while the anti-diffusive Després and Lagoutière [1999] advection scheme is included to reduce vertical diffusion of sharp plumes [Lachatre et al., 2020, Mailler et al., 2021].

Other major CTMs include Geos-CHEM, a global chemistry-transport model working on a cubed sphere, recently including the possibility to *zoom* on a particular region by stretching this cubed-sphere grid [Bindle et al., 2021].

General Circulation Models and their Dynamical Cores

A general circulation model (GCM) is a numerical model that aims to represent, numerically, the circulation of fluids in the atmosphere. Many such models are in use around the world, primarily for weather forecasting and climate studies. To serve this purpose, general circulation models portray the physics of circulation using numerical equations. Physical quantities, such as the mixing ratio of water vapor and other gases, among many other variables, are evaluated by the numerical solution of the advection equation throughout 3D meshes dividing the atmosphere. The part of the model accounting for the equations of motion of the fluid, or the transport equations, is called the *dynamical core* of the model. In the sections below, we detail some of the most prominent GCMs in use today, with some paired models and dynamical cores.

AM3 is the atmospheric component of the CM3 coupled model developed by the Geophysical Fluid Dynamics Laboratory (GFDL) of the National Oceanic and Atmospheric Administration (NOAA). Its particularities include a special focus on addressing emerging issues in climate change, including aerosol–cloud interactions and chemistry–climate interactions, with an interactive chemistry including 85 species. Originally developed on a lat-lon grid, the AM3 GCM was adapted to a cubed-sphere grid in 2011, resulting in improved accuracy and performance [Donner et al., 2011].

Laboratoire de Météorologie Dynamique–Zoom (LMDZ) is a second-generation general circulation model formulated at LMD based on former models [Sadourny and Laval, 1984], [Le Treut et al., 1994], [Le Treut et al., 1998], with the Z of LMDZ standing for zooming capability. The zooming is done on a staggered longitude-latitude Arakawa C-grid on the sphere [Kasahara, 1977], such that both local and global scale climate studies can be done.

Numerically, LMDZ is based on the discretization of the equations of mechanics and fluid dynamics by finite differences and volumes on the adopted grid. This allows modelers to represent the evolution of meteorological variables and the transport of air constituents—such as aerosols and water—for climatic and atmospheric modeling [Hourdin et al., 2006]. The advection equation in LMDZ is solved using the Van Leer [1977] advection scheme, as described in Hourdin and Armengaud [1999]. The Interaction with Chemistry and Aerosols (INCA) model, paired to LMDZ, is a global chemistry-transport model developed at Laboratoire des Science du Climat et de l'Environment (LSCE) [Hauglustaine et al., 2004].

DYNAMICO is an icosahedral dynamical core which solves the hydrostatic dynamical equations of fluid motion, and most notably the multi-layer rotating shallow-water equations [Dubos et al., 2015]. DYNAMICO's finite-difference operators generalize Sadourny's scheme [Sadourny, 1975a] from regular staggered grids to general Voronoi meshes, and are employed in positive-definite finite-volume transport schemes inspired by [Lauritzen et al., 2012], as described in Dubey et al. [2015]. This dynamical core is intended to replace the current lat-lon dynamical core of LMDZ, thereby avoiding singularities at the pole, and opening the possibility of variable resolution in a way even more flexible than LMDZ's current *zoom* capability.

The horizontal discretization of DYNAMICO is that of Ringler et al. [2010], with a discrete quasi-Hamiltonian structure. The horizontal mesh is a quasi-uniform icosahedral C-grid obtained from a regular icosahedron following multiple subdivisions. The vertical discretization is obtained from a three-dimensional Hamiltonian formulation based on mass rather than pressure. Control volumes for tracers are the hexagonal cells of the Voronoi mesh to avoid the fast numerical modes of the triangular C-grid.

Implemented on a mesh similar to DYNAMICO's, the Non-hydrostatic Icosahedral Atmospheric Model is another well-established GCM. It was first developed for use by the Earth Simulator launched by the Japan Agency for Marine-Earth Science and Technology (JAMSTEC) in 2002 [Satoh et al., 2014b]. Its grid begins with an icosahedron, recursively subdivided for higher resolution grids. Over this grid, the transport equations are discretized following the finite volume method, ensuring a conservation of both mass and energy. A characteristic worth mentioning is that NICAM has a multi-scale capability, illustrated by representing cloud structures from the meso- to the planetary scale. It also yields the possibility of regional modelling, by taking a patch of the initial icosahedron formed from two adjacent triangles over the considered region. Another method supported by NICAM to adapt the mesh to a region of importance, while maintaining the global mesh, is through regional refinement. This is done following a Schmidt transformation method which renders the grid gradually finer, culminating at the point of interest [Tomita, 2008].

Finally, and again on a similar grid, the Model for Prediction Across Scales (MPAS) began in a collaborative effort between the Mesoscale and Microscale Meteorology (MMM) Division and the DART development team at the Institute for Mathematics Applied to Geosciences (IMAGe) at the National Center for Atmospheric Research (NCAR) in Boulder, Colorado. It features a Voronoi mesh with variable resolution capability, that can be used from global to local scales Skamarock et al. [2012], Rauscher and Ringler [2014], permitting, for example, atmospheric simulations with a resolution ranging from 60 km to 3 km [Kramer et al., 2020]. A limited-area model (LAM) version of MPAS has been released so that MPAS can now be used both as a GCM, or as a limited-area model (LAM), as described in Skamarock et al. [2018]. MPAS relies on high-order (3^{rd} and 4^{th} order) advection on its Voronoi mesh for tracer advection schemes, as described in Skamarock and Gassmann [2011] and Zheng et al. [2021].

These final three models all allow variable resolution for higher accuracy simulations, though with different levels of flexibility. DYNAMICO and NICAM allow for gradual refinement around a certain point. The level and spatial distribution of refinement is controlled by single parameter defining the Schmidt transform. MPAS meshes make it possible to relax the grid refinement in unneeded regions, while maintaining a higher refinement in more sensitive areas of the global grid (such as in the work of Michaelis et al. [2019]). The latter methodology offers a balance between refinement important for accuracy, and computational economy, with more flexibility than the Schmidt transform.

1.3 Research questions

Recent developments in the fields of GCMs—in particular with the development of the MPAS model of global, limited-area, and variable-resolution capabilities—highlight the need to investigate icosahedral and unstructured Voronoi meshes as an alternative to Cartesian meshes as far as CTMs are concerned. While the possibility of modelling *across scales* is very appealing and opens extraordinary perspectives in terms of studying scale interactions in CTMs, several questions need to be answered before undertaking this direction for models such as CHIMERE, and many others developed for years or decades on Cartesian meshes. Advecting sharp plumes with good accuracy and without excessive diffusion is a critical capability for chemistry-transport models. While several studies have focused on evaluating and improving this capability for Cartesian-mesh CTMs [Eastham and Jacob, 2017, Zhuang et al., 2018, Lachatre et al., 2020], to our knowledge, this question has yet to be addressed in a systematic way on Voronoi meshes. Therefore, the present work aims at addressing the following research questions:

- How do second-order advection schemes for Voronoi meshes compare to classical schemes for Cartesian meshes such as Van Leer [1977] and Colella and Woodward [1984] in terms of accuracy and convergence rates, as well as in terms of limiting numerical diffusion?
- How does advection by a model on an icosahedral Voronoi mesh such as DYNAMICO compare to a state-of-the-art CTM such as CHIMERE in terms of reproducing the advection of a volcanic plume of a real-world eruption?

Answering these questions will give important information on the general feasibility of Voronoi-mesh chemistry-transport models and their potential compared to Cartesian-mesh chemistry-transport models: if Voronoi-mesh transport schemes can compete favourably to similar schemes on Cartesian meshes in terms of transporting sharp plumes, then Voronoi mesh CTMs are already a viable alternative to Cartesian mesh CTMs. Otherwise, work remains to be done to obtain numerical schemes of sufficient performance on Voronoi meshes in order to be able to build next-generation chemistry transport models that would have both the robust properties of numerical advection schemes on Cartesian meshes and the versatility and variable-resolution capability of Voronoi meshes.

1.4 General outline

For the purpose of answering the above-mentioned research questions, we first explain, in detail, the discretization strategies and numerical schemes which we deploy on Voronoi meshes and recall, briefly, the characteristics of the Cartesian-mesh schemes that we implement (Chapter 1).

We then present the academic cases designed to test both the Voronoi and Cartesian frameworks in terms of accuracy and other properties (Chapter 3) before exposing and analyzing the results of the numerical experiments performed on these academic test cases with various numerical schemes at various resolutions in both the Cartesian and Voronoi frameworks (Chapter 4).

Finally, we perform and analyze a simulation of a real-world case of a sharp plume in the atmosphere—namely the eruption of the Puyehue-Cordón Caulle volcano in Chile, on June 4, 2011—with the Voronoi-mesh DYNAMICO GCM and the Cartesian-mesh CHIMERE CTM in order to compare the performances of these two frameworks in a real scenario (Chapter 5). As a conclusion, we give some final considerations on the consequences of the results exposed in Chapters 4 and 5 and their implications regarding the feasibility of substituting Cartesian meshes by Voronoi meshes in chemistry transport models such as CHIMERE, as a first step towards multi-scale chemistry-transport modelling.

Chapter 2

Discretization

Our numerical work is based on spherical Voronoi meshes, particularly quasi-uniform ones with hexagonal and pentagonal cells, whose performance is compared to that of a typical longitude-latitude Cartesian mesh. To go about this comparison, the construction of the Voronoi mesh and its attributes are first detailed.

The bulk of this chapter discusses the discretizations involved in the 2D Voronoi formulation. We begin by explaining how the Voronoi mesh is generated through the spatial discretization of a sphere's surface. We then label the useful mesh elements and proceed to highlight some of the mesh properties. Following the domain discretization, a description of the discretized quantites—involved in the discretized advection equation introduced later on in the chapter—is made. Then, time and space discretization schemes for the advected tracer fields are discussed. The notion of monotonicity, and the slope limiting technique used to achieve it, are further on explained.

In the last section of this chapter, we briefly sketch the properties of Cartesian meshes and the schemes we use with them. The Cartesian structure of the mesh allows the construction of two-dimensional schemes by composing one-dimensional schemes using a strategy called *operator splitting*.

2.1 Mesh generation and descriptions

This section describes the generation of the different meshes used in this study. In what follows, the following definitions are needed:

Definition 2.1.1 (Spherical polygon)**.** It is a part of the spherical domain bounded by spherical arcs. A spherical arc, in turn, is the spherical equivalent of a straight segment, i.e. the shortest-length curve joining two points on the sphere.

Definition 2.1.2 (Mesh cell)**.** Each polygon within a partition of the spherical domain into spherical polygons, not containing smaller polygons of the same mesh, is referred to as *a cell* of the mesh.

Definition 2.1.3 (Neighbouring cells)**.** Cells adjacent to each other by sharing a spherical arc are called *neighbouring cells*. The common spherical arc is an edge of both cells.

2.1.1 Quasi-uniform Voronoi-mesh generation

The following paragraph describes the construction of the quasi-uniform hexagonal-pentagonal Voronoi mesh used in this study. This mesh is inspired, in particular, by the mesh of Sadourny et al. [1968], followed by the optimization procedure of Du et al. [1999].

Definition 2.1.4 (Voronoi mesh)**.** A *Voronoi mesh* is one generated from any distribution of points, each of which is the generator of a cell. The latter is composed of all the points of the domain which are closer to the considered generator than to any other generator.

One result of this definition is that the cells of a Voronoi mesh are polygons. In practice, we start with a regular icosahedron, which is a polyhedron with 20 flat triangular faces. The size of this icosahedron does not matter, as long as the triangular faces are equilateral, and equal to one another. The icosahedron is then projected, radially, onto a sphere. The result of this step is a sphere whose surface is divided into 20 equal spherical triangles, with curved edges and surfaces (Fig. 2.1). The resulting surface is referred to as an *icosahedral mesh*.

The following step consists of refining this icosahedral mesh. To do so, we follow the method of Sadourny et al. [1968]. Each spherical triangle of the spherical icosahedral mesh is considered. Two of its edges are divided into n arcs of equal length. The end of each arc is numbered from 1 to n increasingly from the point common to the two edges, and until the end of the considered edge. Each end of arc is joined with the corresponding end of arc on the second edge of the considered triangle. The lines joining these points together are in turn arcs. Each of the latter is divided into sub-arcs in turn, with an increasing number as we move away from the common triangle vertex. The first arc is kept as 1 segment, the second is divided into 2, and so forth until we divide the n^{th} arc into n sub-arcs. This final arc is, in fact, the third edge of the initial triangle. The ends of these segments are joined together to result in n^2 sub-triangles within the initial triangle. This step's procedure falls into the category of triangular tessellation [Du et al., 1999]. The edges of the resultant spherical sub-triangles, which are no longer equal, have edges which vary to within 18% of each other's lengths [Wang and Lee, 2011]. This resultant mesh is a *Delaunay triangulated mesh*.

The refined triangular mesh of the above paragraph is referred to, in this study, as the *dual mesh*. It is only used in some sub-calculations detailed in the sections below. The cells of this mesh are referred to as *dual cells*. The next step in mesh generation is forming what we call our *primal mesh*, where the main computations of the numerical schemes are made.

To describe, completely, the primal mesh cells, we first obtain their vertices—i.e. the points where the cell edges intersect. By design of the Voronoi mesh, each vertex is the circumcenter of a triangle of the dual mesh. Another consequence of the definition of a Voronoi mesh is that the Voronoi cell edges and dual edges are orthogonal [Augenbaum and Peskin, 1985]. The shapes of the cells of this mesh are primarily hexagons, with 12 pentagons, one surrounding each vertex of the initial 12-vertex icosahedron. Each primal cell also has a centroid, which, in general, does not coincide with the generator. Following Lloyd's iterative algorithm as in Du et al. [1999], the generators of the Voronoi mesh are made to coincide with the centroids of the Voronoi cells by an iterative process. This procedure produces a more uniform mesh.

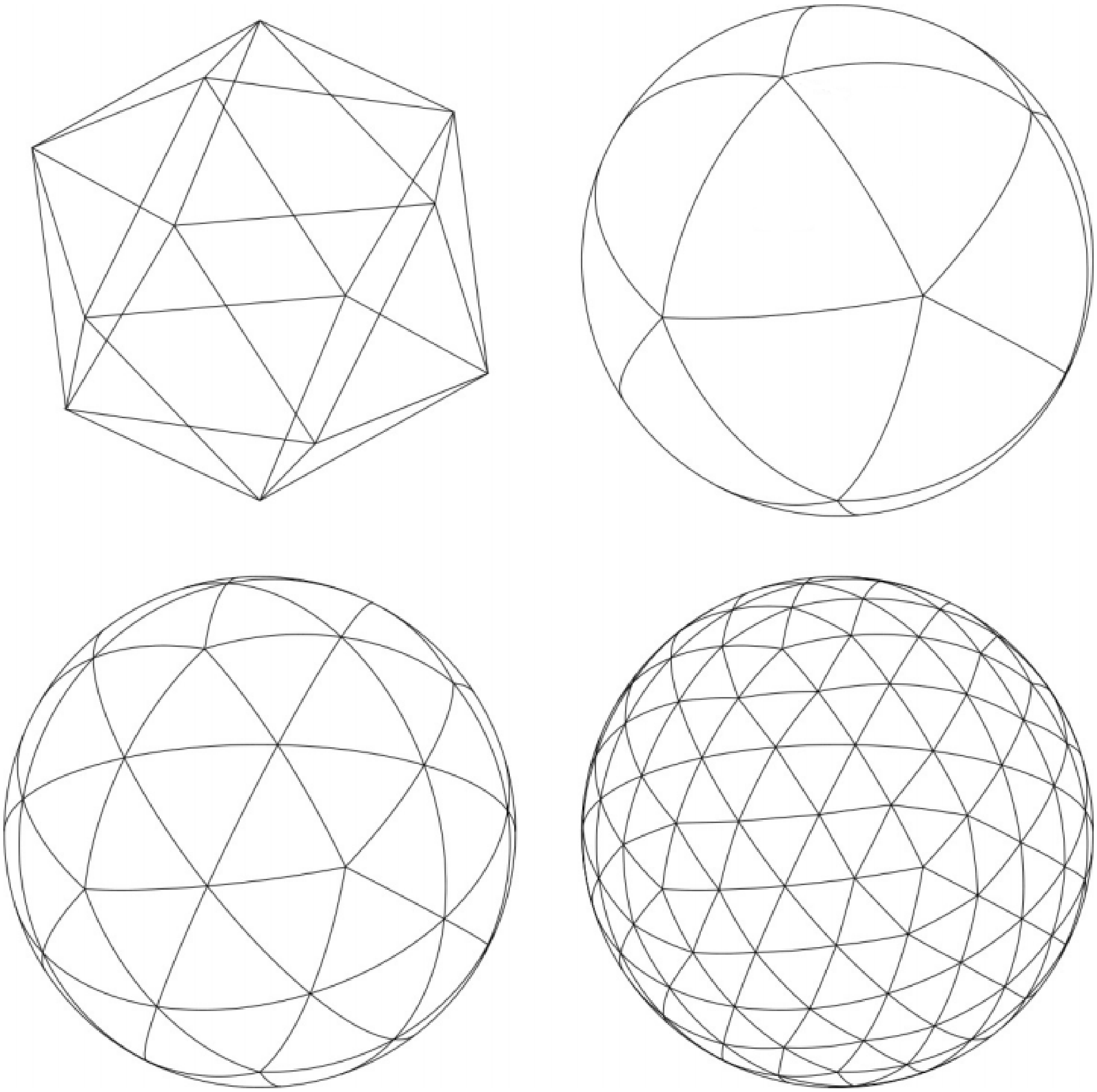

Figure 2.1: Phases of an icosahedral mesh generation, from the regular icosahedron (top left) to the spherical icosahedron (top right), then following n=2 refinement (bottom left), and finally n=4 refinement (bottom right). (Image, modified, taken from Florinski et al. [2020])

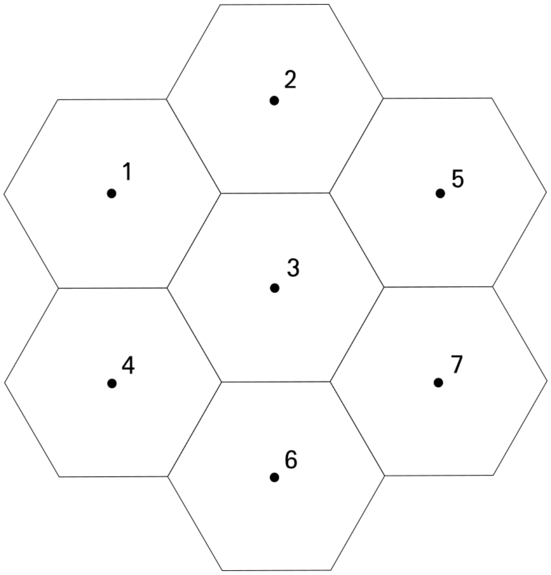

Figure 2.2: Arbitrary unstructured-mesh cell-numbering on a flattened patch of the hexagonal-pentagonal Voronoi grid

2.1.2 Variable-resolution Voronoi-mesh generation

Similarly to the quasi-uniform Voronoi meshes, a variable resolution Voronoi mesh is built upon a Delaunay triangulation. However, to account for the variable resolution, the starting point cannot, in this case, be a regular icosahedron. Instead, a set of points is randomly distributed on the surface of a unit sphere, with a higher probability in regions where higher resolution is sought. A Delaunay triangulation is formed using these points, and then the Voronoi dual is taken in the same way as in the previous case. Also, the target resolution is taken into account during the Lloyd iteration process [Du et al., 1999]. It is important to note that, with variable resolution, the Voronoi mesh is no longer hexagonal-pentagonal: at least some cells have seven edges or more.

2.1.3 Voronoi and Delaunay mesh elements

The following section describes the different parts of the primal and dual meshes, which are defined and annotated for use in the numerical schemes to come. The definitions below apply to the primal and dual meshes simultaneously. The indices used in this section are broadly inspired by the notations of Thuburn et al. [2009].

- **Mesh cells**
  Each cell is referred to using a fixed cell index, k. These indices are unstructured: there is no particular direction for the index increment (Fig. 2.2). A neighbouring cell may or may not have an index with a unit difference from the current cell index. The total number of indices is equal to the total number of cells, with no two cells sharing the same index. Dual mesh cells are referred to by an index, v.

- **Cell areas**
  The cell of index k has an area A_k. A dual cell with index v has an area A_v.

- **Primal-cell centers**
  Each primal cell has a geometric center, or centroid, referred to by its position, $\boldsymbol{x}_k$. The number of cell centers is—quite evidently—equal to the number of cells, and so these centers are assigned the same index, k, as their respective cells. The position of each cell center, in spherical coordinates, is found using the arithmetic mean position of all the points belonging to the cell:

  $$\boldsymbol{x}_k = \frac{\int_{\mathcal{V}_k} \boldsymbol{x} \mathrm{d}A}{\left\| \int_{\mathcal{V}_k} \boldsymbol{x} \mathrm{d}A \right\|} \tag{2.1}$$

  where $\mathcal{V}_k$ represents the primal cell itself, regarded as a subset of the sphere.

- **Cell edges**
  In the Voronoi mesh, each edge of the mesh is referred to using an unrepeated index, e. Each primal cell, k, has a set of edges, E_k. A dual cell , v, has the set of edges E_v.

- **Primal-cell vertices**
  Similarly to the edges, each cell of the Voronoi mesh has a number of vertices, $\mathcal{N}_k$, equal to its number of edges. The indexing is analogous to that of the edges, with a unique index v for each vertex, ordered arbitrarily.

- **Primal-edge lengths**
  The values of the primal edge lengths are designated by l_e, where e refers to the considered edge. l_e has a value corresponding to the arc length of the edge. Similarly, dual edges have lengths d_e.

- **Edge normal**
  Each edge has a normal vector, $\boldsymbol{n}_e$, where e refers to the considered edge. As each edge is common to two cells, this vector points in an arbitrary direction in or out of the considered cell k. A factor $n_{k,e} = \pm 1$ is defined in such a way that vector $n_{k,e}\boldsymbol{n}_e$ points outwards from cell k. This vector is used in the gradient computation detailed in Section 2.2.4.

2.2 Discrete representation of fields

2.2.1 Discrete degrees of freedom

The flux-form advection equation (1.2) is an initial-value problem (IVP) for the density field $\Phi = \rho\phi$. This field, $\Phi(\boldsymbol{x})$, defines infinitely many real numbers, one for each value of the position $\boldsymbol{x}$. The discretization of fields is the process of reducing this information to a finite set of numbers, also called discrete degrees of freedom (DOFs), which can then be manipulated by computers. Of course, this procedure incurs a loss of information, and subsequent errors called discretization errors. One important property of discretization schemes is their order of accuracy, which describes how fast the discretization error decreases as the number of discrete DOFs increases. If spatial discretization errors are $\mathcal{O}(\Delta x)^p$, then the scheme is of order p. For a given problem, the error of higher-order schemes decreases faster with increasing resolution than that of lower-order schemes.

Reducing a field to a finite set of real numbers can be done following multiple approaches. Taking a finite-difference approach, values of $\Phi(\boldsymbol{x})$ are chosen at meaningful points, $\Phi(\boldsymbol{x}_k)$. Following a finite-volume approach, on the other hand, the field $\Phi(x)$ is represented through its averages over a finite set of control volumes. In this study, we adopt a finite-volume approach, where the density of a species is represented by the cell-averaged value of its continuous distribution. Thus, a discrete value of the field is attached to each cell and referred to with the same index:

$$\Phi_k = \frac{\int_{\mathcal{V}_k} \Phi \, \mathrm{d}^2 x}{A_k} \tag{2.2}$$

Similarly, the discretized density, ρ_k, is defined as a cell average:

$$\rho_k = \frac{\int_{\mathcal{V}_k} \rho \, \mathrm{d}^2 x}{A_k}. \tag{2.3}$$

Initial value specified from a closed-form expression

In the practical sense, if we have an analytical expression for the density, $\Phi(\lambda, \theta, t)$, then its value is known at any point of the sphere. Using quadrature formulae, its average over primal cells can be computed almost exactly. However, a simple evaluation at one point, the cell centroid, yields a relatively accurate estimate of the true average. Indeed, this can be seen by considering the integral:

$$I = \int_{\mathcal{V}_k} \Phi(\boldsymbol{x}) \mathrm{d}^2 \boldsymbol{x}. \tag{2.4}$$

Adding and subtracting $\boldsymbol{x_k}$, the position of the centroid C_k of the cell, the expression becomes:

$$I = \int_{\mathcal{V}_k} \Phi(\boldsymbol{x_k} + (\boldsymbol{x} - \boldsymbol{x_k})) \mathrm{d}^2 \boldsymbol{x}. \tag{2.5}$$

Taking a second-order Taylor expansion about the centroid, $\boldsymbol{x_k}$, we obtain:

$$I = \int_{\mathcal{V}_k} \left[\Phi(\boldsymbol{x_k}) + (\boldsymbol{x} - \boldsymbol{x_k}) \cdot \left. \frac{\partial \Phi}{\partial \boldsymbol{x}} \right|_{\boldsymbol{x_k}} + \mathcal{O}\left(\|\boldsymbol{x} - \boldsymbol{x_k}\|^2 \right) \right] \mathrm{d}^2 \boldsymbol{x} \tag{2.6}$$

which is equivalent to:

$$I - \Phi(\boldsymbol{x_k}) \int_{\mathcal{V}_k} \mathrm{d}^2 \boldsymbol{x} = \left. \frac{\partial \Phi}{\partial \boldsymbol{x}} \right|_{\boldsymbol{x_k}} \int_{\mathcal{V}_k} (\boldsymbol{x} - \boldsymbol{x_k}) \, \mathrm{d}^2 \boldsymbol{x} + \int_{\mathcal{V}_k} \mathcal{O}\left(\|\boldsymbol{x} - \boldsymbol{x_k}\|^2 \right) \mathrm{d}^2 \boldsymbol{x}. \tag{2.7}$$

Now, the definition of the cell barycenter is precisely such that the first term on the right-hand-side vanishes. Dividing by the area of a cell, $A_k = \int_{\mathcal{V}_k} \mathrm{d}^2 \boldsymbol{x}$, we obtain:

$$\Phi_k - \Phi(\boldsymbol{x_k}) = \mathcal{O}\left(\Delta x^2 \right). \tag{2.8}$$

From Eq. 2.8, it can be seen that the cell-averaged value can be approximated to a point-wise value at the cell center, with second-order accuracy. This property is used to compute initial values for Φ_k given a closed-form expression for $\Phi(\boldsymbol{x})$. Conversely, during the course of the computation, whenever point-wise values of $\Phi(x)$ are sought, they can be estimated—cheaply—at $\boldsymbol{x_k}$ from the known cell-averaged values. The same can be done for the density, ρ. As a result, the mixing ratio, ϕ, can be estimated at $\boldsymbol{x_k}$ with second-order accuracy as the ratio:

$$\phi(\boldsymbol{x_k}) = \phi_k + \mathcal{O}\left(\Delta x^2 \right) \quad \text{where} \quad \phi_k = \Phi_k / \rho_k. \tag{2.9}$$

These cell-center values are used for the reconstruction of edge values, needed for the advection schemes (detailed in Section 2.3.2).

2.2.2 Edge values of the mixing ratio

The mixing ratio at the midpoints of the cell edges is denoted by ϕ_e. This edge value is needed in the numerical schemes detailed in Section 2.3. Its evaluation depends on the chosen numerical scheme, starting from the value at the respective cell center. This step of the numerical formulation of schemes is referred to as *reconstruction* [Dubey et al., 2015]. To transport the tracer field from one cell to one of its neighbouring cells, we reconstruct the tracer mixing ratio at the edge common to the two cells.

2.2.3 Discretized velocity field

The velocity field, $\boldsymbol{u}$, on the other hand, is a vector field, and a different approach is used to discretize it. To each edge, of index e, we attach a real number, u_e, which we define as the velocity vector—at the edge midpoint—projected onto the normal unit vector of the edge.

2.2.4 Discretized gradient

This quantity is useful for the second order numerical schemes requiring a discrete gradient (Section 2.3.3). This is the discrete counterpart of the continuous gradient of the continuous mixing ratio field. In our study, we go by the work of Dubey et al. [2015], who demonstrate that a first order approximation of the gradient is sufficient to maintain second order scheme accuracy. Following their first order approximation, a first-order estimate of the gradient, $\nabla_v \phi$ is obtained at a each dual cell (with index v) as the dual-cell-averaged gradient:

$$\nabla_v \phi = \frac{1}{A_v} \int_{\mathcal{V}_v} \nabla \phi \mathrm{d}A \tag{2.10}$$

where A_v is the area of the dual cell v, and $\mathcal{V}_v$ is the dual cell itself (i.e. a triangular subset of the sphere). The vertices of these dual cells correspond to the centers of the the primal cells, where the mixing ratio can be estimated with second-order accuracy as discussed above.

Using the Green-Gauss theorem, the above area integral is converted into a line integral:

$$\int_{\mathcal{V}_v} \nabla \phi \mathrm{d}A = \int_{\Gamma} \phi \boldsymbol{n} \mathrm{d}\Gamma \tag{2.11}$$

where Γ is the perimeter of the v^{th} cell, and $\boldsymbol{n}$ is the normal relative to the infinitesimal edge, $\mathrm{d}\Gamma$, directed outwards. Discretizing the above expression using second-order-accurate estimates of the mixing ratio at primal-cell centers, we obtain the discrete gradient of the continuous scalar field at the dual cell v:

$$\nabla_v \phi = \frac{1}{A_v} \sum_{e \in E_v} \left(\phi_{v,e} - \phi_v\right) m_{v,e} \boldsymbol{n}_{v,e} d_e \tag{2.12}$$

where $\boldsymbol{n}_{v,e}$ is the vector normal to the dual edge e, and $m_{v,e} = \pm 1$ is the factor ensuring the vector is directed out of dual cell v (analogous to the $n_{k,e}$ of primal cells). d_e is the length of this dual edge, $\phi_{v,e}$ is the half sum of ϕ estimated at the extremities of the dual edge (which are cell centers) and ϕ_v is the equal-weight average of ϕ at dual-cell vertices, which are also cell centers. We apply the Green-Gauss formula (2.11) to $\phi - \phi_v$, which has the same gradient as ϕ. This ensures that $\nabla_v \phi$ is zero whenever the mixing ratio is uniform. In a second step, $\nabla_k \phi$ is computed for each cell k by performing a dual-cell-area-weighted average of $\nabla_v \phi$ for all dual cells v intersecting the primal cell k.

2.3 Numerical solution of the advection equation

2.3.1 Time discretization

The solution of the advection equation cannot be computed, in practice, at infinitely many values of time t. Instead, we estimate the solution at integer multiples of a time step, Δt, such that:

$$\Delta t = \frac{T}{n} \tag{2.13}$$

where T is the experiment length, and n is the total number of time steps. In practice, as the problem is an IVP, given $\phi_k^{(n)}$, the discrete representation of $\phi(\boldsymbol{x})$ at $t = n\Delta t$, one then estimates $\phi_k^{(n+1)}$ corresponding to time $t + \Delta t = (n+1)\Delta t$. $\phi_k^{(n)}$ is then set aside to proceeds further in time. This repeated procedure is the *time iteration*, or *time loop*.

The numerical schemes marching the approximate solution of the advection equation from time t to time $t + \Delta t$ are classified depending on their separate or coupled treatment of space and time. In the first category is the method of lines, consisting of regarding time as continuous at first, while discretizing the right-hand side of the evolution equation of Φ. This step involves only spatial derivatives and is called the *spatial discretization*. It transforms the original PDE into a set of many coupled ordinary differential equations (ODEs), one for each cell index k. In the second step of the method of lines, time integration schemes for ODEs are used to solve numerically the previously obtained set of ODEs.

In the second category, the difference $\phi_k^{(n+1)} - \phi_k^{(n)}$ is deduced from the advection equation and the finite-volume definition of the discrete degrees of freedom ϕ_k, and approximated. Such schemes are called *space-time coupled*. Space-time coupled schemes make explicit use of the knowledge of the problem being solved, while this knowledge is not used during the time integration step of the method of lines.

In what follows, the space and time decoupled schemes are detailed, followed by an explanation of the used coupled scheme, in the Voronoi mesh framework. The Cartesian schemes are sketched in Section 2.5.3.

2.3.2 Method of lines: time-integration schemes

In this section, we describe the time-integration schemes used as part of the method of lines. Hence, it is assumed that the spatial discretization, described in the next subsection, is known: there is a well-defined procedure to compute, for each cell index k, $\partial\Phi_k/\partial t$, given the values of Φ_k for all k, and other known quantities, such as the discretized wind and air density fields.

Below, we describe the first- and second-order Euler and Heun schemes, respectively. For the simplicity of notations, we omit the subscript k. Thus, we consider the model problem with a single degree of freedom:

$$\partial_t\Phi = f(\Phi(t)) \tag{2.14}$$

Euler method

The simplest time integration scheme, in terms of computational complexity, is the first-order Euler scheme. To begin solving the initial-value problem following the Euler method, a first-order finite-difference approximation is invoked:

$$\partial_t\Phi = \frac{\Phi(t+\Delta t) - \Phi(t)}{\Delta t} + \mathcal{O}(\Delta t) \tag{2.15}$$

which yields an explicit expression:

$$\Phi(t+\Delta t) = \Phi(t) + \Delta t f(\Phi(t)) + \mathcal{O}((\Delta t)^2). \tag{2.16}$$

From the above expression, an iterative discretized form can be stated:

$$\Phi^{(n+1)} = \Phi^{(n)} + \Delta t f(\Phi^{(n)}) \tag{2.17}$$

where $\mathcal{O}((\Delta t)^2)$ is the error term of a first-order finite-difference approximation with step size Δt.

Heun method

This time scheme is a second-order evolution from the Euler scheme [Hairer, 1996]. It takes the prediction step of first-order accuracy, and adds a correction step which brings the scheme to second order.

Again, the starting point is the model ODE (2.14), from which an advance-in-time algorithm is developed. An Euler step is first applied, leading to an estimate $\tilde{\Phi}^{(n+1)}$ of Φ at time $t+\Delta t$. The time derivative of Φ at $t+\Delta t$ is then calculated from $\tilde{\Phi}^{(n+1)}$ and used to estimate $\Phi^{(n+1)} - \Phi^{(n)}$ by the trapezoidal rule, with second order accuracy:

$$\tilde{\Phi}^{(n+1)} = \Phi^{(n)} + f(\Phi(t))\Delta t, \tag{2.18}$$

$$\Phi^{(n+1)} = \Phi^{(n)} + \frac{1}{2}\Delta t \left[f(\Phi^{(n)}) + f(\tilde{\Phi}^{(n+1)}) \right]. \tag{2.19}$$

2.3.3 Method of lines: spatial schemes

Having dealt with the time-integration problem, we are left with the purely spatial problem of estimating the right-hand-side of the flux-form advection equation (1.2), or, more precisely, its discrete representation.

Upwind scheme

The upwind, or Godunov, scheme [Godunov, 1959] is a 1st-order spatial scheme based on the direction of wind flow. The cell-averaged values of tracer density Φ are the main input of the scheme. These are obtained from an initial condition or from the previous time step. In addition to Φ_k, the scheme takes as input the cell-averaged air density, ρ, and the discretized wind field, or, more precisely, the discretized air-flux:

$$U_e = \rho \boldsymbol{u} \cdot \boldsymbol{n}_e. \tag{2.20}$$

From these values, as explained before, one can immediatelty estimate the mixing ratio at cell barycenters as $\phi_k = \Phi_k/\rho_k$. Then, the edge values of ϕ are approximated according to the following conditional equation following the notations in Fig. 2.3:

$$\phi_e = \begin{cases} \phi_i, & \text{if } U_e < 0. \\ \phi_j, & \text{if } U_e > 0. \end{cases} \tag{2.21}$$

where ϕ_i and ϕ_j are the concentration ratios at the adjacent cells indexed by i and j respectively, and ϕ_e is the value at the common edge. Between these two cells, the upwind one is the cell from which the wind field arrives at the edge under consideration.

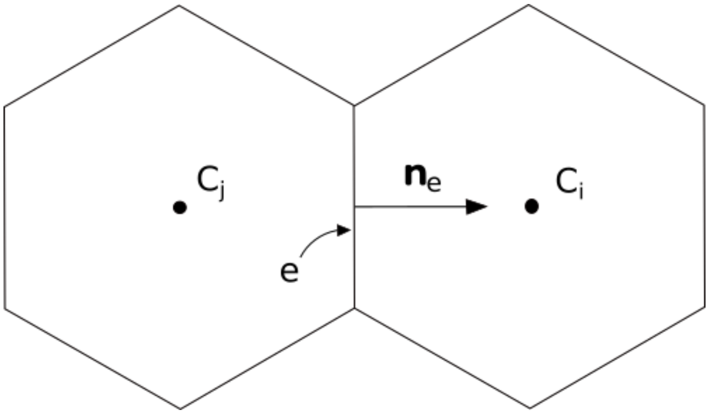

Figure 2.3: Edge normal relative to two neighbouring cells

Finally, to complete the method of lines, an advance in time is made using one of the aforementioned time integration schemes. For consistency in scheme order, the upwind spatial scheme is usually paired with the Euler method (Section 2.3.2) :

$$\Phi_k^{(n+1)} = \Phi_k^{(n)} - \frac{1}{A_k} \sum_{e \in E_k} n_{k,e} f_e \tag{2.22}$$

where E_k is the set of edges of cell k, and the tracer flux is:

$$f_e = U_e l_e \phi_e^{(n)} \Delta t. \tag{2.23}$$

Green-Gauss gradient scheme

The Green-Gauss gradient scheme is an upwind-biased 2nd-order spatial scheme, based on the upwind scheme, but with a linear reconstruction of the tracer mixing ratio—instead of a piecewise-constant reconstruction—to improve the convergence order. The exact scheme used is the one detailed by Dubey et al. [2015].

The Green-Gauss gradient is first calculated in each primal cell. Then, edge values are computed using the linear Taylor expansion :

$$\phi_e = \phi_k + \nabla_k \phi \cdot (\boldsymbol{x}_e - \boldsymbol{x}_k) \tag{2.24}$$

where k is the index of the cell upwind of edge e, and $\nabla_k \phi$ is approximated as detailed in Section 2.2.4.

Following the method of lines, this scheme is usually paired with the 2nd-order Heun time scheme to maintain its order of convergence (Section 2.3.2).

2.3.4 Coupled time and space scheme

We also consider a space-time coupled scheme, i.e. one whose iterations cover both time and space dimensions in a coupled manner. The discretized equations of such a scheme account for time and space variations together.

Semi-Lagrangian finite-volume scheme

The Semi-Lagrangian Finite-Volume (SLFV) scheme is a second-order space-time coupled scheme for the integration of the advection equation formulated for a spherical unstructured mesh by Dubey et al. [2015]. Following this finite volume method, where the cell-averaged Φ is predicted, the flux form of the advection equation (1.2) is taken as a starting point for the discretization.

Given only the wind field, let $\boldsymbol{x}_e^*$ be the foot of the backward trajectory followed during half a time step from the midpoint $\boldsymbol{x}_e$ of edge e:

$$\boldsymbol{x}_e^* = \boldsymbol{x}_e - \frac{\Delta t}{2}\boldsymbol{u}_e. \tag{2.25}$$

We can estimate ϕ at $\boldsymbol{x}_e^*$ from the linear Taylor expansion:

$$\phi_e^* = \phi_k + \nabla_k \phi \cdot (\boldsymbol{x}_e^* - \boldsymbol{x}_k) \tag{2.26}$$

where k is the index of the upwind cell.

Now, considering the air mass traversing edge e during the time interval $[t, t+\Delta t]$, which is an input to the scheme:

$$F_e^{\text{air}} = \int_t^{t+\Delta t} \int_{\Gamma_e} \rho \boldsymbol{u} \cdot \boldsymbol{n_e} \mathrm{d}\Gamma \mathrm{d}t \tag{2.27}$$

the amount of tracer traversing this edge during the same time interval is:

$$F_e = \int_t^{t+\Delta t} \int_{\Gamma_e} \phi \, \rho \boldsymbol{u} \cdot \boldsymbol{n_e} \mathrm{d}\Gamma \mathrm{d}t \tag{2.28}$$

which is estimated with second-order accuracy as:

$$F_e = \phi_e^* F_e^{\text{air}}. \tag{2.29}$$

Finally, integrating the flux form over cell k and time interval $[t, t+\Delta t]$ yields an update formula for Φ_k:

$$\Phi_k^{(n+1)} - \Phi_k^{(n)} = -\frac{1}{A_k} \sum_{e \in E_k} n_{k,e} F_e \tag{2.30}$$

where the perimeter of cell k is decomposed into edges Γ_e for $e \in E_k$, and $n_{k,e}$ ensures that outgoing fluxes are counted positively.

2.4 Slope limiting

From the Euler update-formula applied to the upwind scheme (Section 2.3.3), it is apparent that $\phi_k^{(n+1)}$ is a weighted average of $\phi_{k'}^{(n)}$, with k' the index of the nearest-neighbour cells. Furthermore, it can be shown that, for a small enough time step, the weights are positive. Therefore, $\phi_k^{(n+1)}$ belongs to the interval of values spanned by $\phi_{k'}^{(n)}$. Specifically, the maximum (resp. minimum value) of ϕ_k over all indices k is less (resp. greater) at time step $n+1$ than at time step n. It is then said that the scheme is monotonous (conditionally).

More generally, if each ϕ_e or ϕ_e^* is a positively-weighted average of nearby $\phi_{k'}$, then, after an Euler update, ϕ_k is again a positively-weighted average of nearby ϕ_k' (subject to the same time-step restriction) and the scheme is again

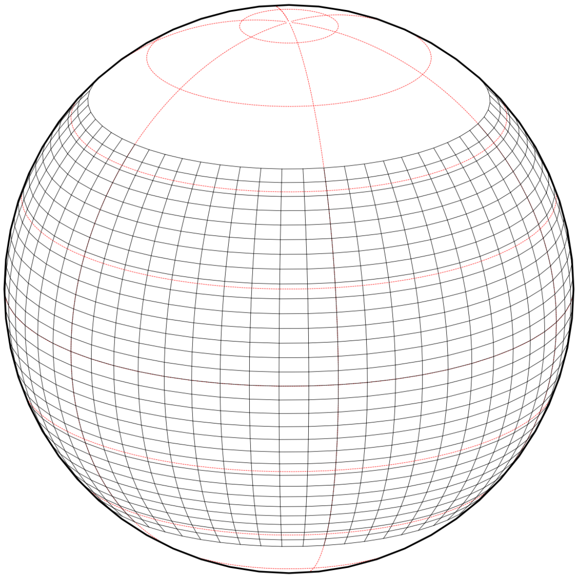

Figure 2.4: Cartesian mesh over the latitude band within the interval $[\frac{-\pi}{4}, \frac{\pi}{4}]$ on the globe, featuring 1800 cells

(conditionnally) monotonous. However, this condition on ϕ_e is not satisfied in general when a linear reconstruction is used to compute ϕ_e (or ϕ_e^* for SLFV). An extra step, called *slope limiting*, is introduced to enforce it, and therefore monotonicity, preventing the onset of spurious numerical oscillations (see Section 3.4.1). This extra step consists of multiplying $\nabla_k \phi$ by a coefficient $\alpha_k \in [0, 1]$. If $\alpha_k = 0$, the upwind scheme is recovered, while if $\alpha_k = 1$, the unmodified Green-Gauss gradient scheme (or SLFV scheme) is recovered. Thus, α should be as close to zero as required to guarantee monotinicity, but as close to 1 as possible to benefit from the higher accuracy brought by the linear reconstruction. In the present study, slope-reduction is enforced following the procedure detailed by Dubey et al. [2015] to compute α_k and ensure monotonicity.

Now that we have described the discretization strategies that we have implemented for Voronoi meshes, we briefly explain the ones we have chosen for the Cartesian mesh simulations.

2.5 Cartesian meshes

2.5.1 Cartesian-mesh generation and elements

We use a Cartesian mesh similar in essence to that used in the CHIMERE CTM. It is defined by taking the area on the surface of a sphere, which, using spherical coordinates, lies within the latitude range $[\frac{-\pi}{4}, \frac{\pi}{4}]$ and longitude range $[0, 2\pi]$. It hence forms a curved *rectangle*, fully revolved around the sphere, which we will refer to as *the latitude band* (Fig. 2.4). This surface is then divided into curved *rectangles*. This is done by taking evenly spaced longitudinal lines, intersecting a group of latitudinal lines, also evenly spaced. Each curved *rectangle* is a Cartesian mesh cell.

The Cartesian mesh used in this study has similar elements to those of the Voronoi mesh (Section 2.1.3). By virtue of the structured nature of the Cartesian mesh, the indexing of these elements is incremental starting from an origin, or reference point.

2.5.2 Operator splitting

Operator-splitting methods formulate a numerical solver for the problem :

$$\partial_t \Phi = f_1(\Phi) + f_2(\Phi) \tag{2.31}$$

(where the expressions $f_1(\Phi)$ and $f_2(\Phi)$ may involve partial derivatives) by composing solvers for the auxiliary problems:

$$\partial_t \Phi = f_1(\Phi) \tag{2.32}$$

$$\partial_t \Phi = f_2(\Phi) \tag{2.33}$$

Notice that even if each auxiliary problem is solved exactly, composing the auxiliary solvers to solve the main problem produces an error that depends on the splitting method and can be first-order in the time step, second-order, or higher-order. Commonly-used approaches include *Lie splitting*, which is of first-order, and *Strang splitting*, which is of second-order. We refer to [Mailler et al., 2021] for details.

The maximum order of accuracy that can be attained through splitting is the lowest order of accuracy among the used schemes, including 1D advection schemes and splitting strategies. Specifically, if a splitting strategy of a lower order than the order of the 1D advection schemes is used, the global order will be that of the splitting strategy. For instance, if second-order splitting is used with a third-order transport scheme, second-order accuracy only will be attained.

For the advection equation formulated in longitude-latitude coordinates, the auxiliary problems correspond to zonal (resp. meridional) transport and involve only derivatives with respect to longitude (resp. latitude). Furthermore, zonal (resp. meridional) advection along different constant-latitude (resp. constant-longitude) circles forms mutually independent problems. Thus, the ultimate building blocks are one-dimensional transport schemes.

2.5.3 One-dimensional transport schemes

We consider finite-volume schemes of first-, second- and third-order accuracy. The first-order scheme is the original Godunov scheme [Godunov, 1959], which the Voronoi upwind scheme (Section 2.3.3) generalizes to Voronoi meshes. The second-order scheme is the Van Leer method [Van Leer, 1977]. The SLFV scheme can be regarded as an extension of this scheme to Voronoi meshes. More specifically, the Van Leer method relies on a linear reconstruction in each cell and a semi-Lagrangian approach to time integration. As with SLFV, monotonicity is enforced by a slope-limiting technique.

The Piece-wise Parabolic Method (PPM) scheme [Colella and Woodward, 1984], [Carpenter et al., 1990] is also used in our study. The PPM scheme implements a semi-Lagrangian design similar to Van Leer [1977] but with a better accuracy due to a parabolic (instead of linear) reconstruction of ϕ in each cell. While formally third-order away from extrema in the advected field, the slope-limiting procedure presented in Colella and Woodward [1984] generates order-1 error terms in the immediate vicinity of extrema, preventing the scheme from formally reaching third-order accuracy [Colella and Sekora, 2008]. The PPM scheme—as described by Colella and Woodward [1984]—is therefore order-2, but generally more accurate than Van Leer [1977] (see, *e.g.*, Mailler et al. [2021]).

As discussed above, solvers for the two- and three-dimensional advection equations are obtained by combining these schemes with time splitting with the above-described strategies of Lie (order-1) and Strang (order-2).

Chapter 3

Two-Dimensional Test Cases

This chapter describes the various conditions which may be combined together to form complete test cases for 2D advection modelling. An initial concentration—or tracer mixing-ratio—distribution is required as a starting point, followed by a wind field which advects this concentration. Restrictions can be added to the wind fields to guarantee that the flow remains within the prescribed geographic domains covered by the mesh under study. The variation of these initial conditions allows to discover empirical scheme properties in an attempt to understand and compare them between different meshes.

Furthermore, the metrics used to assess the mesh-scheme pairs are described. Each metric addresses a numerical property of the used schemes. In the next chapter (Chapter 4), comparisons are made based on the metrics described herein.

3.1 Tracer-concentration distributions

The flowing fluid—in our case, the atmosphere—can carry one or more tracers. For a given wind field, the initial distribution of these tracers—that is, at an arbitrarily chosen origin of the time—is involved in determining the distribution of these tracers at any later time after being advected by the fluid. The chosen numerical method for simulating advection will affect the approximation of the new distribution of the tracers depending on the ability of the method to handle advection.

Different types of concentration—or tracer mixing-ratio—distributions are used to initiate the simulations. These different distributions permit to study different properties of the used schemes on the different meshes. For example, smooth distributions for two tracers related initially by a non-linear relationship allow to asses the schemes' abilities to preserve non-linear tracer relationships. Smooth distributions over relatively large patches permit to study scheme convergence. Distributions with sharp shapes, like slotted cylinders, permit to study how much the schemes preserve sharp changes in small areas.

The various initial concentration distributions used in the test cases of our study are detailed in this section, along with some of their applications. The metrics for which they are used are detailed in the section on metrics (3.4).

3.1.1 Uniform distribution

In such a distribution, the mixing ratio throughout the entire domain has only one value, in all mesh cells. This is particularly useful for easily detecting breaches in monotonicity, where any change from this uniform value accounts for the non-preservation of the maximum and minimum of the scalar field simultaneously. It is also useful for verifying the correctness of gradient calculation, as the correct concentration-gradient is exactly zero, everywhere. We do not show simulations initialized with a uniform mixing-ratio, as these experiments are rather preliminary checks to detect potential errors in the implementation of the schemes.

3.1.2 Double cosine-bell distribution

The cosine-bell is a smooth distribution with a sinusoidal variation between a background value and a maximum value (Eq. 3.1). In its double form, two cosine-bell-shaped *hills*, are allocated to two distinct parts of the domain.

In 2D, cosine *bells* actually have a circular shape, with a maximum concentration at a central point, decreasing in a smooth sinusoidal manner to reach a minimum value at the edge, matching the background value. Following Lauritzen and Thuburn [2012], we use cosine bells characterized by a common radius $R = 1/2$ (in radians) and by the coordinates (λ_n, θ_n) of their centers ($n = 1, 2$ for two cosine bells):

$$\phi(\lambda, \theta) = \begin{cases} b + c\, h\left(\frac{r_n(\lambda,\theta)}{R}\right), & \text{if } r_n(\lambda, \phi) < R \text{ with } n = 1, 2. \\ b, & \text{otherwise.} \end{cases} \tag{3.1}$$

where b and c are constants, $r_n(\lambda, \phi)$ is the great-circle distance from the center of cosine bell n, found as:

$$r_n(\lambda, \theta) = \arccos\left[\sin\theta_n \sin\theta + \cos\theta_n \cos\theta \cos(\lambda - \lambda_n)\right] \tag{3.2}$$

and $h(r)$ is the shape function :

$$h(r) = \frac{1}{2}\left[1 + \cos(\pi r)\right]. \tag{3.3}$$

b is the background mixing ratio, and $b + c$ is the maximum mixing ratio. $c, b \in [0, 1]$ are chosen so that $b + c = 1$, and the mixing ratio, ϕ, remains in the interval $[0, 1]$. When computing entropy (Section 3.4.4), a background value of 0 is necessary to eliminate any contribution to entropy coming from regions of the full hexagonal-pentagonal mesh beyond the limits of the Cartesian domain. Values $b = 0$ and $c = 1$ are used in this case. This pair of values is also used to investigate the positivity of the schemes, which is a prerequisite for studying the preservation of non-linear tracer-relationships, using, again, the same values. Otherwise, we use $b = 0.1$ and $c = 0.9$.

3.1.3 Single cosine-bell distribution

A simplified form of the above distribution, it is represented by only one of the two cosine bells, the location of which can be varied. Such a distribution is particularly useful for tracking a maximum mixing-ratio throughout space. With only one peak, the location of the maximum is unique. Similar to other smooth distributions, the single cosine-bell is useful when investigating a property such as convergence, where sharp discontinuities would prevent a useful comparison of the various schemes(such as the slotted-cylinder distribution used by Nair and Lauritzen [2010]). In this case, we use the parameters set as $b = 0.1$ and $c = 0.9$

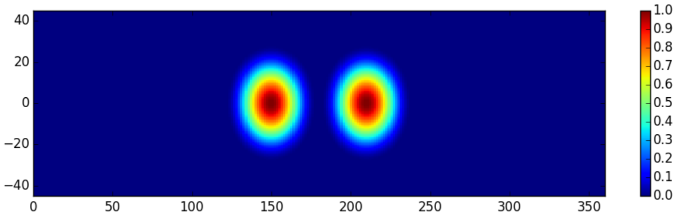

Figure 3.1: The cosine-bell concentration distribution used in this study, where the left axis is the latitude, θ, and the bottom axis is the longitude, λ, expressed in degrees. The right-side color-bar represents the tracer mixing-ratio values.

3.2 Wind fields

To study methods involved in solving the advection equations of wind flow, one of the main parameters to change in the test cases is the wind field. The magnitude of this field, its direction, and its mathematical properties (such as divergence) can be varied. These different properties permit to show the different capabilities of the used schemes. For example, simple solid-body rotational wind fields provide a good reference point for scheme comparisons. Time-dependent wind fields allow us to study the schemes' abilities to deal with time variation. Highly-deformational wind fields add more spatial difficulties to study the schemes' accuracies in following variations in space, and so forth.

For motion along the two-dimensional surface of a sphere, we define the two components of the wind-field velocity in terms of longitude, λ, latitude, θ, and time, t:

$$\boldsymbol{u} = u(\lambda, \theta, t)\boldsymbol{e_{\lambda}} + v(\lambda, \theta, t)\boldsymbol{e_{\theta}} \tag{3.4}$$

In simple cases, the components are independent of any one or more of these variables.

For non-divergent wind fields, a stream function can be defined. The expressions of the spherical wind components (on a 2D spherical surface) in terms of the stream function, Ψ, are as follow:

$$u = -\frac{1}{a}\frac{\partial \Psi}{\partial \theta}\ ,\ v = \frac{1}{a\cos\theta}\frac{\partial \Psi}{\partial \lambda} \tag{3.5}$$

where u is the zonal wind component, v is the meridional one, and a is the planetary radius. The expression of the stream function can be inversely formulated from the equations of the wind-field components:

$$\Psi = -a\int u\mathrm{d}\theta = a\cos\theta \int v\mathrm{d}\lambda. \tag{3.6}$$

The wind fields used in this study are defined in this section, with a description of their purposes. The metrics they are used with are specified in Section 3.4.

3.2.1 Solid-body rotation

A zonal solid-body-rotation wind field has the zonal and meridional components:

$$u(\lambda, \theta, t) = u_0 \cos\theta \tag{3.7}$$

$$v(\lambda, \theta, t) = 0 \tag{3.8}$$

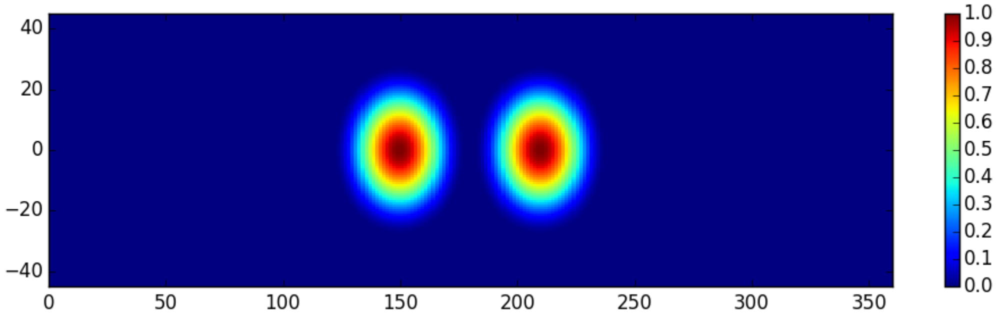

(a) Solid-body wind field, start of simulation

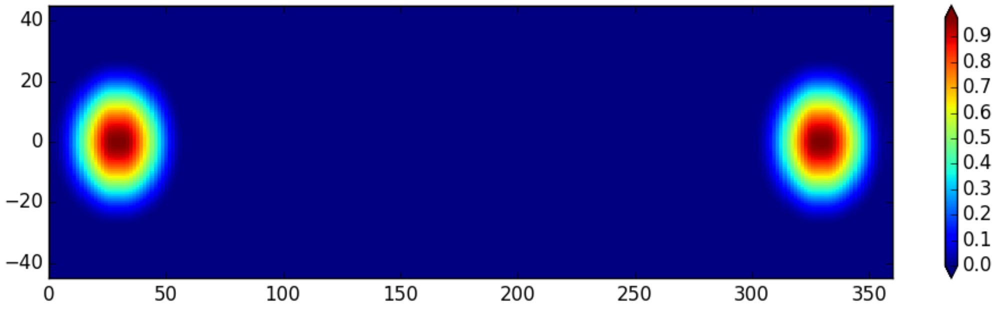

(b) Solid-body wind field, mid-simulation

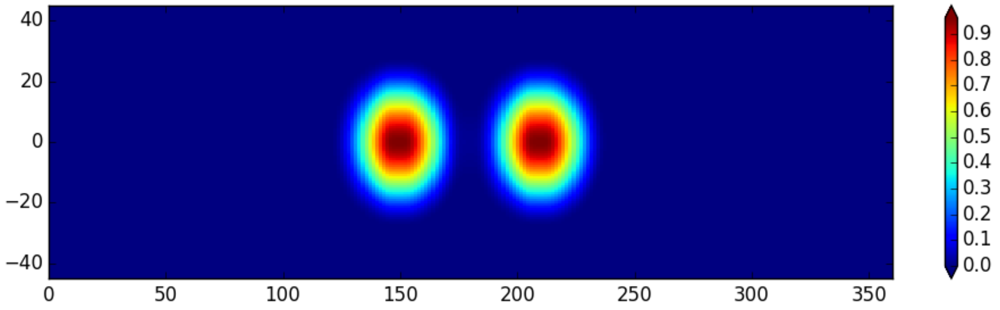

(c) Solid-body wind field, end of simulation

Figure 3.2: The solid-body wind field's simulated effect on a double cosine-bell concentration distribution at the start, middle, and end of a full-Earth rotation, following a van Leer scheme on a fine mesh. The left axis represents the latitude, the bottom axis the longitude, and the color bar represents the tracer mixing ratio.

where u_0 is the speed of wind at $\theta = 0$ (at the equator).

The expression for the stream function obtained from Eq. (3.6) is:

$$\Psi(\lambda, \theta, t) = -u_0 a \sin\theta. \tag{3.9}$$

This maximum-simplicity wind field was used by many authors, such as Prather [1986], Lin and Rood [1996] and Walcek [2000], to test their advection schemes. It is easy to implement [Freitas et al., 2011], and after a complete rotation, the solution of the tracer mixing ratio is exactly the same as the initial field (Figure 3.2). This aspect makes the comparison of the numerical solution to the exact solution simple, as well as the evaluation of properties of the scheme such as shape preservation, diffusion, and others (see Section 3.4).

3.2.2 Tilted solid-body-type periodic oscillation

Such a wind field is simple in its similarity to the ordinary solid-body field. However, it endows some challenges to the schemes through an inclination, while still avoiding strong deformations that increase numerical diffusion. A sinusoidal time-dependence guarantees the return of the scalar field to its initial position after a full period (Figure 3.3). These properties make this wind field a reasonable candidate for studying convergence, which requires a comparison between the numerical and exact solutions, the latter identical to the initial field distribution.

At the same time, by introducing a tilt of the wind field relative to the zonal direction, we reduce the advantage endowed to the Cartesian mesh by a solid-body wind-field aligned with the Cartesian grid. The tilt and wind speed are set in a way that ensures that no tracer mass is transported beyond the boundaries of the Cartesian domain.

To define this field, we begin with the classical solid-body rotation around the axis passing through the two poles. A tilt is made to the axis of rotation, such that it is skewed away from the pole axis by an angle α. If we define the sphere of radius a as the surface $x^2 + y^2 + z^2 = a^2$ in a three-dimensional Cartesian system (x, y, z), this is represented by a skew from the z-axis, within the z and x plane, with no change along y. The tilted axis has the (λ, θ) coordinates $(0, \frac{\pi}{2} - \alpha)$, where α is the tilt angle in radians. In terms of 3D (x, y, z) coordinates, the tilted axis can be expressed as follows:

$$\boldsymbol{e_\alpha} = \begin{pmatrix} \sin\alpha \\ 0 \\ \cos\alpha \end{pmatrix} \tag{3.10}$$

which falls back to the pole axis $\boldsymbol{e_z}$ when the tilt is zero. At any point $(a\cos\theta\cos\lambda, a\cos\theta\sin\lambda, a\sin\theta)$ on the surface of the sphere, the wind-field stream-function is:

$$\Psi(\lambda, \theta, t) = -u_0 a \cos\left(\frac{2\pi t}{T}\right) \boldsymbol{e_r} \cdot \boldsymbol{e_\alpha} \tag{3.11}$$

with:

$$\boldsymbol{e_r} \cdot \boldsymbol{e_\alpha} = a\left(\cos\theta\cos\lambda\sin\alpha + \sin\theta\cos\alpha\right) \tag{3.12}$$

and the zonal and meridional wind components ensuing from the above expression. u_0 is taken as $u_0 = \frac{2\pi a}{T}$ to ensure a full rotation during the simulated time, T, in the absence of a sinusoidal time dependence.

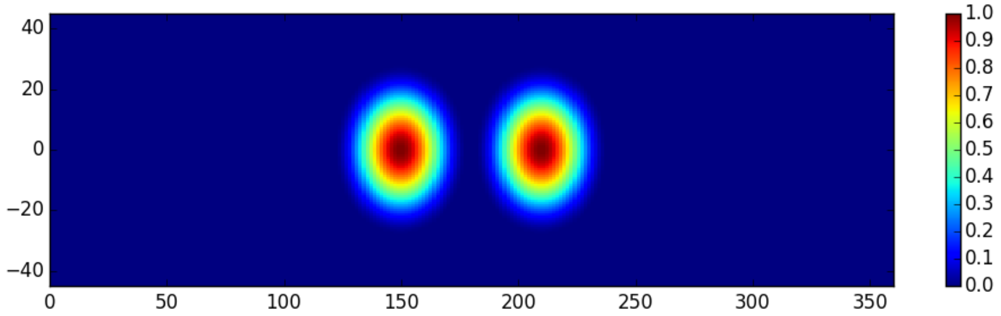

(a) Tilted solid-body wind field, start of simulation

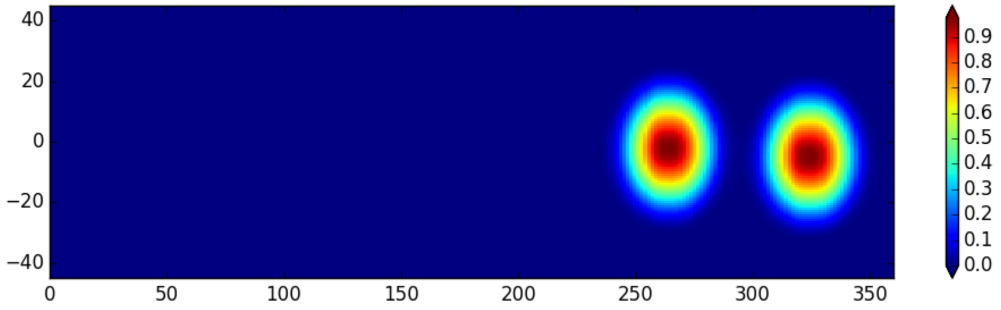

(b) Tilted solid-body wind field, mid-simulation

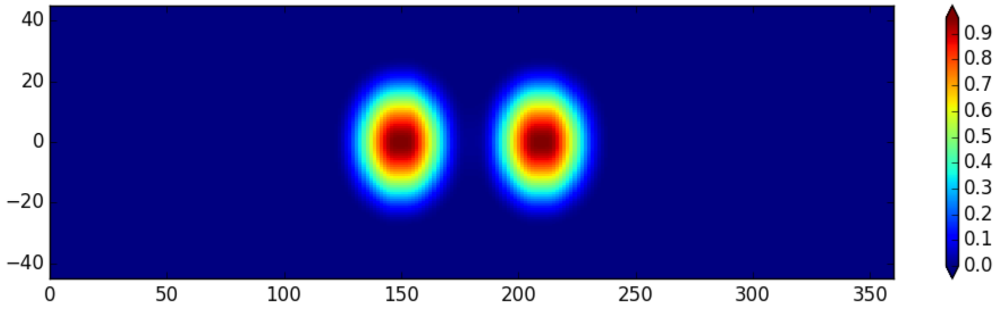

(c) Tilted solid-body wind field, end of simulation

Figure 3.3: The tilted solid-body wind field's simulated effect on a double cosine-bell concentration distribution at the start, middle, and end of a full-Earth rotation, following a van Leer scheme on a fine mesh. The left axis represents the latitude, the bottom axis the longitude, and the color bar represents the tracer mixing ratio.

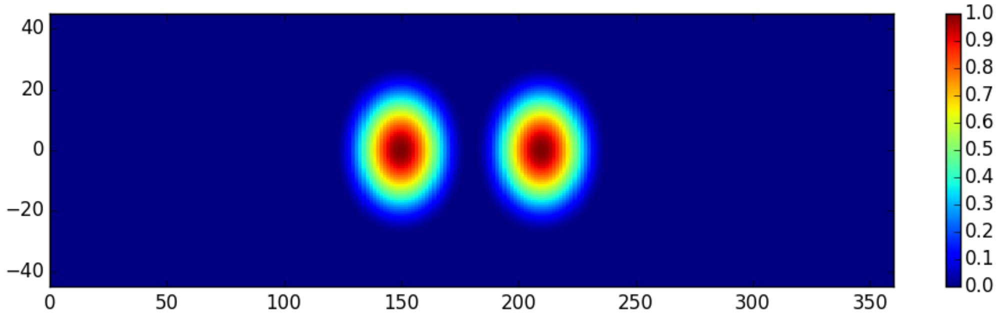

(a) NL2010 wind field, start of simulation

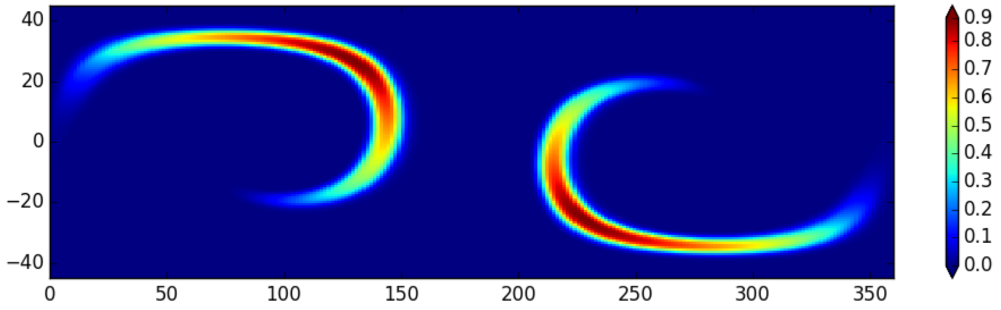

(b) NL2010 wind field, mid-simulation

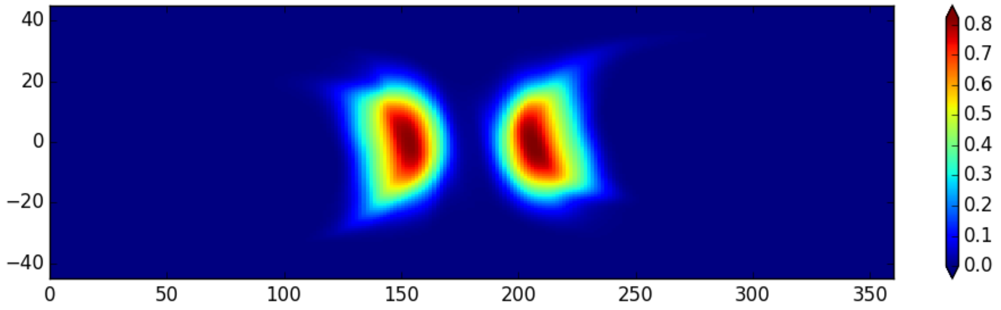

(c) Solid-body wind field, end of simulation

Figure 3.4: The NL2010 wind field's simulated effect on a double cosine-bell concentration distribution at the start, middle, and end of a full-Earth rotation, following a van Leer scheme on a fine mesh. The left axis represents the latitude, the bottom axis the longitude, and the color bar represents the tracer mixing ratio.

3.2.3 Dual vortex with solid-body rotation (NL2010)

This wind field was first proposed by Nair and Lauritzen [2010]. It results from the superposition of a zonal solid-body rotation and the wind fields induced by two vortices, which also move with time. The aim of this design is to produce large deformations (i.e. if we let a pair of points follow the wind field, it is possible for a pair of initially close points to be widely separated later). Conversely, it is possible for a pair of initially well-separated points to become very close to each other after some time following such wind. If these two points carry different values of a tracer, this will result in a large change in tracer concentration over a short distance. Figure 3.4 illustrates the deformational character of this flow. The presence of sharp fronts challenges the capacities of numerical schemes.

The zonal component of this field is expressed as:

$$u(\lambda, \theta, t) = K \sin\left(\lambda - \frac{2\pi t}{T}\right) \sin(2\theta) \cos\left(\frac{\pi t}{T}\right) + \frac{2\pi a}{T} \cos\theta. \tag{3.13}$$

It can be noted that the zonal component is the sum of both a solid-body translation:

$$\frac{2\pi a}{T} \cos\theta \tag{3.14}$$

and the zonal velocity due to the vortices:

$$K \sin\left(\lambda - \frac{2\pi t}{T}\right) \sin(2\theta) \cos\left(\frac{\pi t}{T}\right) \tag{3.15}$$

where K is the amplitude of the vortical flow, while $2\pi a/T$ is the amplitude of the solid-body rotation.

On the other hand, the meridional component of this wind field comes solely from the meridional motion due to the vortices, and is expressed as:

$$v(\lambda, \theta, t) = K \sin\left(\lambda - \frac{2\pi t}{T}\right) \cos(\theta) \cos\left(\frac{\pi t}{T}\right). \tag{3.16}$$

In the above equations, T is the total time for a full rotation, a is the planetary radius, and K is the amplitude of the vortical flow. Nair and Lauritzen [2010] set K to :

$$K = \frac{10a}{T}. \tag{3.17}$$

We use this canonical value with this wind field, except in Section 3.4.3 where it is useful to consider lower values.

The expression for the stream function obtained from Eq. 3.6 is:

$$\Psi(\lambda, \theta, t) = aK \sin^2\left(\lambda - \frac{2\pi t}{T}\right) \cos^2\theta \cos\left(\frac{\pi t}{T}\right) - \frac{2\pi a^2}{T} \sin\theta \tag{3.18}$$

where the vortex motion is accounted for by the first term:

$$\Psi_{\text{vortex}} = aK \sin^2\left(\lambda - \frac{2\pi t}{T}\right) \cos^2\theta \cos\left(\frac{\pi t}{T}\right) \tag{3.19}$$

and the solid-body motion is accounted for by the second term:

$$\Psi_{\text{SB}} = -\frac{2\pi a^2}{T} \sin\theta. \tag{3.20}$$

3.3 Limiting to the Cartesian band

The Voronoi mesh used in this study covers the full sphere, while the Cartesian mesh domain covers only the latitude band $[\frac{-\pi}{4}, \frac{\pi}{4}]$. To make comparisons on similar grounds, we first ensure that the initial tracer-distribution falls entirely in the latitude band covered by the Cartesian domain, and remains there as it is advected. Nothing complementary needs to be done for the zonal solid-body rotation. As for the tilted periodic solid-body rotation, we check that the tilt is small enough to satisfy the mentioned constraints. Less simply, for the dual vortex with solid-body rotation, the constraints are only satisfied by taking special measures. In this case, we define a re-scaled latitude:

$$\theta'(\theta) = \begin{cases} 2\theta, & \text{if } \theta \in \left[\frac{-\pi}{4}, \frac{\pi}{4}\right]. \\ \frac{\pi}{2}, & \text{if } \theta > \frac{\pi}{4}. \\ -\frac{\pi}{2}, & \text{if } \theta < \frac{-\pi}{4}. \end{cases} \tag{3.21}$$

with a resulting new streamfunction:

$$\Psi'(\lambda, \theta, t) = \Psi(\lambda, \theta', t) \tag{3.22}$$

where we then define the wind field from Ψ' instead of Ψ. Since, by design, Ψ' is constant for $\theta > \pi/4$ and for $\theta < -\pi/4$, there is no flow crossing latitudes $\theta = \pm\pi/4$. Furthermore, as the zonal solid-body rotation is not problematic, we apply this transformation only to the vortex part:

$$\Psi'(\lambda, \theta, t) = \Psi_{\text{vortex}}(\lambda, \theta', t) + \Psi_{\text{SB}}(\lambda, \theta, t) = ak \sin^2\left(\lambda - \frac{2\pi t}{T}\right) \cos^2\theta' \cos\left(\frac{\pi t}{T}\right) - \frac{2\pi a^2}{T} \sin\theta \tag{3.23}$$

where the last term, $-\frac{2\pi a^2}{T} \sin\theta$, accounts for the solid-body rotation.

The velocity components are obtained by substituting the new expression of the stream function in the expressions of (3.2). Thus, the expressions of the translated field's zonal and meridional components become, respectively:

$$u'(\lambda, \theta, t) = \begin{cases} 2k \sin^2\left(\lambda - \frac{2\pi t}{T}\right) \sin(4\theta) \cos\left(\frac{\pi t}{T}\right) + \frac{2\pi a}{T} \cos\theta, & \text{if } \theta \in [\frac{-\pi}{4}, \frac{\pi}{4}]. \\ \frac{2\pi a}{T} \cos\theta, & \text{if } \theta > \frac{\pi}{4}. \\ \frac{2\pi a}{T} \cos\theta, & \text{if } \theta < \frac{-\pi}{4}. \end{cases} \tag{3.24}$$

$$v'(\lambda, \theta, t) = \begin{cases} \frac{1}{2\cos\theta} k \sin\left(2\lambda - \frac{4\pi t}{T}\right) \cos^2(2\theta) \cos\left(\frac{\pi t}{T}\right), & \text{if } \theta \in [\frac{-\pi}{4}, \frac{\pi}{4}]. \\ 0, & \text{if } \theta > \frac{\pi}{4}. \\ 0, & \text{if } \theta < \frac{-\pi}{4}. \end{cases} \tag{3.25}$$

3.4 Metrics

In order to assess the properties of the numerical methods, some metrics are put in place. To provide a reference for assessment, schemes of similar order and functionality are applied on the Cartesian and Voronoi meshes. The performance of the Cartesian schemes, under the same set of metrics, is used as a baseline for comparison. These metrics will be detailed in this section.

In addition to these metrics, other basic validation criteria are tested for the used schemes paired to the studied meshes. To start, the numerical gradient used in the gradient-corrected schemes is validated through the use of uniform-concentration fields, where the gradient must be zero. Also, mass conservation is validated by tracking the total mass of all species at each time step of the numerical iterations.

3.4.1 Stability

Scheme stability is the property that the numerical solution remains within physically allowed bounds, whose definition depends on the behaviour of the exact solutions of the problem. For advection, an important property of the exact solution is that—if the initial mixing ratio is bounded—it remains bounded. A simple criterion for scheme stability is, therefore, that the absolute value of the numerically-computed mixing-ratio must remain bounded. As mentioned in the introduction, for the schemes considered here, stability is conditional. The Courant number, C, for example, must not exceed a certain threshold:

$$C = \frac{u\Delta t}{\Delta x} \tag{3.26}$$

where u is the maximum wind speed and Δx is a length characterizing the smallest cell in the mesh. For Voronoi meshes, we define Δx as the length of the shortest dual-cell edge d_e, or equivalently, the shortest distance between primal-cell centers.

The critical Courant number C_{crit}—i.e. the value of C below which the numerical solution remains bounded—depends on the scheme. To obtain its precise value empirically rather than from a formal proof, we perform numerical simulations and compare the maximum concentration of the simulated concentration-field to its initial value. An initially small value, $C \ll 1$, is chosen, from which the time step is computed. The simulation is repeated while gradually increasing C and the time step. The maximum concentration should remain below the initial maximum for the scheme to be considered stable. When the simulated values begin to overshoot the initial maximum, we say that the corresponding Courant number is our estimate of C_{crit}. Increasing the time step beyond this threshold causes instabilities for the used numerical scheme.

Higher values of C_{crit} are desirable, as the computational work for a given simulation is proportional to $T/\Delta T$, with T the full duration of the simulation. A scheme with a relatively lower C_{crit} than others is considered less stable, while a scheme with a relatively higher threshold value is considered more stable.

For operational simulations, the mesh is fixed, and the maximum value of the wind speed is known or estimated in advance. Thus, knowing the value of the critical Courant-number, the Courant-Friedrichs-Lewy condition:

$$C < C_{\text{crit}} \tag{3.27}$$

becomes a guideline used to set the time step, Δt.

3.4.2 Monotonicity

Another property—more stringent than boundedness—of the exact solutions of the advection equation is that the values of the mixing ratio remain within their initial interval of values. *Monotonicity* is the property of a numerical scheme that enforces the same property for numerical solutions. It is, therefore, a more stringent notion of stability. Monotonicity can be violated by the numerical scheme in one of two ways:

- returning values beyond the initial maximum, or

(a) Initial time (analytical solution)

(b) Final time with PPM scheme

(c) Final time with van Leer scheme

(d) Final time with upwind scheme

Figure 3.5: The deviation of the simulated solution from the analytical solution (a), after a simulated full Earth rotation following the PPM scheme (b), the van Leer scheme (c), and the upwind scheme (d) under the NL2010 wind field on a fine mesh. The left axis represents the latitude, the bottom axis the longitude, and the color bar represents the tracer mixing ratio. The deviation from the analytical solution forms the basis for convergence measurement.

- returning values below the initial minimum,
    - ○ sometimes yielding negative values for an initially strictly positive field.

Definition 3.4.1 (Positivity)**.** Positivity is the numerical scheme's ability to preserve positive values. When the lower bound of the scalar field's value interval is zero, positivity can be studied by following the monotonicity at the lower bound.

Schemes which are mathematically proven to be monotonous are usually monotonous under certain criteria only. Usually, the latter is the condition that the Courant number remains below a certain critical value, as with stability.

Again in a similar way to stability, to numerically test the monotonicity of the used schemes, the latter are run under increasing Courant numbers. The final Courant number beyond which monotonicity is breached is deemed the *threshold* Courant number for the monotonicity of the given scheme.

3.4.3 Convergence

Convergence is the property that the numerical solution approaches the exact solution as the mesh is refined. We note that, to ensure stability, the time step is also implicitly refined proportionally to the mesh resolution, Δx. A quantitative measure of convergence is the order of accuracy of a scheme. For a scheme of order p, the discrepancy between the exact and numerical solutions decreases as $(\Delta x)^p$.

To quantify convergence, we calculate the root-mean-square error (RMSE) of the simulated tracer mixing ratio relative to an analytical solution. This is done by taking an advection test which returns the tracer field to its initial distribution at the end of the simulation. The difference between the simulated field at the final location, and the initial field at the initial location—which represents the analytical solution—forms the basis for this error calculation (Figure

3.5). We sum the squares of the differences in each cell between the initial and final times, then divide by the total area represented by the considered mesh cells, and find the square root:

$$\text{RMSE} = \sqrt{\frac{\sum_{k=1}^{N} A_k (\phi_k^n - \phi_k^0)^2}{\sum_{k=1}^{N} A_k}} \tag{3.28}$$

where A_k is the cell area, ϕ_k^n is the simulated tracer mixing-ratio in cell k at the final time, and ϕ_k^0 is the initial value of the tracer mixing-ratio in cell k (or the analytical solution at the final time).

Using this equation, we find the root-mean-square errors for both the Cartesian and Voronoi meshes at coarse, intermediate, and fine resolutions. The RMSE of first-order accurate schemes will decrease at a rate proportional to the cell size Δx of the used mesh. Second- and third-order-accurate schemes have errors decreasing with rates proportional to the squares and cubes of the mesh-cell size, respectively.

The test case for this metric requires a smooth concentration distribution. Indeed, the design of higher-order schemes relies on Taylor expansions, which are only valid if the exact solutions have enough existing and continuous successive derivatives. A counter-example would be a distribution with discontinuities, or with a discontinuous gradient. We use a wind field that is not too deformational to make sure that the solution is well-resolved at all times, even on coarse meshes. We could thus choose the zonal solid-body rotation, which is not sheared. However this wind field is aligned with the Cartesian grid and potentially introduces a bias in its favor. We therefore choose to use the tilted periodic solid-body wind-field. In addition to this field, other test cases with more demanding fields are used to illustrate their effects on convergence.

3.4.4 Numerical diffusion

Numerical diffusion—visualized in Figure 3.6—is an *umbrella name* for numerical artifacts which resemble the effect of adding a diffusion term to the advection equation. In fact, for simple schemes—such as the Godunov scheme in one dimension—it may be possible to decompose the numerical scheme into a higher-order part and a residual which is a discretization of a diffusive flux. We use two metrics to identify and quantify these artifacts empirically: the entropy, and the preservation of non-linear tracer-relationships.

Entropy

The maximum value of exact solutions of an advection-diffusion equation decreases with time. The physical interpretation of this phenomenon is that diffusion lets the fluid parcel where the maximum mixing ratio occurs mix with neighbouring parcels with a lower mixing ratio, resulting in a decrease of the mixing ratio of that fluid parcel. Thus, one measure of numerical diffusion is the decrease of the maximum value of the numerical solution.

As the maximum value depends on only one grid point of the numerical simulation, it may be preferable to construct a more integral quantity measuring the amount of mixing occurring in the numerical simulation. For this, we compute an entropy, inspired from statistical physics [Lauritzen and Thuburn, 2012], but with the Boltzmann constant dropped:

$$S_\phi = -\sum_{k=1}^{N} \phi_k \log \phi_k \rho_k A_k \tag{3.29}$$

where A_k is the cell area, and N is the total number of considered mesh cells.

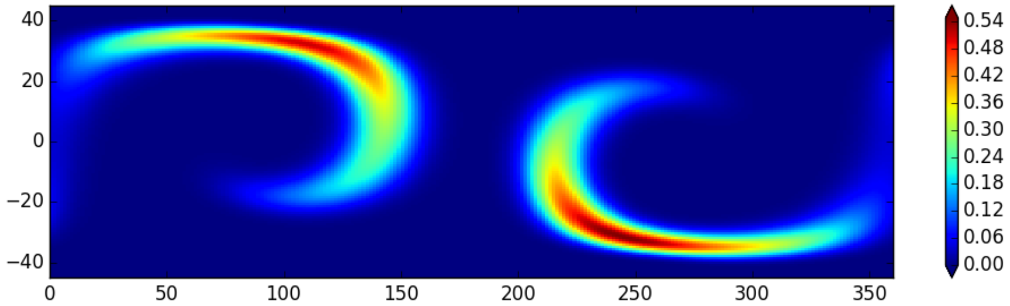

(a) Upwind scheme

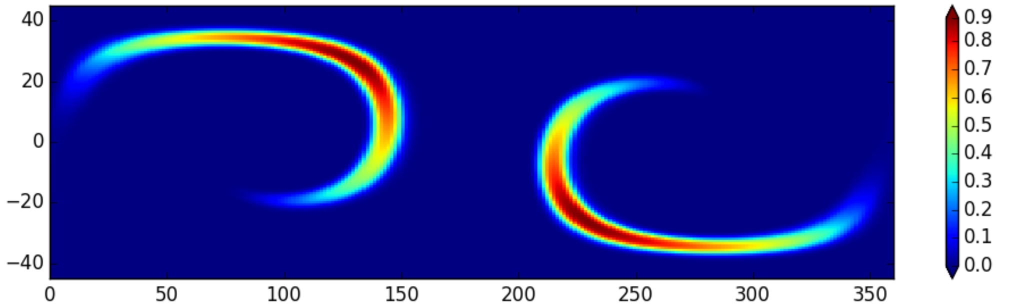

(b) Van Leer scheme

Figure 3.6: The difference in the numerical diffusion of a double cosine-bell initial concentration field visualized between a more-diffusive scheme (the upwind) and a less-diffusive scheme (the van Leer), after a half Earth-rotation under the NL2010 wind field on a fine mesh. The left axis represents the latitude, the bottom axis the longitude, and the color bar represents the tracer mixing ratio.

This metric is an approximation of a similar quantity—computable from the exact solution by replacing the sum by an integral—which is analogous to Ludwig Boltzmann's entropy in statistical mechanics. The latter is a measure of *mixed-up-ness* of a physical system as Josiah Willard Gibbs put it [Gibbs et al., 1906]. A uniform concentration distribution has a maximum entropy as per this definition, where the mixing is complete. Furthermore, the entropy of exact solutions of the advection equation is constant. Thus, variations of S_ϕ are numerical artifacts which indicate how much the initial field is spreading within the domain, as the time of the simulation progresses. The more *evenly spread* the field, the more it is diffused, and the lower the field's maximum value is relative to the initial maximum. Higher entropy is therefore regarded as an undesired property, while lower entropy is preferred for a numerical scheme.

The metric accounting for increase in entropy—to reflect the amount of diffusion—is defined in this study as:

$$S_\phi - S_\phi^0 \tag{3.30}$$

where ϕ_k is the field's value at the cell k, ρ_k is the density of the carrier fluid in the cell, A_k is the area of the cell, and S_ϕ^0 is the initial entropy found using the initial tracer mixing ratio distribution plugged into Eq. 3.29.

To study this metric, we use a cosine-bell smooth initial distribution with a zero background value to omit contributions from the Voronoi mesh cells beyond the Cartesian mesh bounds. The smooth distribution allows the schemes to transport the scalar field smoothly, to better represent small changes in mixing. Various wind fields are used to show the different effects of different wind properties on mixing.

Preservation of non-linear relationships

A more complete picture of numerical diffusion can be obtained by advecting two tracers, ϕ_1 and ϕ_2, by the same wind field and enforcing a non-linear relationship between mixing ratios at the initial time. Fig. 3.7 shows an example of a non-linear tracer relationship between two tracers, whose equation represented by the green curve is:

$$\phi_2 = -0.8(\phi_1)^2 + 0.9 \tag{3.31}$$

If the advection equation were solved exactly, this relationship would remain true at all times. Thus, any deviation from the initial relationship between the two tracers is a purely numerical artifact.

We can classify empirically observed artifacts as *physical* and *unphysical*. Observed effects are deemed *physical* if it is possible to obtain them by adding a diffusion term to the advection equation. For instance, by mixing two nearby fluid parcels A and B with mixing ratios ϕ_1^A, ϕ_2^A and ϕ_1^B, ϕ_2^B, we obtain a new fluid parcel, C, whose mixing ratios, ϕ_1^C, ϕ_2^C, are obtained from the original ones by a certain positively weighted average. If we plot the three points ϕ_1^X, ϕ_2^X, $X = A, B, C$ in a two-dimensional diagram, then C belongs to the segment AB.

In addition to this physical mixing, some numerical *unmixing* can occur. The latter will apparently decrease the diffusion and make the scheme look better than it should if looked at only through the lens of entropy. Such artifacts can be detected by classifying the non-preservation of a non-linear relationship as illustrated in Fig. 3.7.

On the graph, the possible range of simulated values is divided into regions based on the physical or numerical phenomenon behind the obtained values. Any tracer mixing ratio value pairs on the convex curve are *exact* in the sense that they have not undergone any mixing values. Points lying within the convex hull and above the line joining the two maxima of the tracer mixing ratios represent values obtained from real mixing. Points falling between both the minima and maxima of the tracer mixing ratios, but outside the real mixing region, account for *range-preserving unmixing*. Points below the minima account for undershooting, while points beyond the maxima account for overshooting.

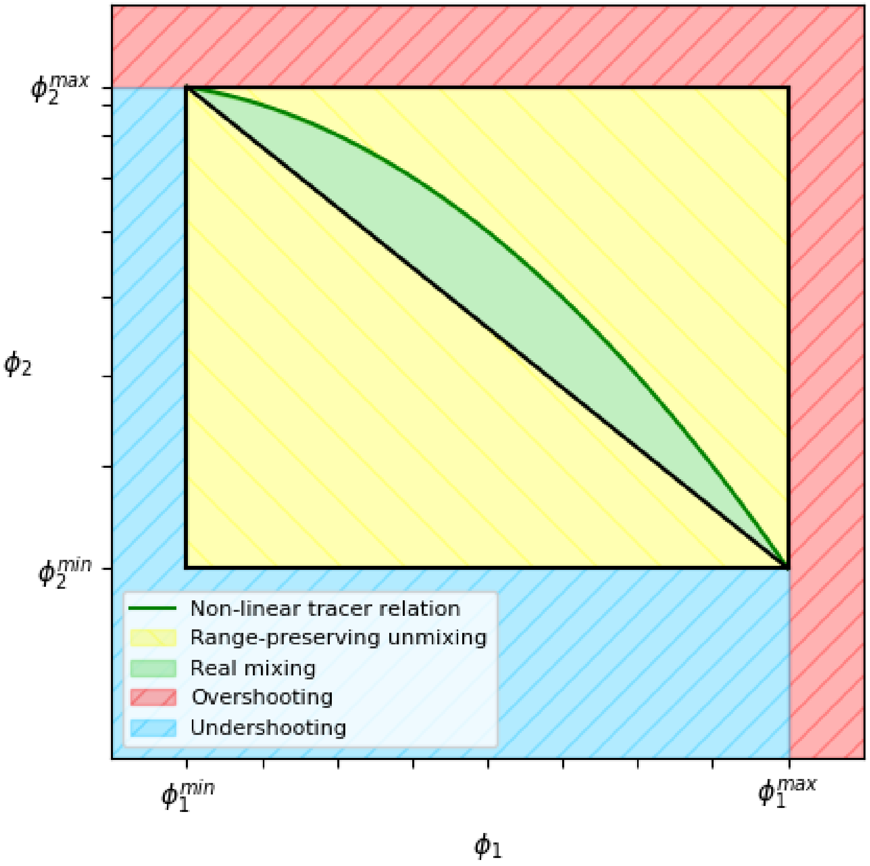

Figure 3.7: The classification of numerical mixing based on the violation of non-linear tracer-relationships

To study the preservation of non-linear relationships, a smooth concentration field with a well-defined shape over a designated area is needed, such as the double cosine-bell field. Each tracer is taken to have an *inverse* cosine-bell distribution to the other, where the first tracer's maximum is at the second tracer's minimum, and vice versa. Similarly to the case of entropy, different wind fields are used to show the effects of their different properties on two-tracer diffusion.

Chapter 4

Findings on the Numerical Mesh-Scheme Pairs in 2D

The following chapter highlights the results obtained based on stability, monotonicity, diffusivity, and convergence metrics for simulations on two-dimensional grids, on both a quasi-uniform unstructured hexagonal-pentagonal Voronoi mesh and a uniform structured Cartesian mesh. The metric measurements are presented, and the mesh-scheme pairs are evaluated as compared to each other.

Common test cases were used for each metric to ensure a fair comparison between the two frameworks with the used schemes. When using the method of lines for time integration, each spatial scheme was paired with a time scheme of equal order to avoid order reduction. Furthermore, as the Cartesian mesh is defined over a latitude band of interval $[-\frac{\pi}{4}, +\frac{\pi}{4}]$—and not the entire sphere—the resolutions were defined in such a way that the number of cells of the Voronoi mesh falling within this band was as close as possible to the total number of cells of the Cartesian mesh. Table 4.1 summarises the numbers of cells taken for each refinement.

4.1 Stability

Following the description of stability in Section 3.4.1, the mathematical expressions of all used schemes can be analytically proven to be stable under some constraints, or after slope-limiting [Colella and Woodward, 1984], [Godunov, 1959], [Dubey et al., 2015], [Van Leer, 1977]. Stability is expected to be affected only by the maximum wind speed of the wind field under consideration, as expressed by the Courant number (Eq. 1.4). Hence, to verify the analytical

Domain	Coarse refinement	Intermediate refinement	Fine refinement
Voronoi on the full sphere	2562	10242	40962
Voronoi in the meridional band	1812	7242	28965
Cartesian in the meridional band	1800	7200	28800

Table 4.1: Number of 2D mesh cells of each mesh type for the used refinements

expectations of the Voronoi-mesh schemes numerically, we ran a test case for a range of values of the Courant number (in the sequel, we refer to the Courant number as *the CFL*, in a slight abuse of nomenclature, but for the sake of brevity). As all used wind fields have a maximum wind speed of similar order, any one of them can be used to study scheme stability. To avoid the directional bias that a solid-body wind field may give to the Cartesian mesh, the tilted solid-body wind field was used. A full Earth rotation with a realistic wind velocity amplitude was used so that stability following real simulations can be checked, and hence a simulation length of 12 simulated days. The test cases are summarized in Table 4.2.

We use an initial concentration field with a 0.1 tracer mixing ratio background value, and a maximum value of 1, in a cosine-bell distribution. A maximum of 1 allows us to immediately detect increases, following a logarithmic representation. More precisely, we follow—with increasing CFL—the evolution of the *amplification factor* of the maximum tracer mixing ratio at the final time, ϕ^N_{max}, with respect to the initial maximum, ϕ^0_{max}:

$$\log \frac{\phi^N_{\text{max}}}{\phi^0_{\text{max}}}. \tag{4.1}$$

This factor suits to amplify any small changes from the initial maximum by virtue of the logarithm, and eases the detection of stability breaches.

Remark. *Establishing stability is necessary for monotonicity, and is sufficient to verify the preservation of the upper bound of the tracer mixing ratio interval.*

To verify the stability of the used schemes, we plot the maximum simulated tracer mixing ratio at the end of the simulation, at time N, versus the increasing CFL (Figure 4.1). As the initial concentration field has a cosine-bell distribution, with a maximum mixing ratio of $\phi = 1$, we follow the variation of the simulated maximum tracer mixing ratio relative to a value of 1, indicated on the figure with a dotted horizontal black line.

As can be seen in Figure 4.1, the maximum tracer mixing ratio simulated by the upwind scheme begins at a value below 1, due to the diffusive behavior of this scheme, whatever the CFL. As the CFL increases, the upwind scheme maintains the tracer mixing ratio maximum below 1, until it begins to increase abruptly at a CFL of about 1.4. On the other hand, the Gauss-Heun and SLFV schemes simulate a tracer mixing ratio maximum closer to 1, which can be attributed to their lower diffusivity, as will be seen in the following sections. As the CFL increases, both Gauss-Heun and SLFV schemes maintain the maximum tracer mixing ratio close to 1, until the SLFV scheme incurs abrupt increases at a CFL of about 1.15, while the Gauss-Heun scheme incurs abrupt changes beyond that value, at a CFL of about 1.3.

Therefore, all schemes are stable at a CFL of 1, and up to some vlaues beyond it. The SLFV scheme is stable up to a CFL of 1.15, followed by the Gauss-Heun scheme which it stable up to CFL 1.3, then the upwind scheme which is stable up to CFL 1.4. It can be seen that the higher order of SLFV and Gauss-Heun schemes comes at a certain cost in stability compared to the first-order upwind scheme.

4.2 Monotonicity

Similarly to stability, the mathematical expressions of all used schemes can be analytically proven to be monotonous under some constraints, or after slope-limiting [Colella and Woodward, 1984], [Godunov, 1959], [Dubey et al., 2015], [Van Leer, 1977]. Monotonicity is expected to be affected only by the same factors as stability, that being summarized by the CFL number. We hence adopt the same test case as that undertaken for stability, summarized in Table 4.3.

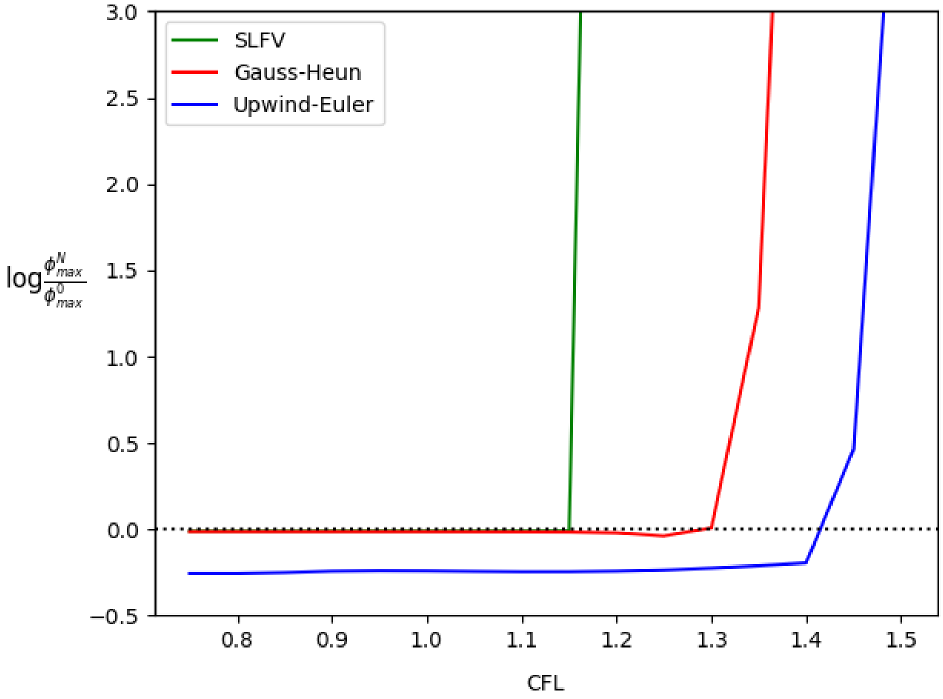

Figure 4.1: The amplification factor of the simulated maximum tracer mixing ratio versus CFL under the tilted, periodic solid-body wind field using all Voronoi schemes on the refined mesh. The dotted black line is a reference for the initial maximum tracer mixing ratio.

Parameter	Value
Initial Concentration	Cosine-bells, with $\phi \in [0.1, 1.0]$
Wind Field	Tilted, periodic solid-body
Courant Number	[0.7, 1.5]
Simulation Length	12 days
Number of Tracers	1
Refinement	Fine

Table 4.2: 2D stability test case

Parameter	Values
Initial Concentration	Cosine-bells, with $\phi \in [0.1, 1.0]$
Wind Field	Tilted, periodic solid-body
Courant Number	[0.75, 1.2]
Simulation Length	12 Days
Number of Tracers	1
Refinement	Fine

Table 4.3: 2D monotonicity test case

In this section, we verify the monotonicity of the Voronoi-mesh schemes as described in Section 3.4.2. Stability is sufficient to demonstrate the preservation of the upper bound, so the study of monotonicity only requires a demonstration of the preservation of the lower bound of the tracer mixing ratio range. The following part discusses this issue, by monitoring the simulated lower bound, in the same simulations as those used in the previous section.

Figure 4.2 shows the variation of the final simulated minimum mixing ratio from the initial minimum mixing ratio, versus the CFL. This variation is again expressed in terms of an amplification factor whose logarithm is taken to enhance small changes from the initial value. The expression $\log \frac{\phi^N_{\text{min}}}{\phi^0_{\text{min}}}$ is the minimum-tracer-mixing-ratio amplification-factor. When the initial value is maintained, an amplification factor of 0 is maintained. Any decrease from this initial value is seen as a plunge of the amplification factor towards negative values, while an increase is seen as a climb beyond zero. Deviations only in the negative direction from zero imply a non-preservation of the monotonicity.

Following the values of the simulated minimum mixing ratio compared to the initial minimum in Fig. 4.2, we see that as the CFL increases from 0.75 to 1, the logarithm of the computed fraction remains zero with all schemes. At a CFL of about 1.25, the Gauss-Heun scheme is the first to display negative values, and hence a decrease from the initial minimum, followed by the upwind-Euler scheme at a CFL of 1.3. Since the SLFV scheme does not produce negative values by virtue of slope limiting (Section 2.4), it remains monotonous until its stability limit obtained in the previous section, at a CFL of about 1.15

Therefore, SLFV maintains monotonicity up to a CFL of about 1.15, Gauss-Heun up to about 1.25, and upwind up to about 1.3, verifying—and even exceeding—the theoretically expected threshold values.

4.3 Numerical diffusion

A measure of numerical diffusion is performed on both mesh types in order to compare the two. After verifying the monotonicity and stability of the used schemes up to a CFL of 1, we evaluate the remaining metrics at a CFL below this bound to remain in a stable and monotonous interval with high confidence. For this reason, a CFL of 0.8 is chosen. The added abbreviation, *-SL*, to the Van Leer and PPM scheme names in the graphs of the following sections refers to the fact that they were implemented with slope-limiting to maintain monotonicity.

As discussed in Chapter 3, we obtain insight onto numerical diffusion from two perspectives: by monitoring the increase of entropy of a single tracer, and by examining to which extent—and in which way—the preservation of a nonlinear relationship between two tracers is violated.

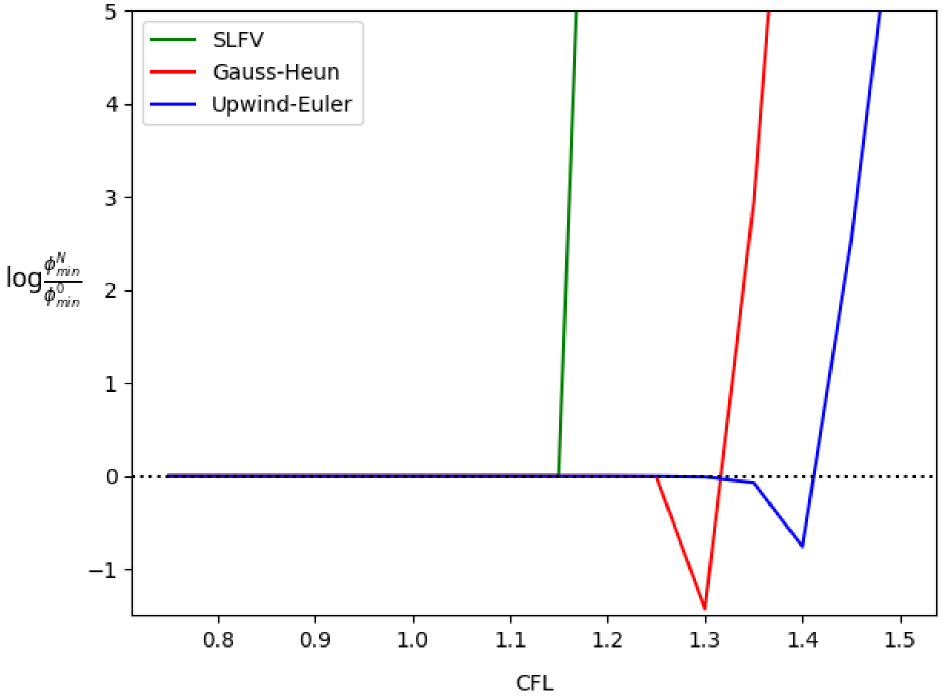

Figure 4.2: The amplification factor of the simulated minimum tracer mixing ratio versus CFL number under the tilted, periodic solid-body wind field using all Voronoi schemes on the refined mesh. The dotted black line is a reference for the initial minimum tracer mixing ratio.

Parameter	Value		
Initial Concentration	Cosine-bells, with $\phi \in [0.0, 1.0]$		
Wind Field	Solid-body	Tilted, periodic solid-body	NL2010
Courant Number	0.8		
Simulation Length	12 Days		
Number of Tracers	1		
Refinement	Coarse	Intermediate	Fine

Table 4.4: 2D entropy test cases

4.3.1 Entropy

As entropy is a measure of how much mixing occurs (Section 3.4.4), it can hence provide an indication of the degree of numerical diffusion occurring. The total entropy over the entire domain gives an indication of how much diffusion is occurring throughout this domain. Each cell containing some tracer contributes to the total entropy. Following a single tracer, a smooth initial distribution is taken, namely the cosine bell. The maximum value of the tracer mixing ratio at the peak of the bell is taken to be $\phi = 1.0$, while the background value surrounding the bells is taken to be 0. The choice of a zero background value is to avoid the accumulation of entropy from cells of the Voronoi mesh beyond the latitude boundaries of the Cartesian domain.

We plot the increase in total entropy between the initial time, and the total entropy at the current simulated time, following all schemes on both meshes, with the progression of time in days. These plots are repeated for all wind fields and at all used resolutions to show the effects of these two factors on diffusion, while comparing the performances of the schemes under each test case. These test cases are summarised in Table 4.4.

Fig. 4.3 presents the time variation of entropy on the coarsest mesh using different wind fields. On each panel we can compare numerical diffusion of the various schemes, especially how higher-order schemes compare to lower-order schemes, and how Voronoi-mesh schemes compare to similar Cartesian-mesh schemes. Starting with the solid-body wind field sub-figure in Fig. 4.3c as a reference graph, all schemes show an increase in entropy from the first simulated day. The highest increase is produced by the upwind scheme on the Voronoi mesh, followed by the upwind scheme on the Cartesian mesh, both of which are first-order schemes. A lower increase is produced by the Van Leer scheme, followed by the Gauss-Heun scheme, then the SLFV scheme, all three of which are second-order schemes. The PPM, which is built to be a higher order scheme, produces the least entropy. As time progresses, the hierarchy between schemes is maintained, with the exception of the Gauss-Heun scheme which exceeds the Van Leer scheme's entropy near the end of the simulation.

Quite unsurprisingly, by this measure, first order schemes result in the most numerical diffusion, followed by second-order schemes, then the third-order PPM scheme. This can be considered a baseline for the comparison of schemes following the other wind fields, and at higher resolution.

On meshes of intermediate (Fig. 4.4c) and fine (Fig. 4.5c) resolution, with the same solid-body wind field, entropy increases similarly with the values of entropy shifted to lower values. Thus numerical diffusion decreases for all schemes as the refinement increases, again an expected outcome.

We can repeat this analysis with the tilted periodic solid-body wind field. On the coarsest mesh (Fig. 4.3b), the

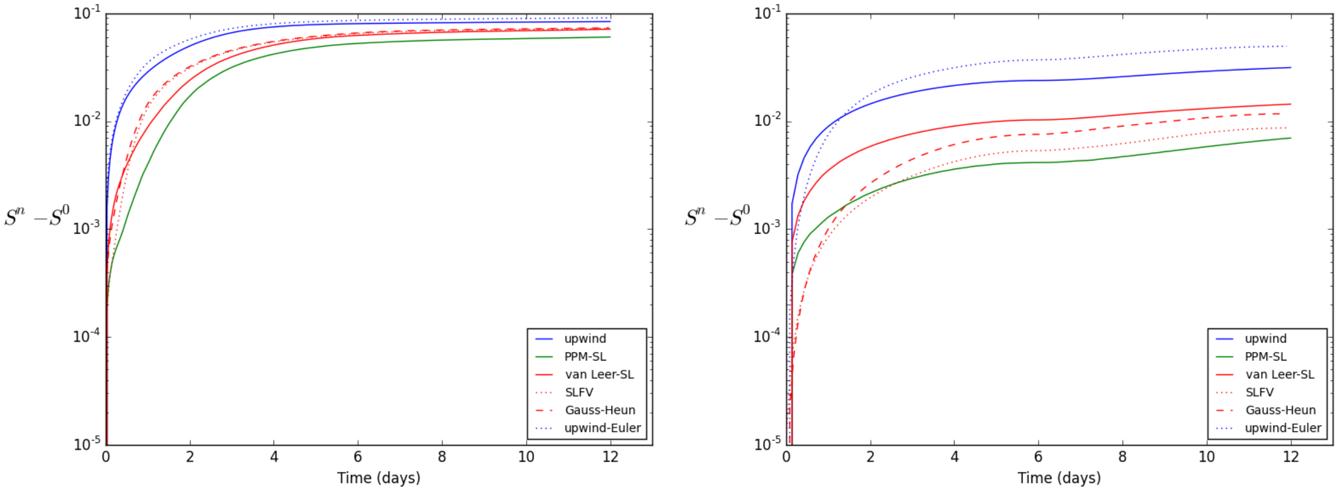

(a) NL2010

(b) Tilted, periodic solid-body

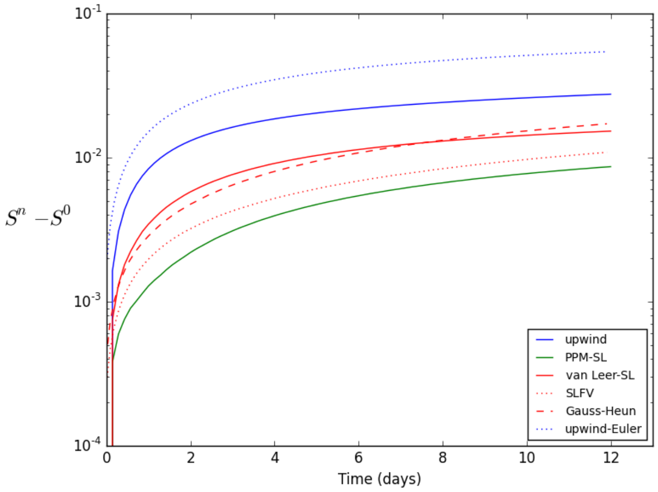

(c) Solid-body

Figure 4.3: Increase of entropy S from its initial value S^0 with time, in coarse-resolution simulations using various Voronoi-mesh and Cartesian-mesh schemes, with wind fields NL2010, tilted periodic solid-body rotation, and zonal solid-body rotation. Cartesian-mesh schemes are represented with solid lines, while the Voronoi-mesh schemes are represented with dotted lines. First order schemes are in blue, second order ones in red, and higher order in green.

Parameter	Value		
Initial Concentration	Cosine-bells, with $\phi \in [0.0, 1.0]$		
Wind Field	Solid-body	Tilted periodic solid-body	NL2010
Courant Number	0.8		
Simulation Length	12 Days		
Number of Tracers	2		
Refinement	Coarse	Intermediate	Fine

Table 4.5: 2D non-linear relationship preservation test case

schemes are ordered in the same hierarchy as with the solid-body wind field. However, slightly more entropy is produced than with the solid-body wind field. A similar behavior is observed with the NL2010 wind field. On the coarsest mesh (Fig. 4.3a), the schemes are ordered in the same hierarchy as with the solid-body wind field, and similarly exhibit a continuous increase in entropy as the simulation progresses. With finer meshes (Figs. 4.4a and 4.5a), the schemes produce again lower values of entropy.

It is worthy to note that significantly more entropy is produced with the NL2010 wind field than with the other two fields. This illustrates the fact that NL2010 presents strong stretching—unlike solid-body wind fields—and, as a result, is more demanding for numerical schemes.

With the potential replacement of the Cartesian mesh by a Voronoi mesh in the CHIMERE model in mind, it is important to compare the numerical diffusion exhibited by the second-order Voronoi-mesh schemes to the second-order Cartesian-mesh scheme, here "Van Leer-SL", where the "SL" refers to the slope-limiting added to the Van Leer scheme. It is seen that all three schemes produce a similar amount of entropy. With solid-body wind fields, the SLFV scheme produces less entropy than Gauss-Heun and Van Leer-SL, but this advantage disappears with the NL2010 wind field, where the differences between second-order schemes are much smaller than the gap between schemes of different orders.

From this measure of diffusivity—and based on this limited set of synthetic numerical experiments—it seems, therefore, that replacing the Cartesian Van Leer-SL scheme by a second-order Voronoi-mesh scheme would not, at comparable resolutions, introduce significant additional numerical diffusion.

4.3.2 Preservation of non-linear relationships between tracers

The test cases of Table 4.5 summarize the conditions we use to study our second metric of numerical diffusion: the preservation of non-linear tracer relationships. In all cases, 2 tracers must be present throughout the simulation, with a relationship of dependence quantifying their mixing ratios relative to each other. We use the relationship described in Section 3.4.4. We set the first tracer's initial mixing ratio distribution to the cosine-bell distribution, so that both tracers start with a smooth field. We use mixing ratio values between 0 and 1 for the first tracer, so that the second tracer has values between 0.1 and 0.9 following the non-linear relationship of Eq. 3.31.

The test cases include all wind fields and all mesh resolutions. The use of different wind fields permits to show the effects of these on diffusivity, where more deformational fields are expected to result in greater diffusion. Furthermore, higher numerical diffusion is expected with coarser meshes.

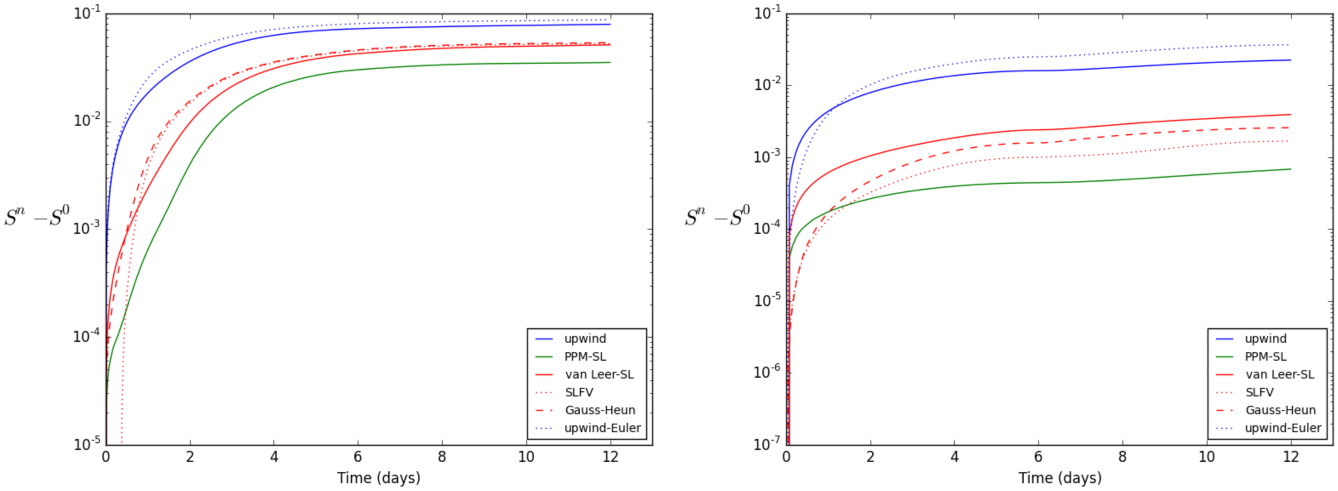

(a) NL2010

(b) Tilted, periodic solid-body

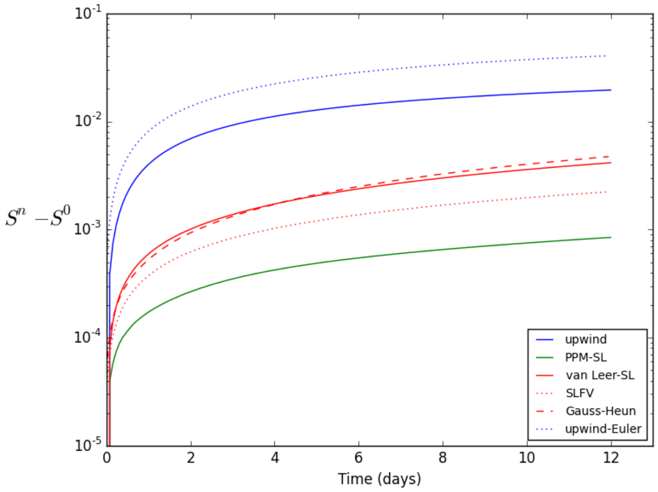

(c) Solid-body

Figure 4.4: Increase of entropy S from its initial value S^0 with time, in intermediate-resolution simulations using various Voronoi-mesh and Cartesian-mesh schemes, with wind fields NL2010, tilted periodic solid-body rotation, and zonal solod-body rotation. Cartesian-mesh schemes are represented with solid lines, while the Voronoi-mesh schemes are represented with dotted lines. First order schemes are in blue, second order ones in red, and higher order in green.

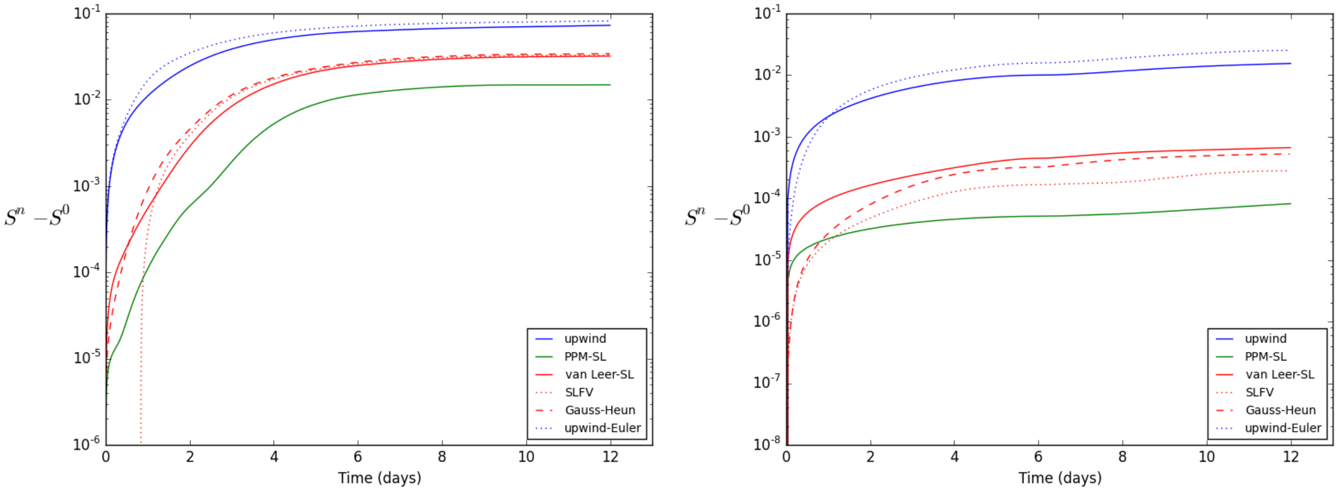

(a) NL2010

(b) Tilted, periodic solid-body

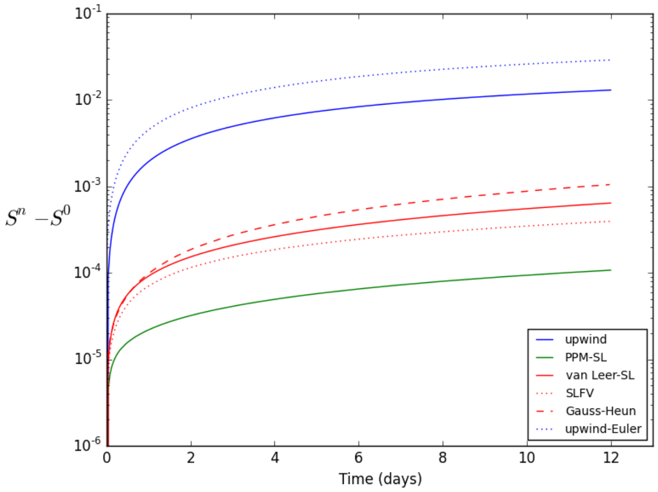

(c) Solid-body

Figure 4.5: Increase of entropy S from its initial value S^0 with time, in fine-resolution simulations using various Voronoi-mesh and Cartesian-mesh schemes, with wind fields NL2010, tilted periodic solid-body rotation, and zonal solod-body rotation. Cartesian-mesh schemes are represented with solid lines, while the Voronoi-mesh schemes are represented with dotted lines. First order schemes are in blue, second order ones in red, and higher order in green.

To visualize the preservation of the used non-linear relationship (Eq. 3.31) by the used schemes—where non-preservation indicates diffusivity—a mixing plot (see Fig. 3.7 as a reference) is made for each scheme, following each wind field, and at every mesh resolution. The analysis is based on scatter plots of the second mixing ratio, phi_2, as a function of the first mixing ratio, ϕ_1. The figures are organized such that sub-figures represent increasing mesh resolution from left to right, and increasing scheme order from top to bottom. The Cartesian schemes are together in one plot for each wind field, and the Voronoi schemes are similarly organized. As for the plotted values, any decrease from the initial maximum value of the tracer mixing ratio indicates the occurrence of diffusion. Moreover, diffusion is represented by any point on the plots below the curve representing the non-linear tracer relationship. This also indicates a decrease from theoretical tracer mixing ratio values.

It is important to note that the schemes are monotonic with the use of slope-limiting (Section 2.4) and with an appropriate Courant number. Therefore, they are expected to exhibit no over- nor under-shooting beyond the initial range of values. On the other hand, real mixing is expected and range-preserving un-mixing remains possible.

Solid-body wind field

This wind field is again used as a baseline for the analysis. We start with results from the Cartesian schemes, in order to build familiarity with the analysis of these scatter plots. We reiterate that the solid-body velocity field taken in this study is parallel to the latitude bands, and is hence perfectly aligned with the Cartesian mesh cells, potentially endowing the Cartesian schemes with an advantage. This fact is considered when analyzing the results.

Fig. 4.6 presents scatter plots of the second mixing ratio, phi_2, as a function of the first mixing ratio, ϕ_1. If the initial relationship between phi_1 and ϕ_2 were exactly preserved, all red points would fall on the reference curve. On panel (i), the PPM scheme with $N = 28800$ grid points is close to this ideal behavior. For the Cartesian schemes under the solid-body wind field, at the coarsest mesh refinement (left column), the upwind, Van Leer and PPM schemes all result in points within the convex hull of the reference curves. The points (ϕ_1, ϕ_2) corresponding to the upwind scheme are clustered in the region $0 \leq \phi_1 \leq 0.5$, $0.6 \leq \phi_2 \leq 0.9$. With the Van Leer scheme, the values are less clustered with $0 \leq \phi_1 \leq 0.7$, $0.5 \leq \phi_2 \leq 0.9$. Finally, for the PPM scheme, the points span $0 \leq \phi_1 \leq 0.8$, $0.3 \leq \phi_2 \leq 0.9$. Thus, higher-order schemes are able to retain values of the tracer mixing ratios closer to their initial ranges. This is consistent with higher-order schemes being less diffusive than lower-order schemes.

At intermediate mesh refinement (the central column), the values mainly remain in the convex hull. Clustering is again highest for the upwind scheme, less for the Van Leer scheme and least for PPM. Compared to the coarsest resolution, red points are distributed closer to the reference curve. With the PPM scheme, for $\phi_1 \simeq 0.2$, some points fall just above the reference curve. These points are not in the convex hull, and are indicators of some range-preserving numerical un-mixing.

At the finest refinement (the right column), all points fall close to the reference curve, especially for PPM, and less so for upwind. They also span a wider range of values, as expected from the reduction in numerical diffusion as resolution is increased. Some range-preserving un-mixing is visible for the Van Leer scheme near $\phi_1 = 0.2$.

We continue with Voronoi schemes (Figure 4.7). At the coarsest mesh refinement (the left column), the upwind (panel a), and Gauss-Heun (panel d) schemes result in points all within the convex hull of the reference curves, thus corresponding to real mixing. On the other hand, the SLFV scheme (panel g) presents some un-mixing near $\phi_1 = 0.8$. Clustering is very strong for upwind, less strong for Gauss-Heun, and slightly less strong for SLFV. Thus, the higher-

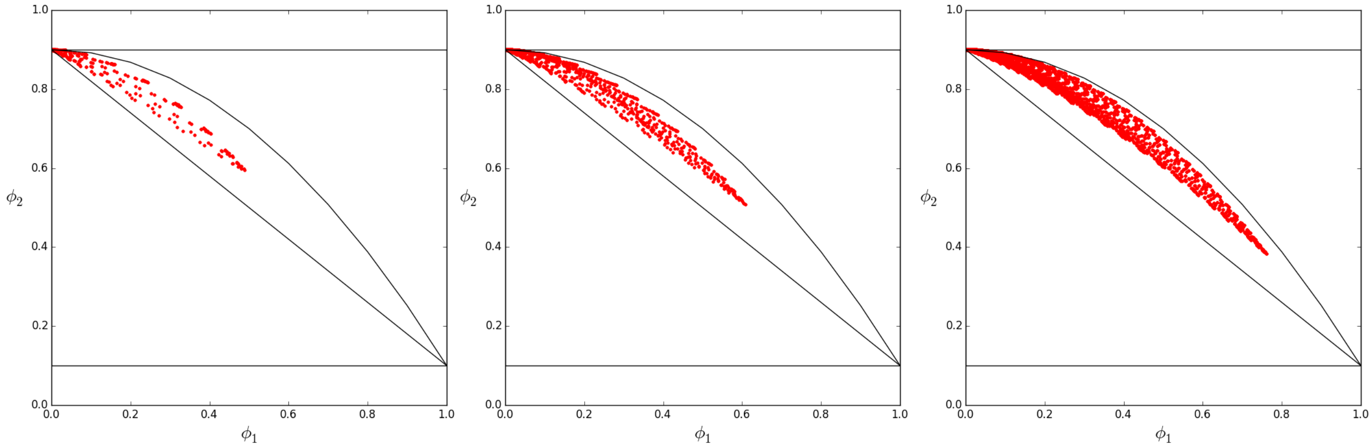

(a) Cartesian upwind, $N = 1800$ (b) Cartesian upwind, $N = 7200$ (c) Cartesian upwind, $N = 28800$

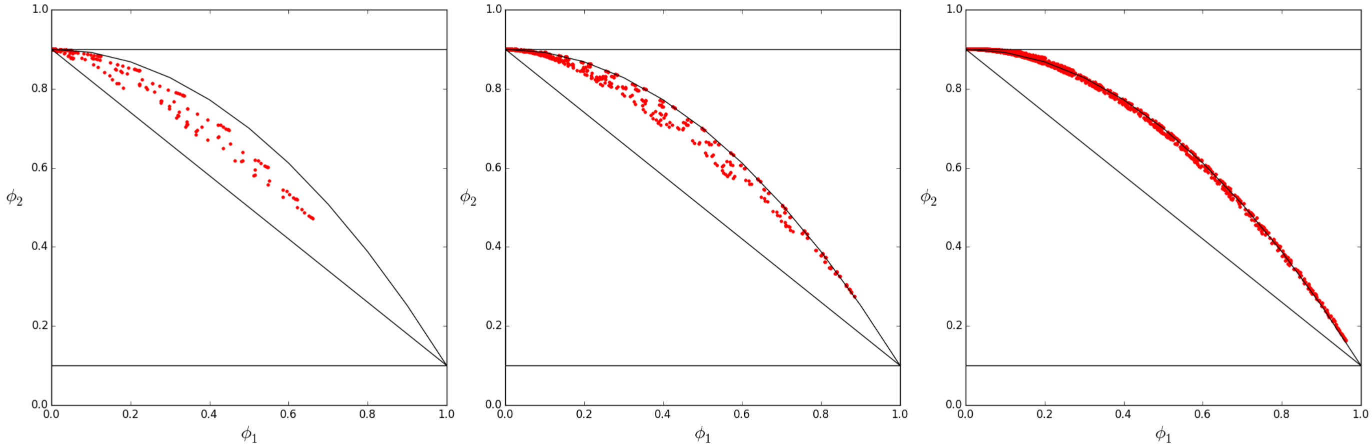

(d) Cartesian van Leer, $N = 1800$ (e) Cartesian van Leer, $N = 7200$ (f) Cartesian van Leer, $N = 28800$

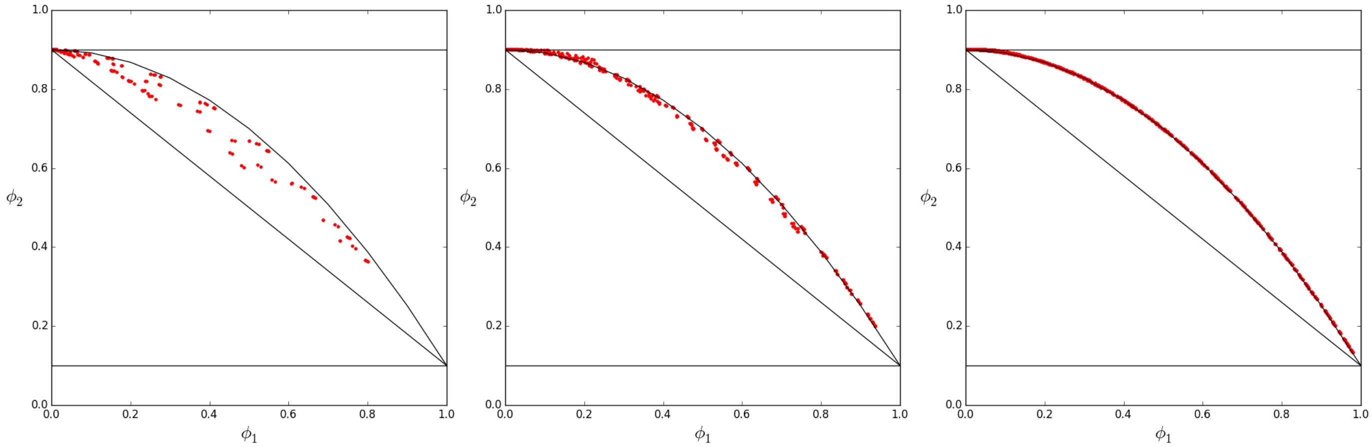

(g) Cartesian PPM, $N = 1800$ (h) Cartesian PPM, $N = 7200$ (i) Cartesian PPM, $N = 28800$

Figure 4.6: The mixing ratio of the second tracer, ϕ_2, versus that of the first tracer, ϕ_1, between reference lines (in black) following Cartesian mesh simulations of the solid-body wind field using three schemes and three resolutions

order schemes are indeed less diffusive than the upwind scheme, at the price of some un-mixing for SLFV.

At intermediate mesh resolution (the center column), the values remain in the convex hull only with the upwind scheme (panel b). With the Gauss-Heun (panel e) and SLFV (panel h) schemes, points get closer to the reference curve, but SLFV exhibits noticeable un-mixing although less than the strong un-mixing produced by Gauss-Heun. Compared to Cartesian schemes, SLFV produces a scatter plot that is intermediate between PPM (Fig. 4.6, panel h) and Van Leer (Fig. 4.6, panel e).

At the finest resolution (the right column), the previous trend is enhanced. Upwind produces only points in the convex hull (panel c), but at the price of strong diffusion. Indeed the range covered by (ϕ_1, ϕ_2) is comparable to the range obtained by Gauss-Heun and SLFV at the coarsest resolution (panels d and g). SLFV (panel i) produces points very close to the reference curve, covering it almost entirely, except near its lower-right extremity, with perhaps some un-mixing. Gauss-Heun, on the other hand, produces a large amount of un-mixing, perhaps as large as at the intermediate resolution. Thus, while both SLFV and Gauss-Heun are less diffusive than upwind, the reduced diffusion of Gauss-Heun comes at a high price in terms of un-mixing. Compared to Cartesian schemes, SLFV produces, again, a scatter plot that is intermediate between PPM (Fig. 4.6, panel i) and Van Leer (Fig. 4.6, panel f).

To summarize these observations, we begin by noting that, as expected, schemes of higher order show less numerical diffusion than those of lower order, and increased mesh refinement implies a decrease of numerical diffusion. However, while the PPM scheme produces a small amount of range-preserving un-mixing, this numerical artifact is stronger on the Voronoi side, and especially strong with the Gauss-Heun scheme. At intermediate and fine resolutions, the schemes best preserving the non-linear relationship are, in order, PPM, SLFV and Van Leer, while the strong amount of un-mixing presented by Gauss-Heun seems problematic.

At this point, we bring forth the note that the solid-body wind field is biased to the Cartesian schemes with regards to cell orientation. We can hypothesize that the stronger un-mixing found on the Voronoi side may be a consequence of this bias. To shed some light on this issue, we repeat the analysis with the tilted periodic solid-body wind field.

Tilted periodic solid-body wind field

Fig. 4.8 presents scatter plots of ϕ_2 vs ϕ_1 for the Cartesian schemes under the tilted periodic solid-body wind field. It is very similar to Fig. 4.6, so we comment on it only very briefly. Our main interest is in the effect of the solid-body rotation being oblique now, rather than zonal previously, especially in the production of un-mixing. We see that, although the wind field is not aligned with the Cartesian mesh anymore, the preservation of the non-linear relationship between ϕ_1 and ϕ_2 is not significantly degraded. Specifically, it is not possible to detect un-mixing produced by the Van Leer scheme (panels d, e, and f). At intermediate resolution, un-mixing due to PPM (panel h) is comparable to the one found with the zonal solid-body wind field (Fig. 4.6, panel h).

Figure 4.9 presents scatter plots of ϕ_2 vs ϕ_1 for the Voronoi schemes under the tilted periodic solid-body wind field. It can be compared to Fig. 4.7. The most striking difference is for the Gauss-Heun scheme (panels d, e, and f) especially at intermediate and fine resolutions (panels e and f). While un-mixing (red points outside the convex hull of the reference curve) is still significant especially near $\phi_1 = 0.2$, it is much reduced compared to Fig. 4.7 (panels e and f). This reduction in the amount of un-mixing is also present—although less striking—for the SLFV scheme (panels h and i on both figures). Since the Voronoi mesh does not have preferred directions, this improvement is probably not due to a more favourable orientation of the wind field. However, the time periodicity of the wind field may result in a cancellation

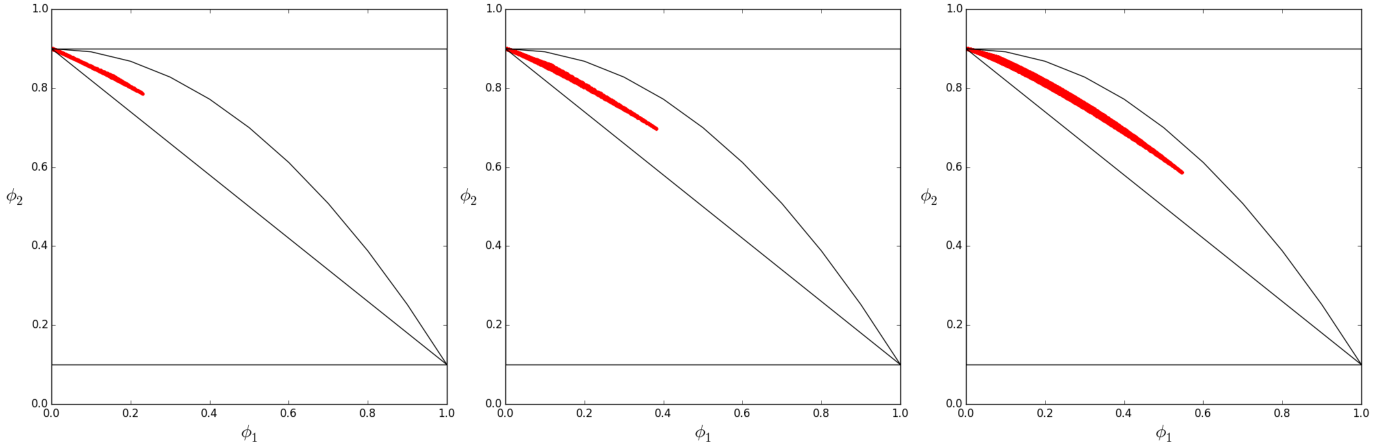

(a) Voronoi upwind, $N = 1812$ (b) Voronoi upwind, $N = 7242$ (c) Voronoi upwind, $N = 28965$

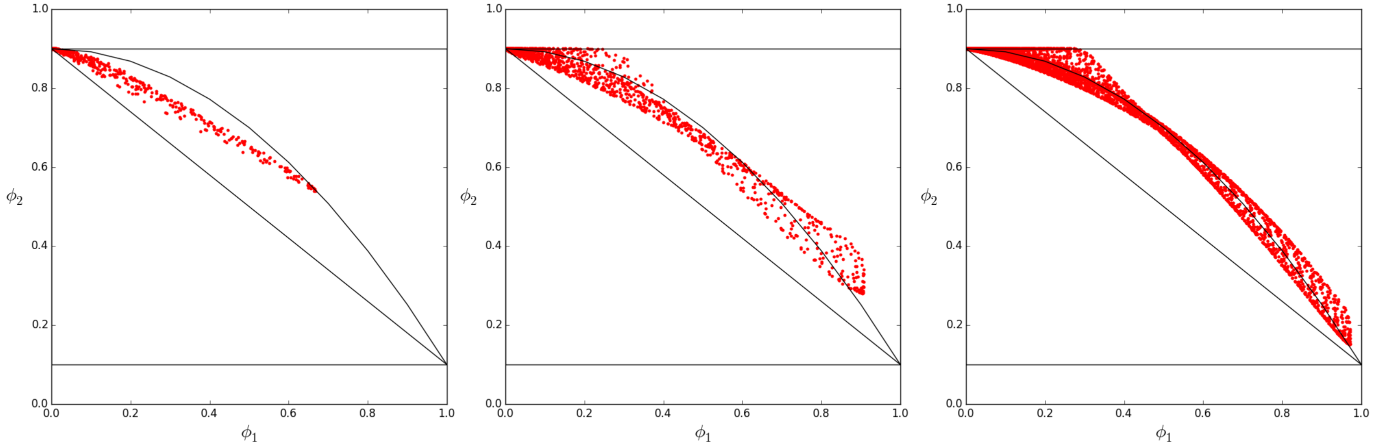

(d) Voronoi Gauss-Heun, $N = 1812$ (e) Voronoi Gauss-Heun, $N = 7242$ (f) Voronoi Gauss-Heun, $N = 28965$

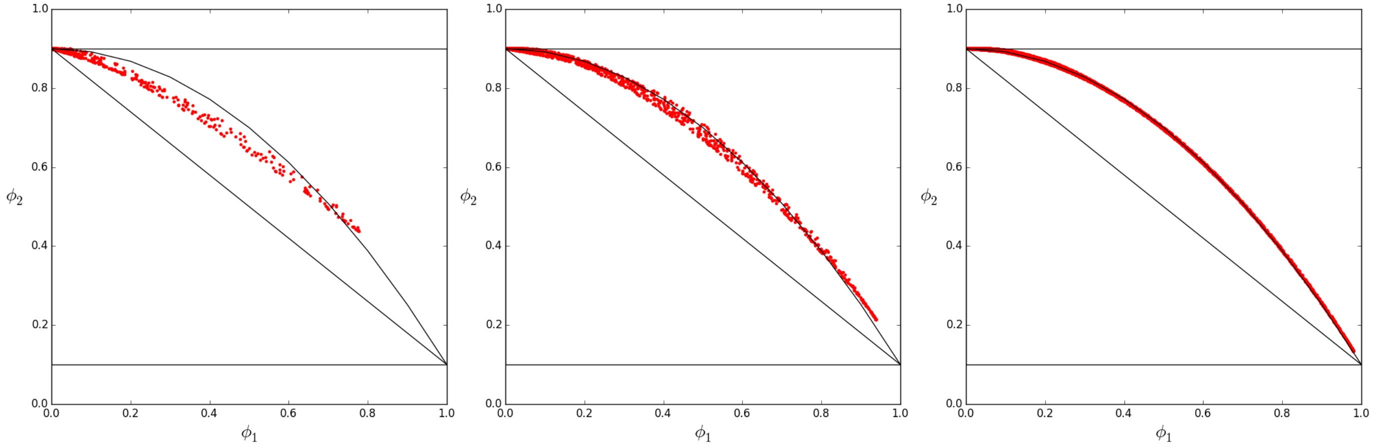

(g) Voronoi SLFV, $N = 1812$ (h) Voronoi SLFV, $N = 7242$ (i) Voronoi SLFV, $N = 28965$

Figure 4.7: The mixing ratio of the second tracer, ϕ_2, versus that of the first tracer, ϕ_1, between reference lines (in black) following Voronoi mesh simulations of the solid-body wind field using all schemes and resolutions

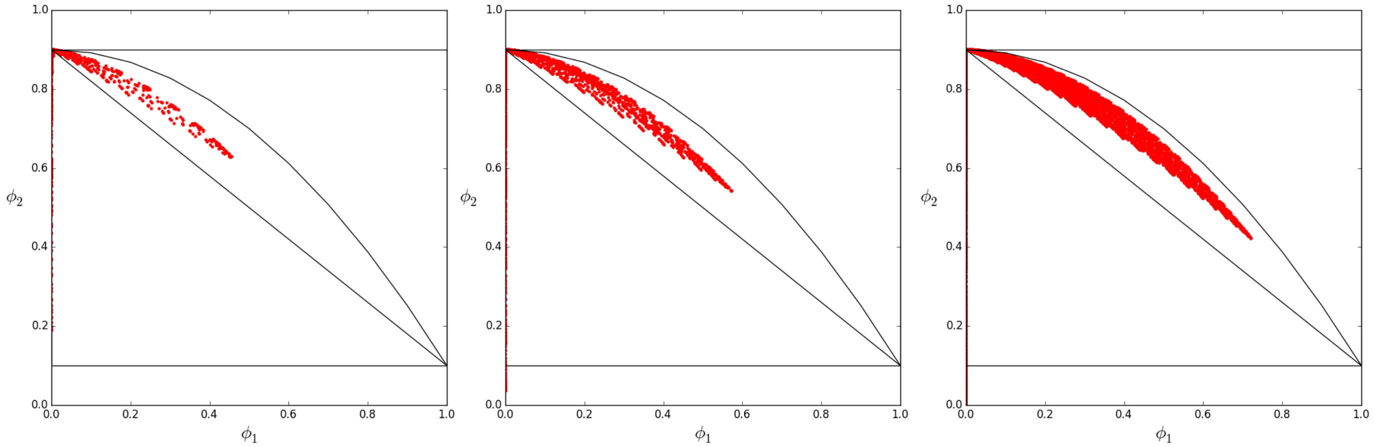

(a) Cartesian upwind, $N = 1800$ (b) Cartesian upwind, $N = 7200$ (c) Cartesian upwind, $N = 28800$

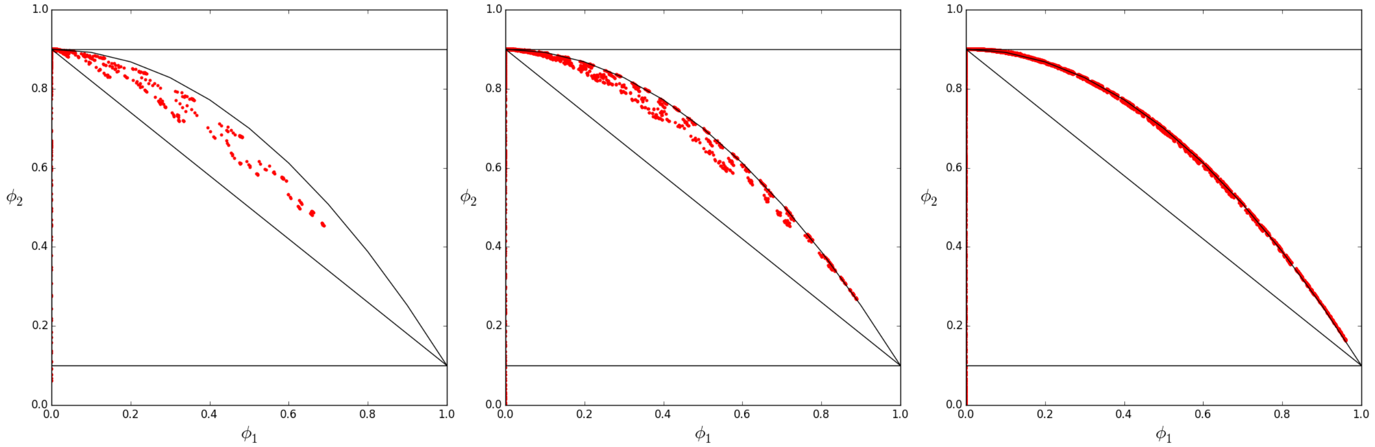

(d) Cartesian van Leer, $N = 1800$ (e) Cartesian van Leer, $N = 7200$ (f) Cartesian van Leer, $N = 28800$

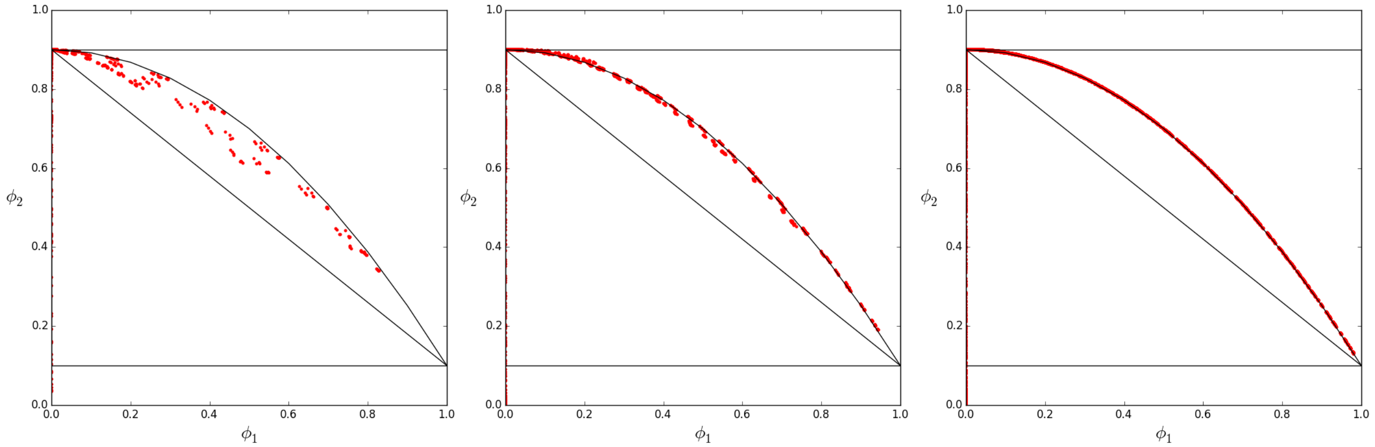

(g) Cartesian PPM, $N = 1800$ (h) Cartesian PPM, $N = 7200$ (i) Cartesian PPM, $N = 28800$

Figure 4.8: The mixing ratio of the second tracer, ϕ_2, versus that of the first tracer, ϕ_1, between reference lines (in black) following Cartesian mesh simulations of the tilted, periodic solid-body wind field using all schemes and resolutions

of errors. Such cancellation does not occur with the steady zonal solid-body velocity. Overall, it is safer to regard this reduction of un-mixing as very specific to this particular wind field.

NL2010 wind field

We continue the analysis with the NL2010 wind field featuring a zonal solid-body wind and a pair of vortices. Unlike the previous two wind fields, this wind field induces strong shear. This shear leads to the formation of filaments and fronts which are harder to resolve than the initial tracer field.

Fig. 4.10 presents scatter plots of the second mixing ratio, ϕ_2, as a function of the first mixing ratio, ϕ_1. This figure can be compared to Figs. 4.6 and 4.8. At coarse resolution (the left column), all schemes produce drastic clustering of the points near the top-left corner. This illustrates the enhancement of numerical diffusion due to the poorly-resolved tracer fronts and filaments. The hierarchy between the schemes is the same as before: i.e. the upwind scheme (panel a) performs worst, followed by Van Leer (panel d) then by PPM (panel g). At intermediate resolution (the center column), clustering is somewhat reduced but is still very strong. With the Van Leer (panel e) and PPM (panel h) schemes, some points lie close to the reference curve, but the overwhelming majority of points lie well inside the convex hull, indicating strong numerical mixing. At higher resolution (the right column), the nonlinear relationship starts to become somewhat better preserved, with more points close to the reference curve for the Van Leer (panel f) and PPM (panel i) schemes. Numerical mixing is still quite strong, indeed stronger than with solid-body and tilted periodic solid-body wind fields at coarse resolution (Figs. 4.6 and 4.8, left column). The same hierarchy between schemes is observed.

Finally, Fig. 4.11 presents scatter plots for the Voronoi schemes. At coarse resolution (the left column), numerical diffusion is very high. The upwind scheme (panel a) behaves similarly to the Cartesian upwind scheme (Fig. 4.6, panel a) while Gauss-Heun (panel d) and SLFV (panel g) schemes behave similarly to the Cartesian Van Leer scheme (Fig. 4.10, panel d). Numerical mixing is somewhat reduced at intermediate resolution (the center column). The upwind scheme (panel b) behaves similarly to the Cartesian upwind scheme (Fig. 4.6, panel b) while Gauss-Heun (panel e) and SLFV (panel h) schemes behave roughly like the Cartesian Van Leer scheme (Fig. 4.10, panel e). The latter is nevertheless better at preserving the non-linear relationship, with at least some points close to the reference curve, while almost all points are well within the convex hull for Voronoi schemes. The amount of mixing decreases at higher resolution. Although Gauss-Heun (panel f) and SLFV (panel i) perform better than upwind (panel c), both are very similar in their poor preservation of the nonlinear relationship. Compared to experiments with solid-body and tilted periodic solid-body wind fields, the amount of mixing is similar to the one produced by the upwind scheme at coarse resolution (Figs. 4.7 and 4.9, panel a).

To summarize the insight gained in this section, some outcomes are a mere confirmation of expectations: numerical diffusion is reduced at higher resolution and with higher-order schemes, which are also better at preserving an existing non-linear relationship between tracers. In addition to this unsurprising outcome, we gained some insight especially onto the second-order schemes. The hierarchy between the studied schemes in terms of entropy production is that the Cartesian PPM scheme performs best, followed by the Voronoi scheme SLFV. They are followed by Gauss-Heun (Voronoi) and Van Leer (Cartesian), which are on par. Upwind is, of course, very diffusive on both meshes. In terms of preservation of non-linear relationships, PPM comes first again. With the solid-body wind field, SLFV comes next, followed by the Cartesian van Leer scheme. The Gauss-Heun schemes produces a large amount of un-physical mixing. This phenomenon is not observed with the tilted periodic solid-body wind field, but this could be the result of a lucky

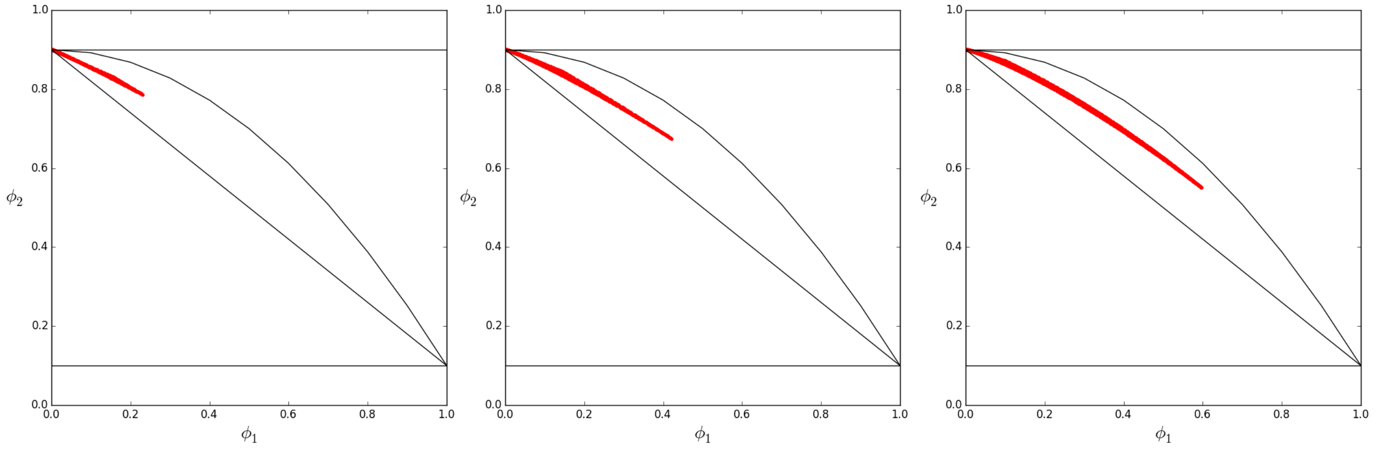

(a) Voronoi upwind, $N = 1812$ (b) Voronoi upwind, $N = 7242$ (c) Voronoi upwind, $N = 28965$

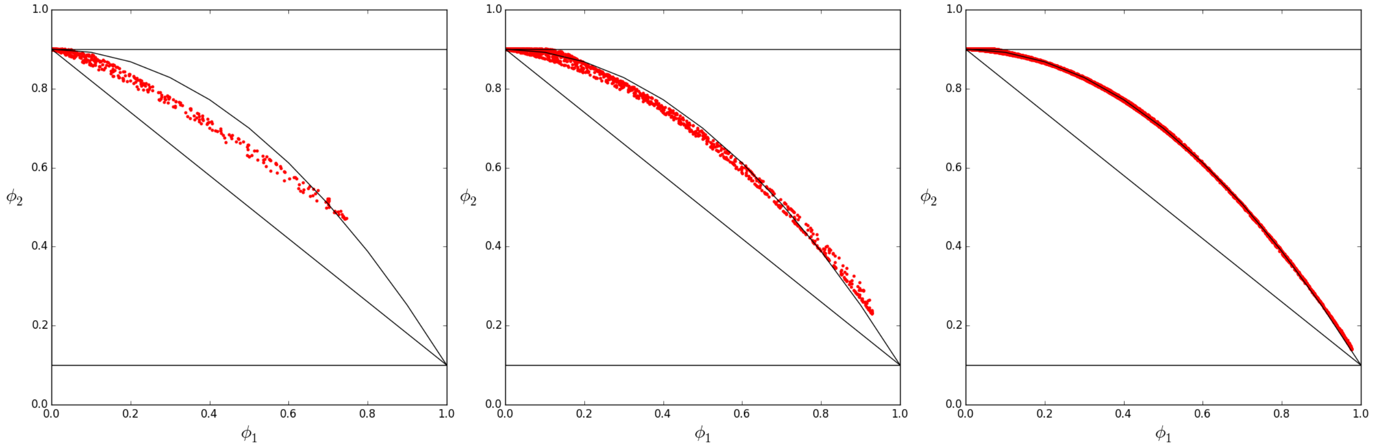

(d) Voronoi Gauss-Heun, $N = 1812$ (e) Voronoi Gauss-Heun, $N = 7242$ (f) Voronoi Gauss-Heun, $N = 28965$

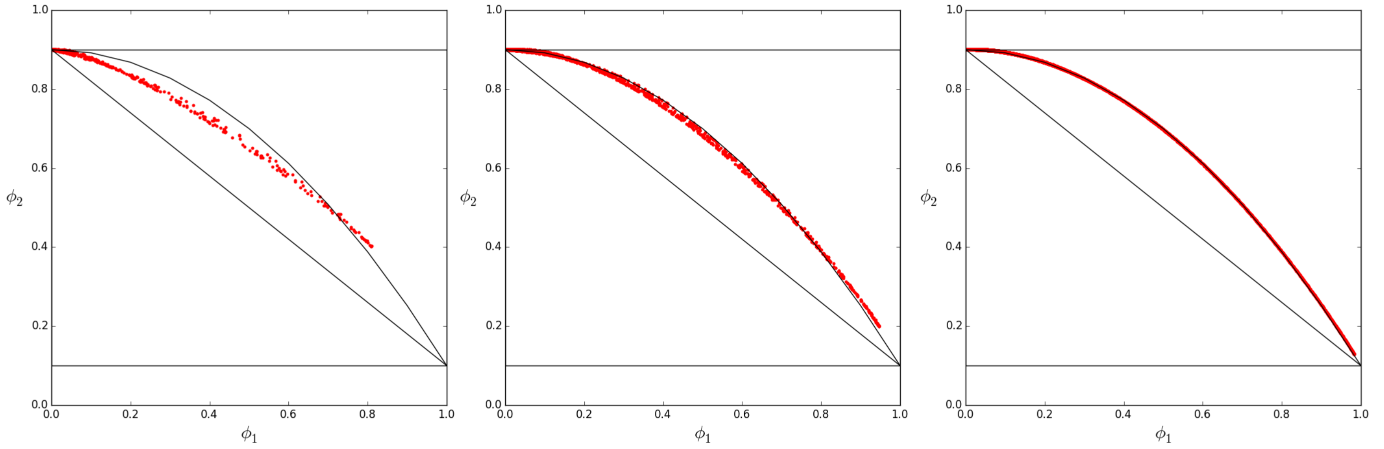

(g) Voronoi SLFV, $N = 1812$ (h) Voronoi SLFV, $N = 7242$ (i) Voronoi SLFV, $N = 28965$

Figure 4.9: The mixing ratio of the second tracer, ϕ_2, versus that of the first tracer, ϕ_1, between reference lines (in black) following Voronoi mesh simulations of the tilted, periodic solid-body wind field using all schemes and resolutions

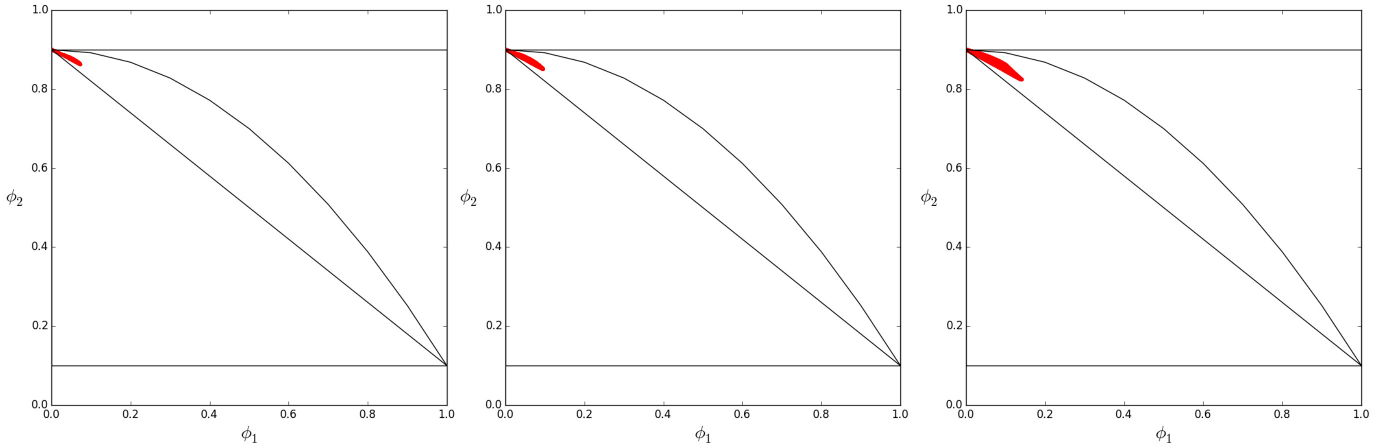

(a) Cartesian upwind, $N = 1800$ (b) Cartesian upwind, $N = 7200$ (c) Cartesian upwind, $N = 28800$

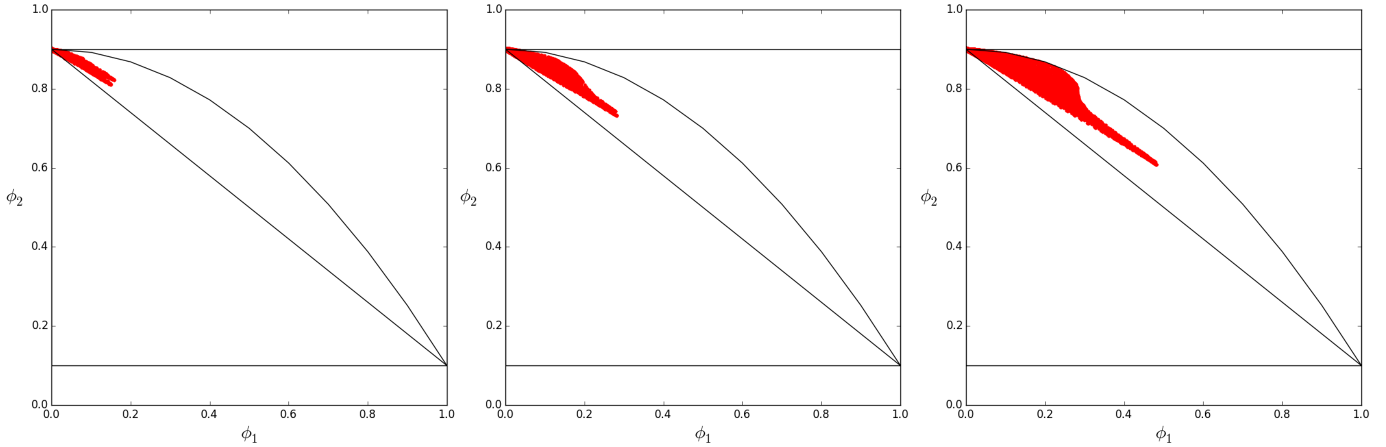

(d) Cartesian van Leer, $N = 1800$ (e) Cartesian van Leer, $N = 7200$ (f) Cartesian van Leer, $N = 28800$

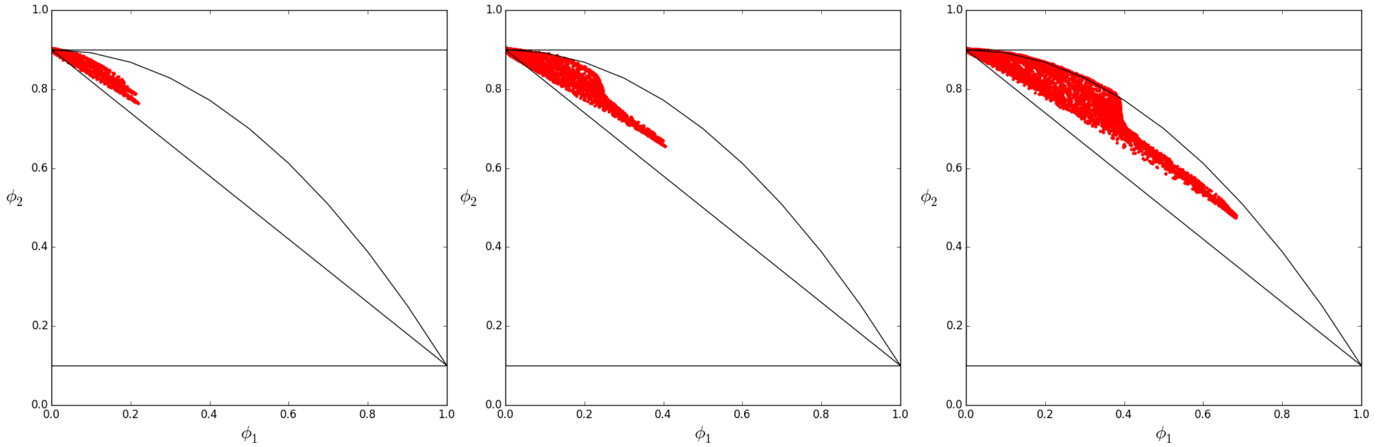

(g) Cartesian PPM, $N = 1800$ (h) Cartesian PPM, $N = 7200$ (i) Cartesian PPM, $N = 28800$

Figure 4.10: The mixing ratio of the second tracer, ϕ_2, versus that of the first tracer, ϕ_1, between reference lines (in black) following Cartesian mesh simulations of the NL2010 wind field using all schemes and resolutions

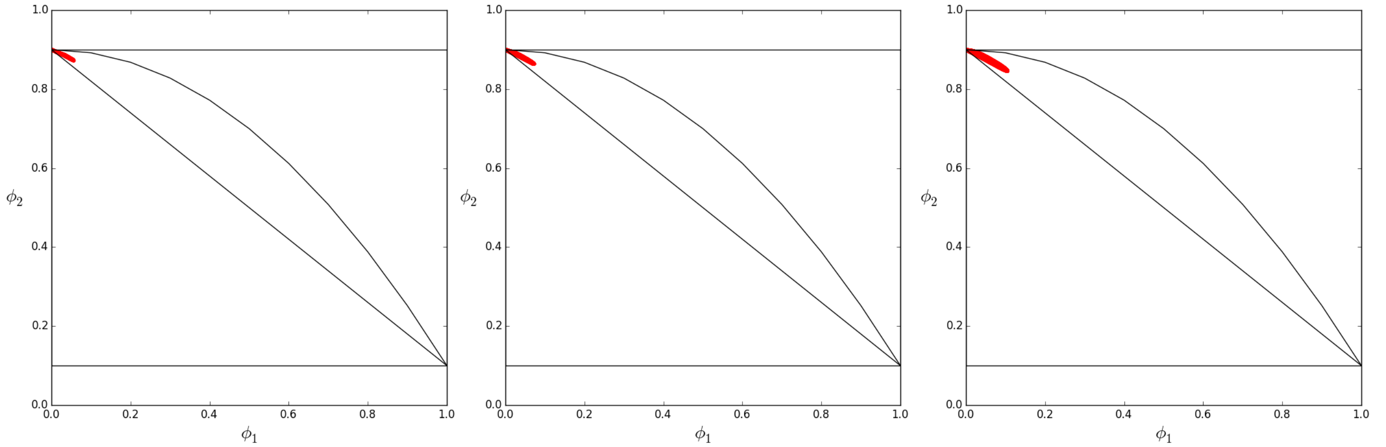

(a) Voronoi upwind, $N = 1812$ (b) Voronoi upwind, $N = 7242$ (c) Voronoi upwind, $N = 28965$

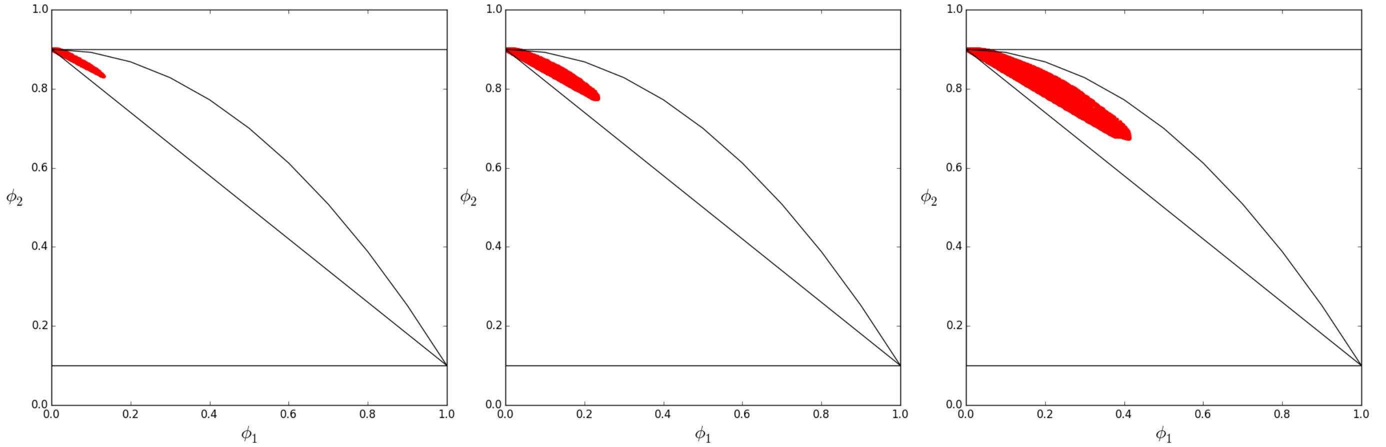

(d) Voronoi Gauss-Heun, $N = 1812$ (e) Voronoi Gauss-Heun, $N = 7242$ (f) Voronoi Gauss-Heun, $N = 28965$

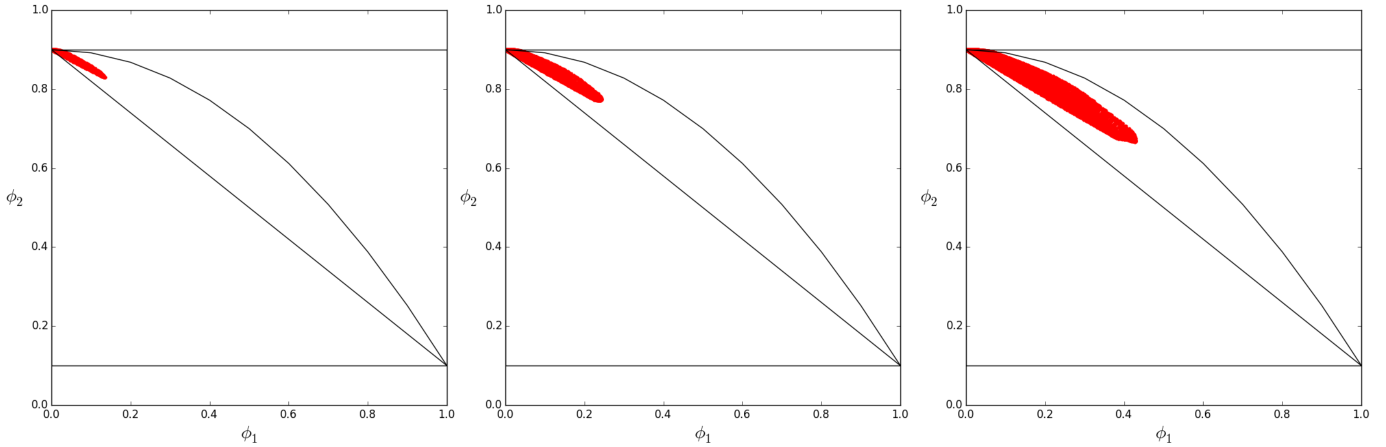

(g) Voronoi SLFV, $N = 1812$ (h) Voronoi SLFV, $N = 7242$ (i) Voronoi SLFV, $N = 28965$

Figure 4.11: The mixing ratio of the second tracer, ϕ_2, versus that of the first tracer, ϕ_1, between reference lines (in black) following Voronoi mesh simulations of the NL2010 wind field using all schemes and resolutions

cancellation of errors. The NL2010 is much more challenging in terms of preservation of non-linear relationships. Only PPM does a decent job at the highest resolution studied. Gauss-Heun and SLFV produce strong diffusion and poor preservation of the nonlinear relationship. The Cartesian Van Leer scheme performs better, but only slightly.

4.4 Convergence

After comparing diffusion between the different numerical configurations under study, it is important to test their convergence-rate order. From the theoretical properties of the schemes, we expect first-order convergence for the Godunov upwind-type first-order schemes, in which upwind concentration is considered equal to the average concentration of the upwind cell (on both Cartesian and Voronoi grids), and second-order for all other schemes. While it is third-order by design, the Colella and Woodward [1984] PPM scheme formally yields second-order convergence only because of slope-limiting in the vicinity of concentration extrema [Colella and Sekora, 2008]. Calculating accuracy for all the numerical configurations under consideration will permit not only to check that all these configurations offer the expected convergence order in accuracy, but also to check how they compare wth each other in terms of accuracy and convergence rate.

Here, and in the following, we define the error as the root-mean-square error (RMSE) between the simulated field and the exact solution. For all cases, the initial concentration is a cosine bell centered at $\left(\lambda = \frac{5\pi}{6}, \phi = 0\right)$. This fields offers the sufficient smoothness (it is twice differentiable) to ensure convergence up to second order for the schemes with that expectation.

In the rest of this chapter, we will plot the RMSEs of the Voronoi schemes together with those of the Cartesian schemes on the same plots, and for exactly identical numerical experiments to permit a just comparison of their accuracy. The Voronoi schemes are represented with hexagonal markers—analogous to their mesh-cell shapes—while the Cartesian schemes are represented with square markers. First- and second-order reference lines are added to the plots to visualize the convergence order. An increase in mesh resolution is quantified by an increase in the number of mesh cells. While, in theory, the convergence order does not depend on the wind or concentration field—provided that the wind field is smooth enough—this is true only in an asymptotic way. As we will see later, for deformational wind fiels, some numerical configurations may not display the expected convergence order for the resolution within our computational reach. Therefore, it is useful to produce and analyze convergence plots for several wind fields, more or less *difficult* and deformational, in order to assess the accuracy of the various configurations in different contexts. The text cases that have been used for this purpose are summarised in Table 4.6.

4.4.1 Zonal solid-body-rotation convergence

The classical solid-body wind field suits as a baseline for scheme RMSE comparisons. The non-deformational nature of this wind field makes it rather *un-challenging* for numerical schemes, even though the long trajectory imposed on the fluid—one entire rotation around the equator—will, as shown below, pose a challenge to first-order schemes.

For this test case, Fig. 4.12 shows the evolution of the total RMSE versus mesh resolution. As expected, first-order schemes (in blue) yield a larger error than higher-order schemes. All second-order schemes offer a convergence rate aligned with their theoretical order, with the notable exception of the Gass-Heun scheme on the Voronoi grid. Since this scheme is based exactly on the same discretization strategy and gradient calculation as the SLFV scheme, its relatively poor performance relative to the SLFV scheme suggests that the semi-Lagrangian approach of SLFV offers improved

Parameter	Value		
Initial Concentration	Single cosine-bell, with $\phi \in [0.0, 1.0]$		
Wind Field	Solid-body	Tilted, periodic solid-body	NL2010
Courant Number	0.8		
Simulation Length	12 Days		
Number of Tracers	1		
Refinement	Coarse	Intermediate	Fine

Table 4.6: Summary of the test-cases used to test accuracy and convergence rate of the numerical configurations under consideration

performance relative to a purely Eulerian approach. Notably enough, for this test case, the SLFV scheme on a Voronoi grid performs best among all schemes. This is not at all expected as the PPM scheme—with its third-order design—is anticipated to perform better, particularly in a case for which the purely zonal wind field is exactly aligned with the cell boundaries of the Cartesian lat-lon grid.

Surprisingly, first-order schemes do not display the expected first-order convergence rate for this simple test case, which is very likely due to the long trajectory of the fluid. Further increase in resolution would be needed to obtain first-order convergence for this test-case, which emphasizes the limited performance of such schemes and the need to use higher-order ones.

4.4.2 Tilted periodic solid-body convergence

In order to neutralize the possible advantage endowed by the zonal solid-body wind field upon the Cartesian schemes, we perform the same numerical experiment using the tilted solid-body-type periodically oscillating wind field to test this metric. Though this wind field is also a non-deformational solid-body rotation, its slightly tilted rotation axis induces non-zero meridional wind. A relatively small tilt angle, 0.05rad, is used to avoid the departure of the advected mass through the Cartesian latitude band limits of $[\frac{-\pi}{4}, \frac{\pi}{4}]$ during 12 days of advection. A reversing wind direction with a sinusoidal formulation is used in order to check the correct behaviour of the Strang-splitting configuration for the second-order Cartesian schemes.

Fig. 4.13 shows the evolution of the total RMSE of all used schemes versus the mesh resolution for this test case. This figure shows that, as with the previous case, the Godunov upwind schemes on both grids have the largest RMSE and fail to converge at a first-order rate. All second-order schemes converge according to their theoretical slope, including the Gauss-Heun which failed to do so in the zonal solid-body rotation test case. This is possibly due to the shorter trajectory of fluid parcels in the present test case compared to one complete solid-body rotation of $2\pi\,\mathrm{rad}$. In the present test case, the Gauss-Heun scheme's RMSE even matches that of the PPM scheme on the Cartesian grid. In this non-deformational test case, the SLFV scheme on the Voronoi grid clearly outperforms itself under all other tested cases, with a convergence order larger than 2. Such an accuracy exceeds those of all the schemes we use for this test case.

All in all, once the comparative advantage to lat-lon grid schemes with purely zonal flow is removed by slightly tilting the solid-body rotation axis, the schemes operating on the Voronoi grid perform substantially better than comparable

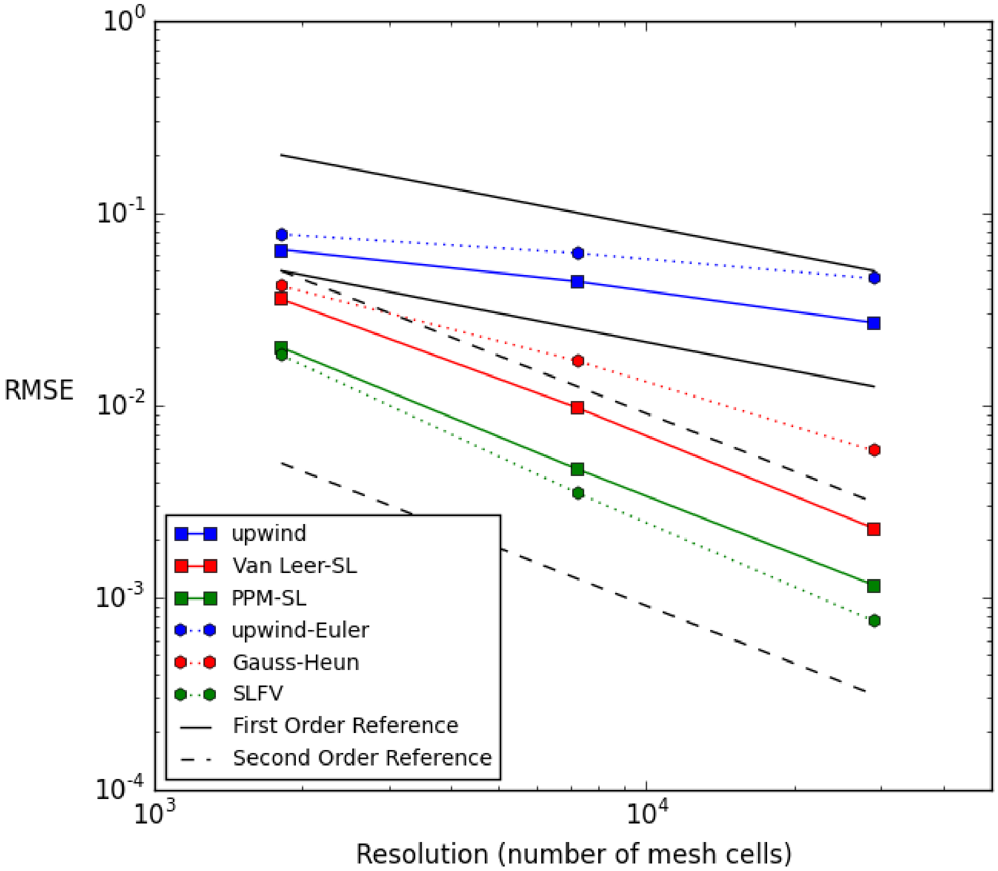

Figure 4.12: Root-mean-square error as a function of grid refinement for 2D Voronoi and Cartesian schemes under the classical solid-body wind field

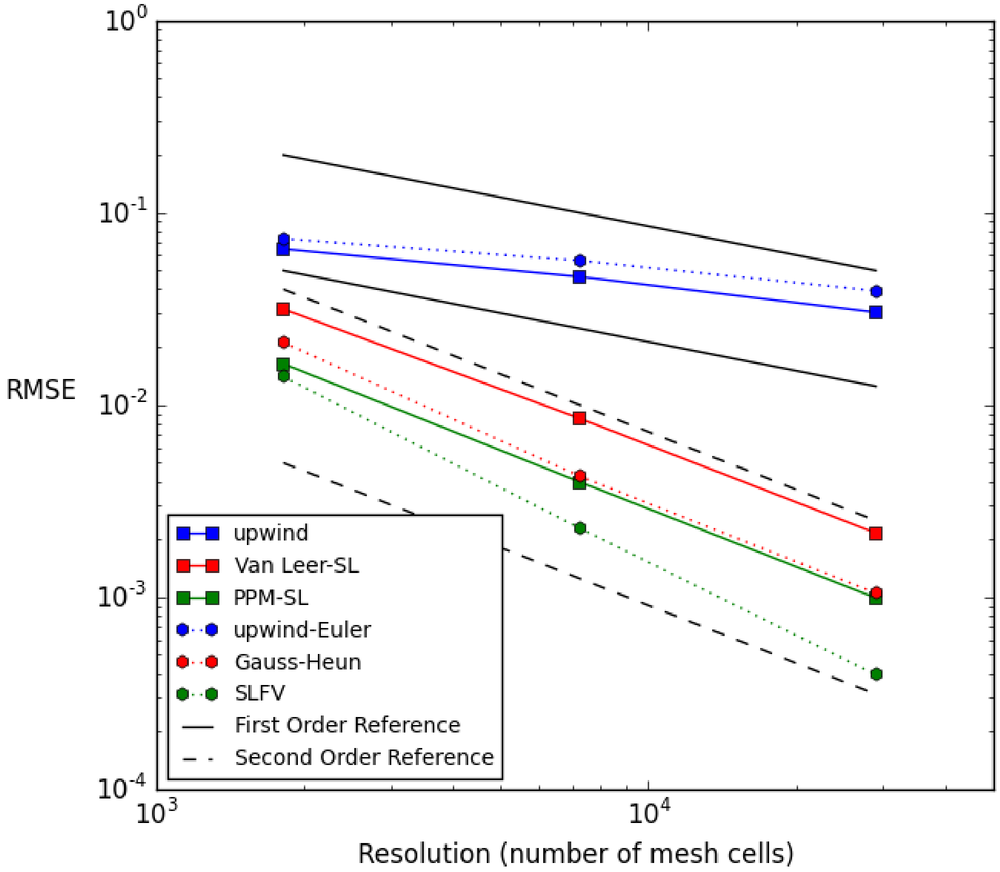

Figure 4.13: Root-mean-square error as a function of grid refinement for 2D Voronoi and Cartesian schemes under the tilted periodic solid-body wind field

schemes on the Cartesian grid. The SLFV scheme, with its semi-Lagrangian formulation and linear reconstruction of the concentration field, is comparable to the Van Leer scheme on the Cartesian grid. However, the SLFV scheme still considerably outperforms the Van Leer scheme. SLFV even strongly outperforms the PPM scheme, though the latter's parabolic reconstruction of the concentration field could—in principle—be deemed superior by design. Even though this partial conclusion is extremely encouraging for the substitution of Cartesian grids by Voronoi grids in CTMs, generalizing this conclusion to more demanding wind fields is not straightforward. To advance further in our comparison, we therefore move on to deformational wind fields.

4.4.3 NL2010 low-shear convergence

Fig. 4.14 shows the evolution of the total RMSE of all used schemes versus the mesh resolution, under the NL2010 wind field, with a relatively low amplitude for vortex velocity: $k = 3\ m.s^{-1}$. Low vortex velocity implies that the wind field is not as sheared as with the default vortex velocity of the NL2010 wind field. Fig. 4.14 shows results comparable as the ones obtained for solid-body rotation, but with an almost complete lack of convergence for first-order schemes. In

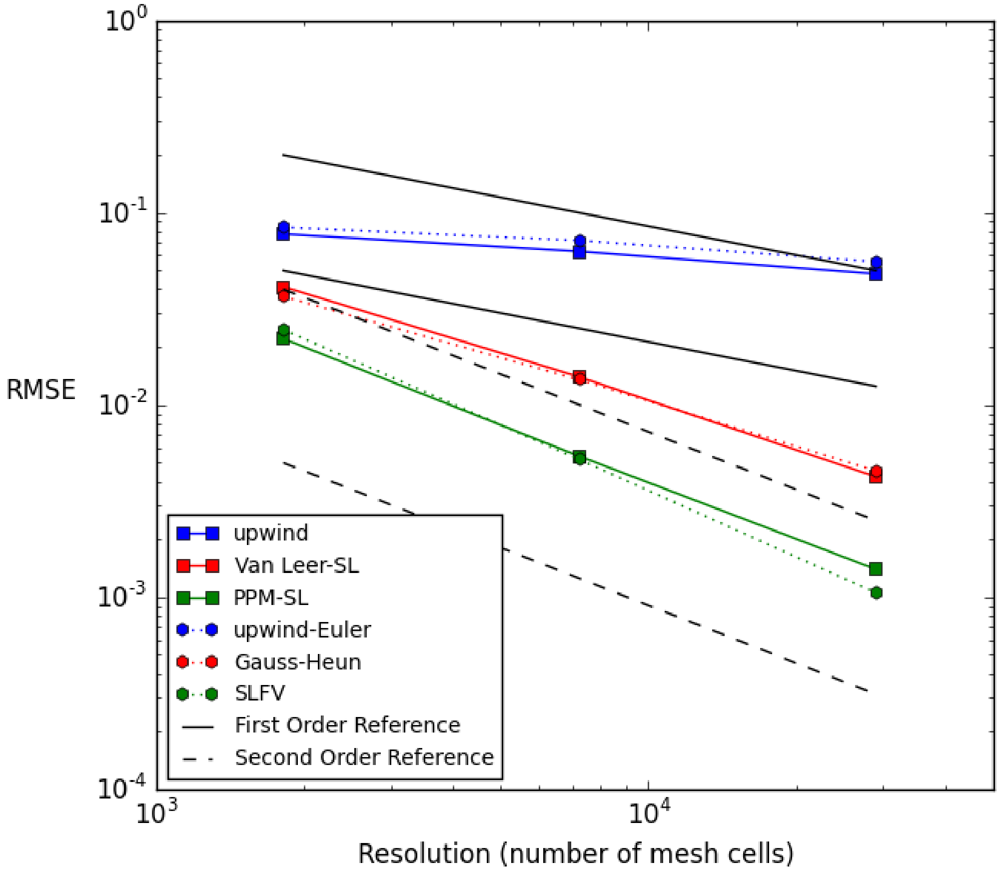

Figure 4.14: Root-mean-square error versus grid refinement for 2D Voronoi and Cartesian schemes under the NL2010 wind field, with a vortex velocity amplitude $k = 3\ m.s^{-1}$

this case, too, pushing resolution much further would be needed in order to observe convergence for these schemes.

For second-order schemes, a convergence rate at, or close to, order 2 is observed, as expected for the Van Leer scheme and the Gauss-Heun scheme. The SLFV scheme still outperforms the PPM scheme, but by a closer margin than with the non-deformational cases. The upwind schemes following both formulations again have the highest RMSE at the coarsest resolution, with the Cartesian one slightly less than the Voronoi one. The Van Leer scheme results in a lower RMSE at the coarsest resolution, very closely followed by the Gauss-Heun scheme. The SLFV and PPM schemes follow, with the PPM scheme starting with the lowest RMSE value with the coarsest mesh. As the mesh resolution increases, the RMSEs of all schemes decrease. The upwind schemes again decrease with a lower slope than the first-order reference lines, with almost equal slopes. The Van Leer and Gauss-Heun schemes decrease with a near-second-order slope, and their curves are practically superimposed. The SLFV and PPM schemes follow the slopes of the second order reference lines, with a slightly steeper descent for the SLFV scheme. As a result, the SLFV scheme has the lowest RMSE error at the finest resolution used in this study, only slightly exceeded by the PPM scheme's. We now increase the *difficulty* a bit more by increasing the vortex velocity amplitude.

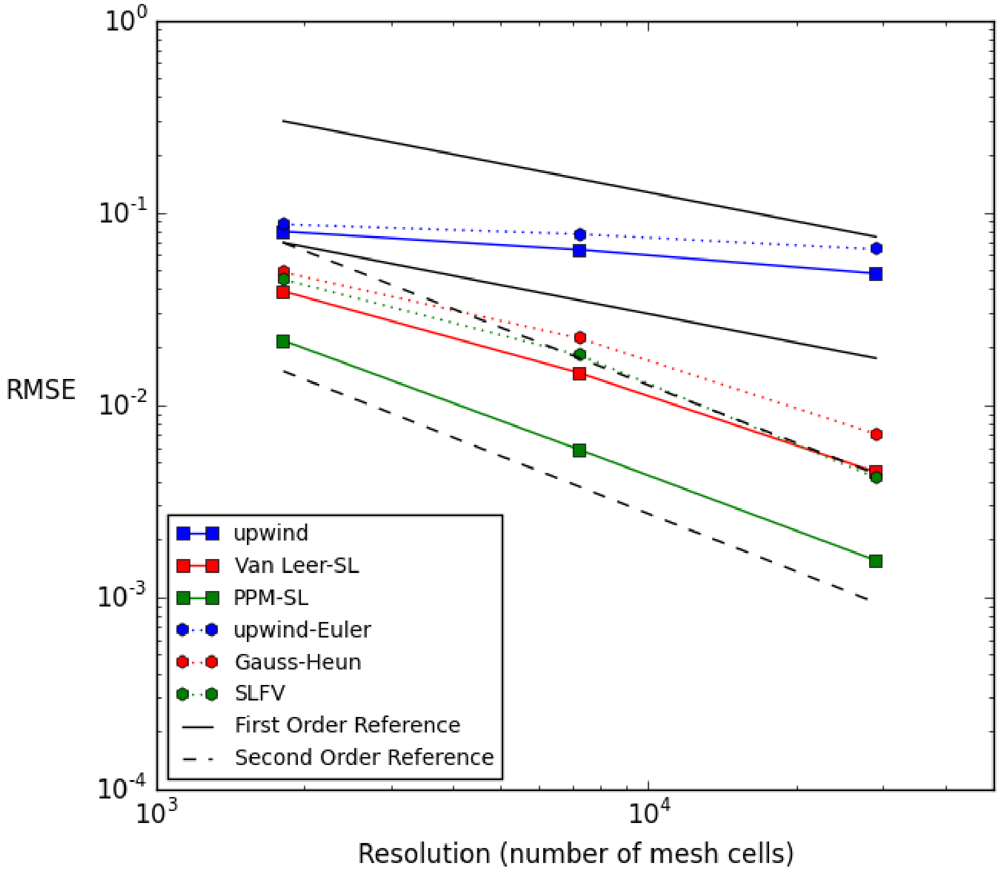

Figure 4.15: Root-mean-square error versus grid refinement for 2D Voronoi and Cartesian schemes under the NL2010 wind field, with a vortex velocity amplitude $k = 10\ m.s^{-1}$

4.4.4 NL2010 intermediate-shear convergence

Fig. 4.15 shows the evolution of the total RMSE of all used schemes versus the mesh resolution, under the NL2010 wind field, with an intermediate vortex velocity amplitude of $k = 10\ m.s^{-1}$, a threefold increase from the low-shear test-case above. Fig. 4.15 shows that, this time, only the SLFV and PPM schemes reach second-order convergence. However, under this more deformational test-case, the PPM scheme—with its parabolic formulation—achieves a better accuracy than the SLFV scheme. For this slightly more demanding test case, the Van Leer scheme on the Cartesian grid and the Gauss-Heun scheme on the Voronoi grid clearly fail to achieve second-order convergence at the resolutions we use. This result suggests an improvement in the performance of the Cartesian-grid schemes (compared to their Voronoi counterparts), which we investigate by imposing an even more demanding test-case.

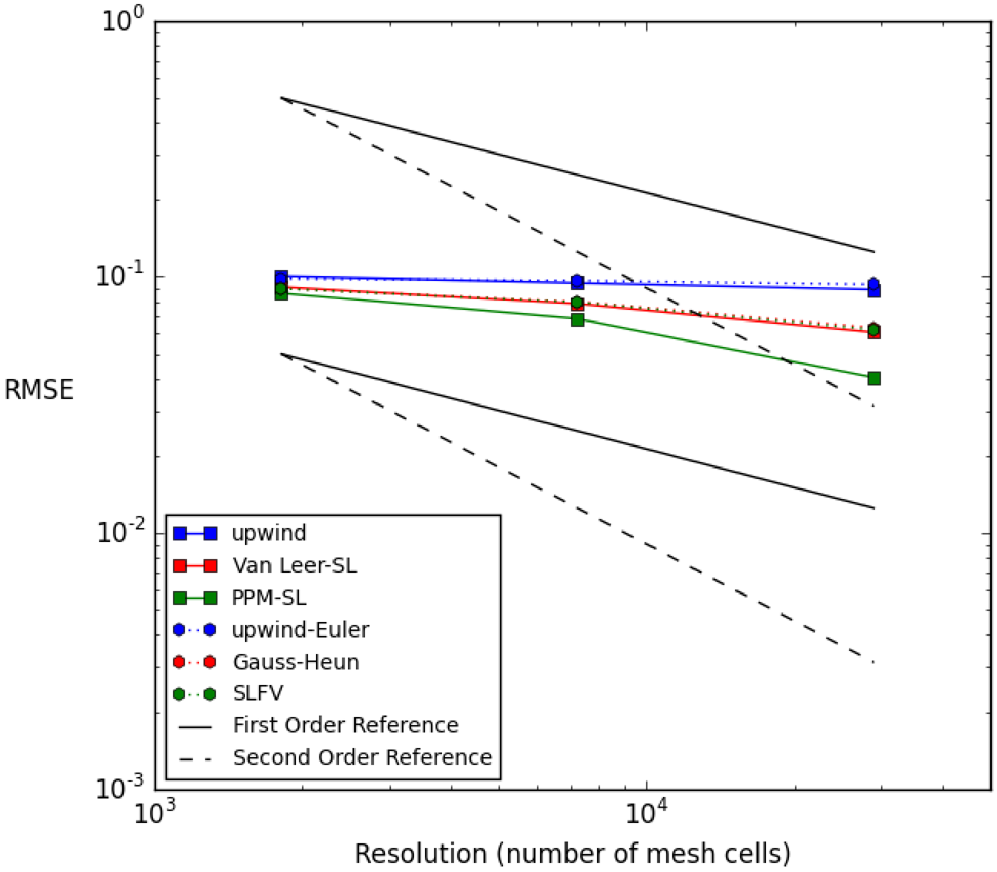

Figure 4.16: Root-mean-square error versus grid refinement for 2D Voronoi and Cartesian schemes under the NL2010 wind field, with a vortex velocity amplitude $k = \frac{10a}{T_{\text{exp}}}$

4.4.5 NL2010 default-shear convergence

Fig. 4.16 shows the evolution of the total RMSE of all used schemes versus the mesh resolution under the NL2010 wind field, with the default vortex velocity amplitude of $k = \frac{10a}{T_{\text{exp}}} \approx 61\ m.s^{-1}$. In this case, the wind field is extremely scheared, as in [Nair and Lauritzen, 2010]. Fig. 4.16 shows that, even though all schemes fail to display convergence up to their theoretical order—at the resolutions within our computational reach—the PPM scheme outperforms the SLFV scheme. The latter displays an accuracy and convergence rate comparable to—but not better than—the convergence obtained by the Van Leer scheme. The PPM scheme's superiority under this highly deformational wind field may be interpreted as an increased ability to follow sharp changes in concentration due to its parabolic (rather than linear) formulation.

Interestingly, for this highly deformational test case, first-order schemes fail to converge at all at the resolutions we have tested, an illustration of the difficulty and highly deformational character of this test case.

4.5 Partial conclusions

As a general conclusion for these idealized test-cases, a general trend seems to emerge: for simple, non-deformational test cases, the SLFV scheme strongly outperforms all the Cartesian schemes we have tested here. The performance of the Dubey et al. [2015] scheme is actually surprisingly good, exceedingly outperforming the Van Leer [1977] scheme with its comparable linear reconstructions, and even the Colella and Woodward [1984] scheme with its parabolic reconstructions of the concentration fields. This is, by itself, quite encouraging with regards to the use of Voronoi grids and their capabilities for variable resolution as an alternative to Cartesian grids for CTMs. Not only could this transition prove to be possible without a loss in accuracy, but it could even bring an improvement in accuracy if a semi-Lagrangian scheme, such as the one of Dubey et al. [2015], is used. However, when it comes to highly deformational and sheared flows—which often occur in the atmosphere due to the appearance of cyclones and anticyclones close to each other—the Cartesian-grid PPM scheme still retains an advantage compared to the SLFV scheme. Even the Van Leer [1977] scheme yields a performance comparable to the Dubey et al. [2015] SLFV scheme for strongly deformational flows.

This complex picture, with an advantage to Voronoi mesh schemes for non-deformational flows, but an improved performance of Cartesian-grid schemes when it comes to highly deformational flows, calls for real-life test cases with realistic wind and concentration fields. This imposes us to move on to three-dimensional flows in the next chapter.

Chapter 5

Puyehue-Cordón Caulle 3D Simulation Results

This chapter presents and discusses realistic simulations of transport of SO_2 emitted by the Puyehue-Cordón Caulle volcanic eruption of June 4, 2011. The simulations are made using the CHIMERE CTM on one side, and the DYNAMICO GCM on the other.

Space-borne observations, such as those of Figure 5.2 where the visible plume gives a good indication of the presence of SO_2, permit to gain confidence in the qualitative relevance of modelled results.

Our simulations include only the advection phenomenon, whereas, in reality, other processes affecting the volcanic plume exist. Furthermore, there are large uncertainties in actual volcanic-plume mass-fluxes. Nevertheless, the CHIMERE simulation has previously been shown to be consistent with observations [Mailler et al., 2017]. Therefore, we do not attempt a quantitative comparison between modelled and observed SO_2 concentrations. Instead, our analysis of the simulations is mainly aimed at comparing them to each other, especially with respect to numerical diffusion.

For a qualitative comparison, we analyse the trajectory of the plume. A quantitative comparison of numerical diffusion is performed by monitoring the minimal volume of air containing half the total mass of SO_2 (Section 5.3.3).

5.1 Puyehue-Cordón Caulle eruption

The *Puyehue–Cordón Caulle* volcanic complex, located in the Chilean southern Andes, underwent a violent volcanic eruption at 14:45 local time on the 4^{th} of June, 2011. The volcanic plume was expelled from the *We Pillán* vent, located 7 km north-west of the crater of the Puyehue volcano, at 40.58° south and 72.13° west, and at an altitude of 2240 meters above sea level [Raga et al., 2013].

The eruption produced a large plume of gas and ash that reached 10 km above crater-rim level [Raga et al., 2013], crossing the troposphere to the lower stratosphere (Fig. 5.1). The plume circled the South Pole within the Southern Hemisphere over the course of the following days, and was back in the vicinity of the emission source by June 14, 2011 [Herrick and Wunderman, 2013], [Klüser et al., 2012]. This eruption—with its plume containing volcanic ash and sulfur dioxide—is a perfect test case to evaluate the ability of a model to simulate circumpolar movements and to represent the location of an aerosol plume after several days of transport [Mailler et al., 2017].

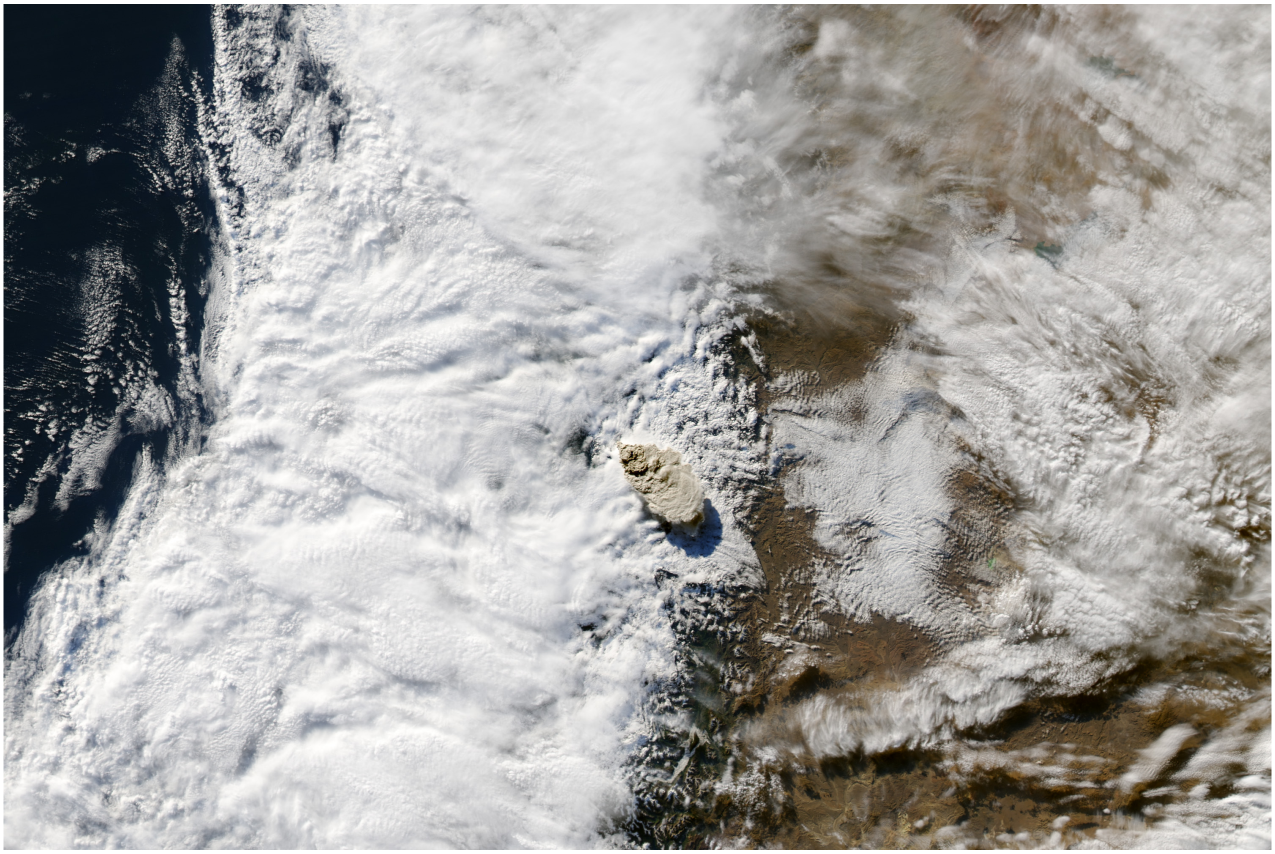

Figure 5.1: The top of the Puyehue–Cordón Caulle volcanic plume as seen from above (Jeff Schmaltz/MODIS Rapid Response Team/NASA-GSFC)

5.2 3D simulations

To provide a realistic support of the 2D experimental simulation conclusions, the advetion of the Puyehue-Cordón Caulle plume around the South Pole was simulated in 3D using CHIMERE and DYNAMICO. The results obtained using CHIMERE represent those of a Cartesian mesh on a curved surface. Those obtained using DYNAMICO, on the other hand, represent the results of a quasi-uniform unstructured hexagonal-pentagonal Voronoi mesh. Both representations have an extension in the 3rd dimension—the altitude—relative to the representations of the previous chapters. The 3D meshes of each formulation are detailed in the documentations of CHIMERE and DYNAMICO [Menut et al., 2013], [Dubos et al., 2015]. The schemes used in the CHIMERE formulation are the Van Leer spatial scheme, combined with Strang splitting [Menut et al., 2013]. On the DYNAMICO side, the time and space coupled SLFV scheme was used for the numerical solution of the advection equation, combined via Strang splitting to a one-dimensional Van Leer advection scheme in the vertical direction [Dubos et al., 2015].

The numerical parameters used in the 3D inter-comparison simulation is summarized in Table 5.1. We begin by ini-

Parameter	Value
Initial Concentration	Volcanic plume, negligible background
Wind Field	Real from the ERA5 dataset
Maximum Courant Number	0.8
Simulation Length	8 days
Tracer	SO_2
Vertical Refinement	99 pressure levels
Horizontal Refinement	approximately 50 km cell width

Table 5.1: Realistic 3D test case

tializing a mesh of similar refinement on both platforms, with enough resolution to represent the advection phenomenon at the hemispheric scale. We then initialize the wind fields using wind data from the ERA5 reanalysis—which finds data values from the past—dataset [C3S, 2017]. From the species emanating from the vent with the volcanic plume, we choose only the SO_2 molecules as tracers, as this species is inert and can easily be detected. The altitudes and rates at which SO_2 mass is injected to mimic the eruption are as in [Mailler et al., 2017], with an initial negligible background value, then sharply increasing in value at the vent's site following the eruption. The time step is adapted following the expression of Eq. 1.4 based on a maximum Courant-number of 0.8. The simulation is carried out for 8 experimental days, including the day of the eruption, to follow the revolution of the plume around the South Pole within the Southern Hemisphere.

5.3 Trajectory of the plume

In this section, we present the simulated advected plume's trajectory following three representations. Firstly, we present for each simulation a map of SO_2 concentration, at the 7th day following the eruption, at a certain model level. Then we present for each simulation the column-integrated value of the SO_2 concentration, i.e. integrated from the surface to the upper vertical bound of each mesh. Finally, we track with time the position of the maximum of the column-integrated SO_2 over the course of 8 days. This provides a qualitative view of the mostly eastwards advection of the plume by the wind in both simulations.

5.3.1 SO_2 concentration at 330 hPa

Figure 5.3 shows the CHIMERE simulated SO_2 plume slice at the 80th vertical level from the surface of the Earth, of a pressure around 330 hPa, and an altitude of approximately 8500 m at the 7th day following the eruption. This model level is chosen based on visual inspection which indicates that the plume is concentrated around its altitude. The bulk of the plume slice remains within the latitudes in the vicinity of the vent's latitude (50 degrees south), with some spreading to the north and south. In terms of longitude, the plume is seen to have traversed two-thirds of the longitudes of a rotation from the site of the eruption and around the pole (clockwise in Fig. 5.3). At this level, the SO_2 concentration is aggregated in broken trailing wisps throughout the Southern Hemisphere, and is mainly concentrated

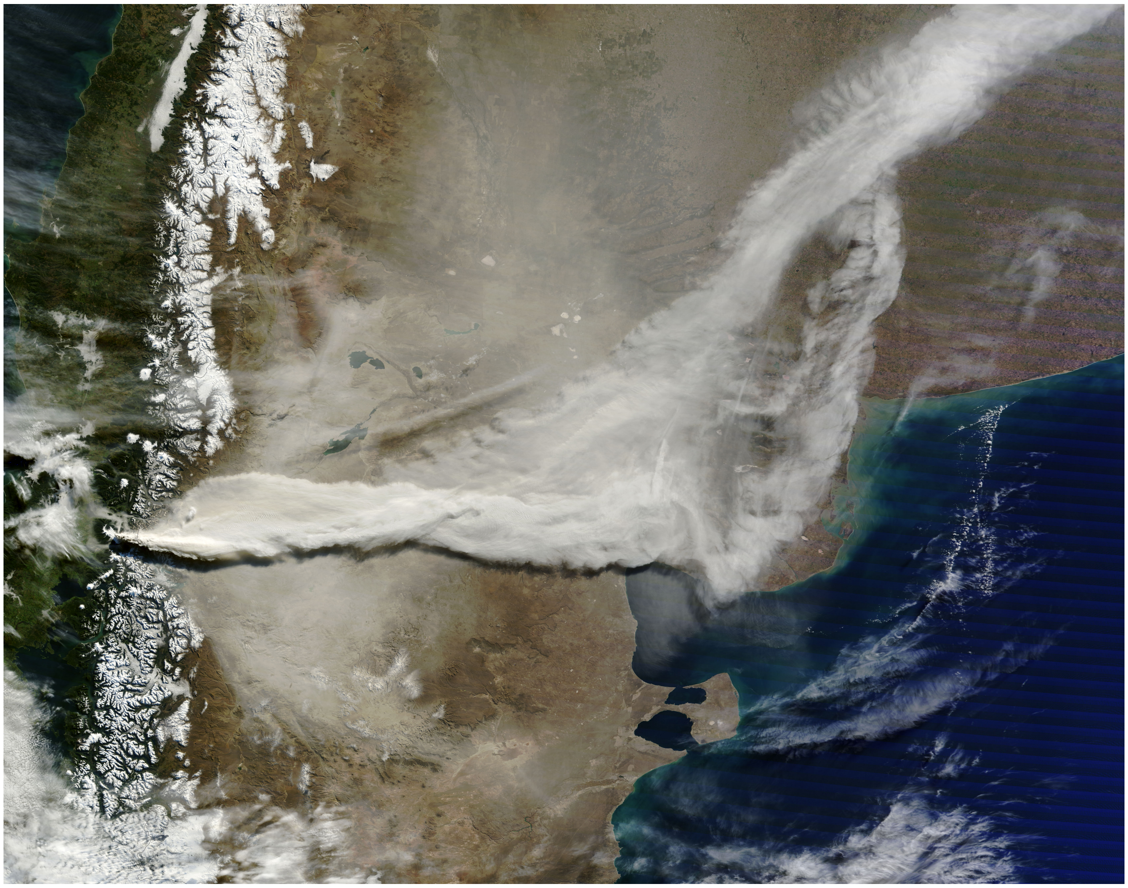

Figure 5.2: The transport of the Puyehue Cordon-Caulle volcanic plume over Argentina, as taken on June 13, 2011, by the Moderate Resolution Imaging Spectroradiometer (MODIS) on the Terra satellite. The image is oriented vertically to the North. (Jeff Schmaltz/MODIS Rapid Response Team/NASA GSFC)

within the longitudes of Australia and New Zealand, and within the latitudes to their south.

Figure 5.4, on the other hand, shows the same simulated quantity following a DYNAMICO simulation. In this figure, the plume slice has also crossed the same longitudes in its rotation around the pole, and again remains in the latitudes in the vicinity of the vent's latitude, without large spreading to the north and south. It exhibits the same distribution and shape as with CHIMERE, with some differences in spreading: the broken parts of the plume look slightly less horizontally diffused.

From both figures, we can infer that the emitted sharp plume maintains its *sharp* profile even with advection, though it diffuses and breaks into patches. The wisps remain well-defined over 7 days of rotation around the South Pole and do not immediately diffuse into the surrounding atmosphere. This suggests that the unstructured formulation, as the Cartesian formulation, allows the preservation of sharp concentration profiles to some extent. Furthermore, the unstructured formulation may cause less diffusion, though only to a small extent.

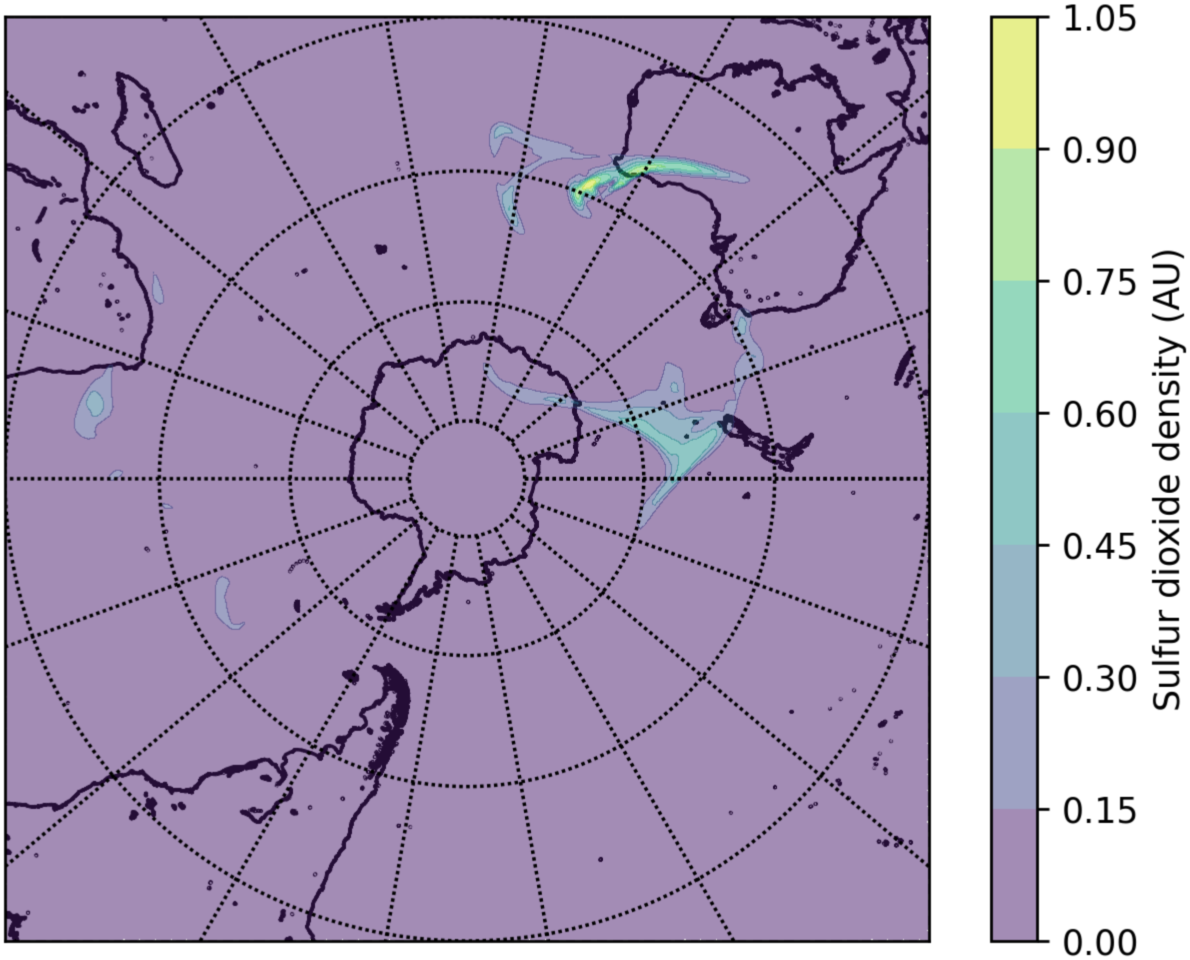

Figure 5.3: SO_2 concentration (arbitrary units) at the 80th vertical model level, corresponding to a pressure of about 330 hPa, and an altitude of approximately 8500 m, 7 days after the volcanic eruption in the CHIMERE simulation. Circles indicate latitudes 80, 60, 40 and 20 degrees South.

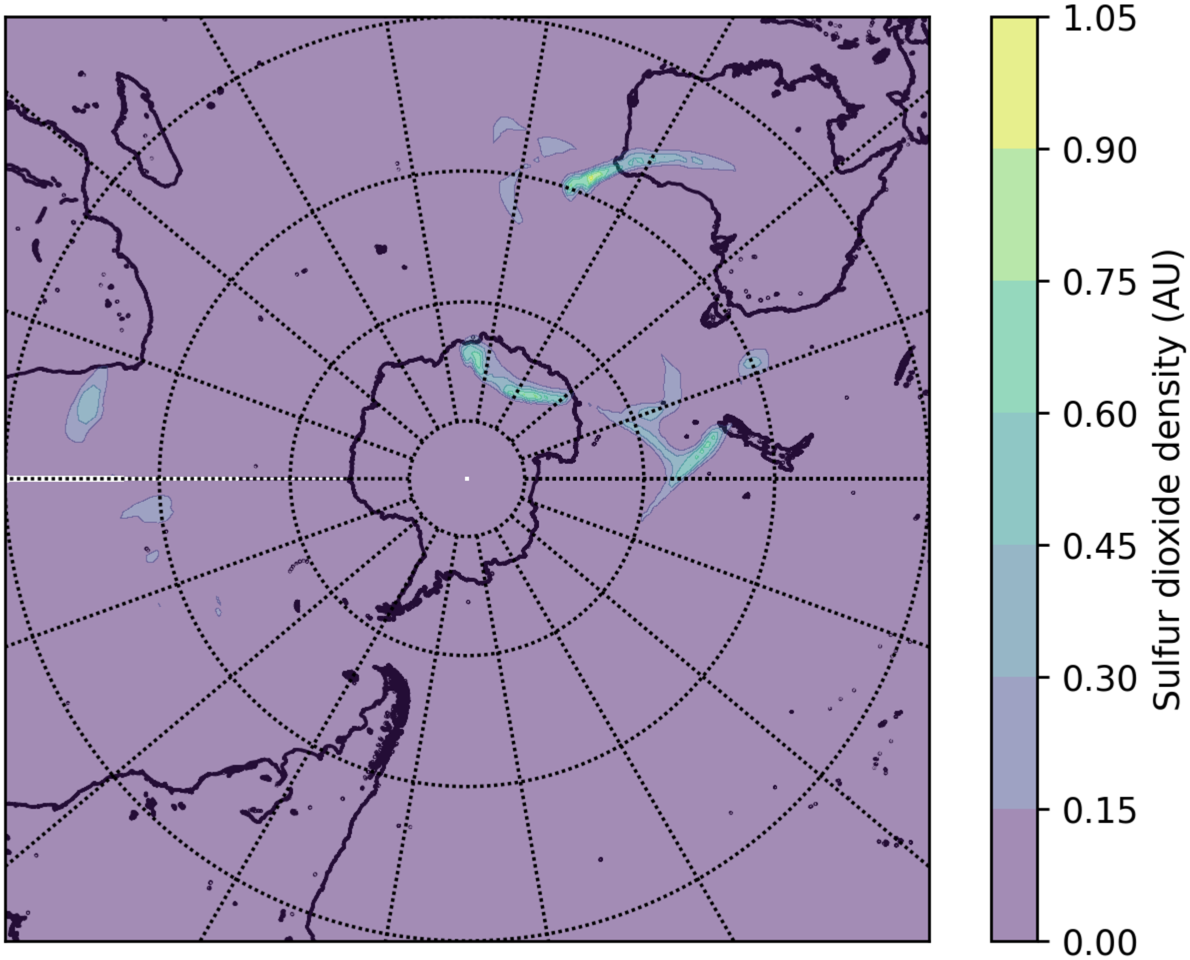

Figure 5.4: SO_2 concentration (arbitrary units) at the 80th vertical model level, corresponding to a pressure of about 330 hPa, and an altitude of approximately 8500 m, 7 days after the volcanic eruption in the DYNAMICO simulation. Circles indicate latitudes 80, 60, 40 and 20 degrees South.

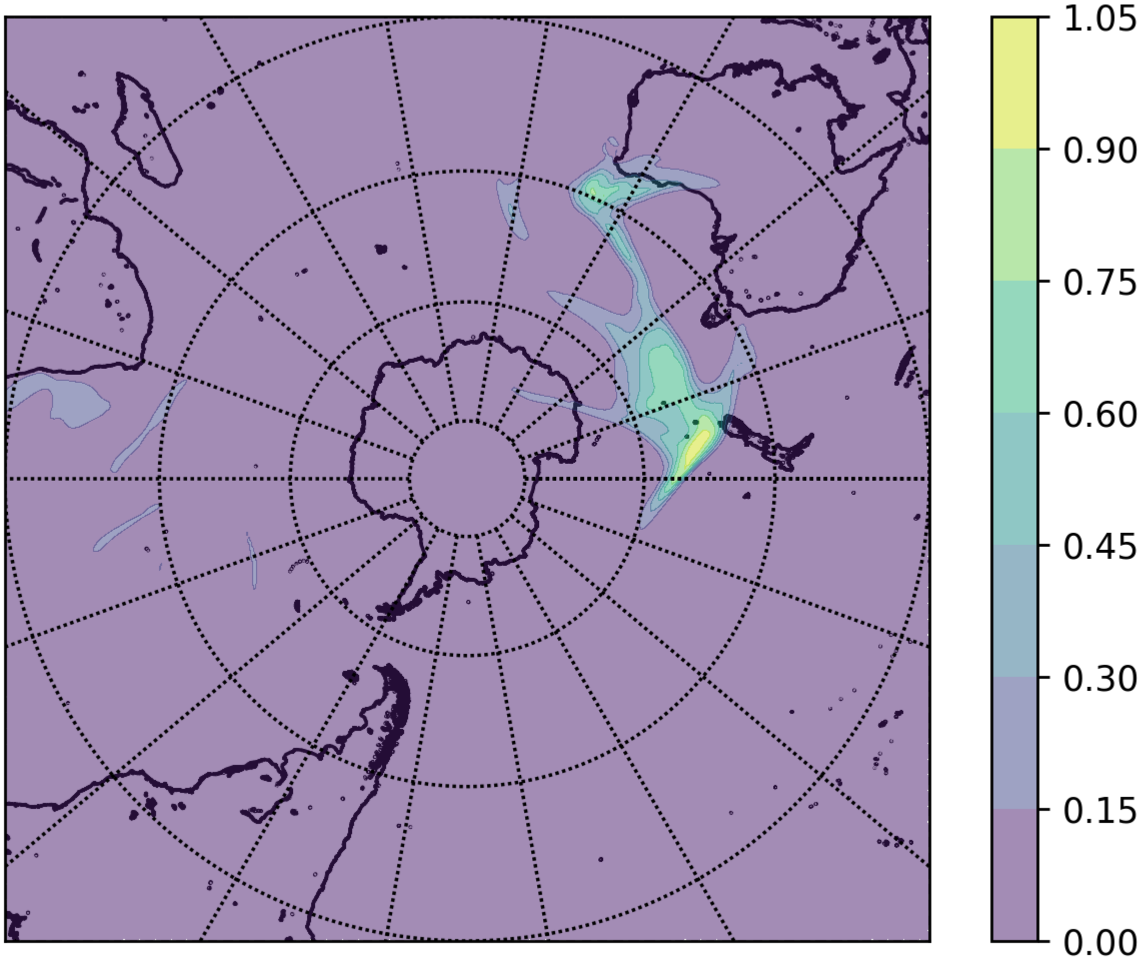

Figure 5.5: The column-integrated values, normalized to the maximum value, of the SO_2 plume 7 days after the volcanic eruption following a CHIMERE simulation. Circles indicate latitudes 80, 60, 40 and 20 degrees South.

5.3.2 Column-integrated SO_2 concentration

Instead of concentration at a single model level, we now consider the column-integrated concentration, still at day 7. We consider first the CHIMERE simulation (Figure 5.5). The main part of the plume is spread to the south of Australia and New Zealand, even extending to Antarctica, with the maximum concentration patch leading this main part near New Zealand. Small wisps can be seen trailing behind—in the rotation sense—the main body of the plume, to the west of South Africa and in the midst of the southern Atlantic ocean.

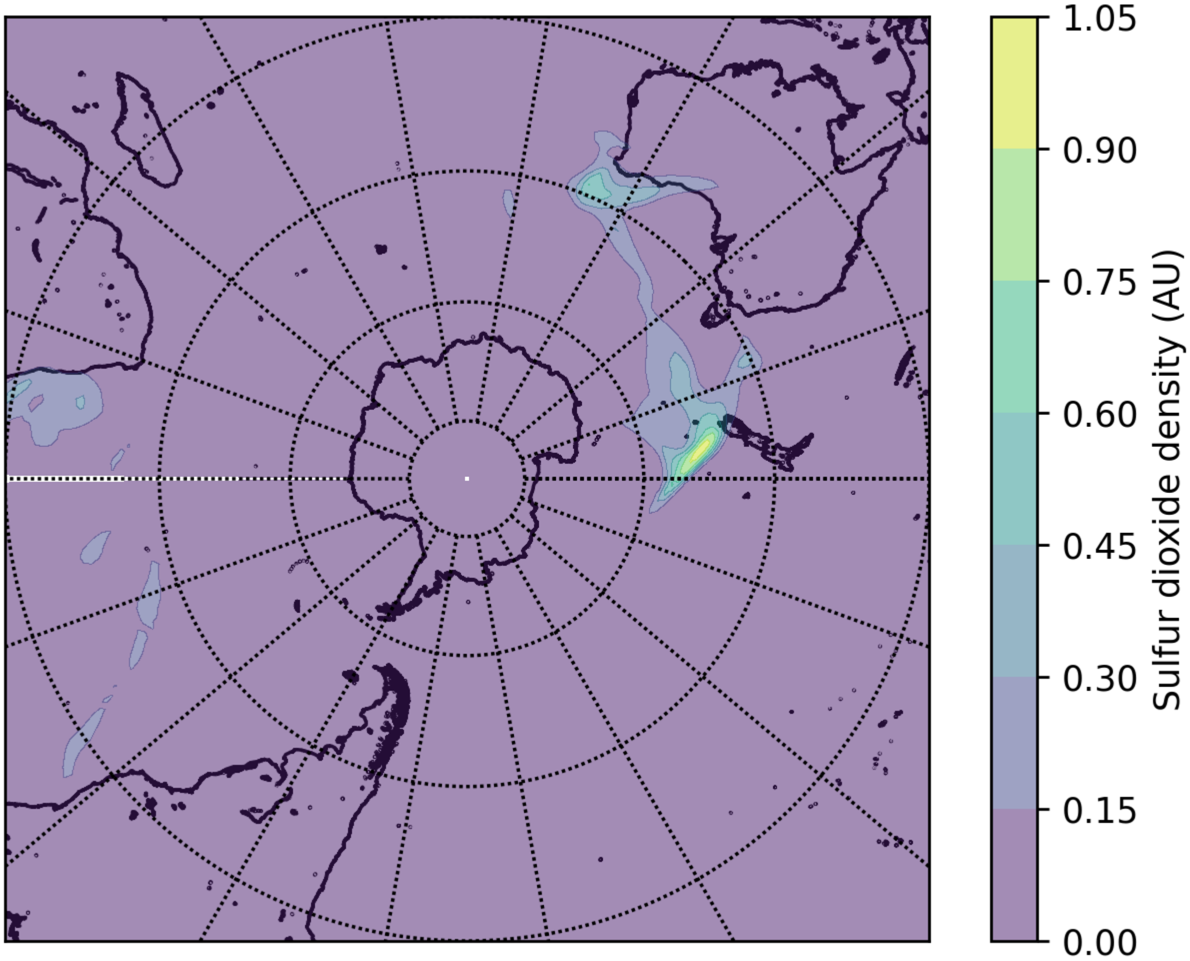

Figure 5.6: The column-integrated values, normalized to the maximum value, of the SO_2 plume 7 days after the volcanic eruption following a DYNAMICO simulation. Circles indicate latitudes 80, 60, 40 and 20 degrees South.

Taking the same quantity as above into consideration, but following a DYNAMICO formulation, we obtain the values portrayed in Figure 5.6. The main distribution of the simulated plume is quite similar to that of the CHIMERE formulation. However, as seen with the horizontal slice in Figure 5.4, the column-integrated plume seems slightly less diffused in the horizontal with the unstructured mesh. However, the trailing patches of the plume are more prominent as seen through this formulation, with a larger patch near South Africa, and longer wisps extending from the Brazilian coast to the midst of the southern Atlantic.

5.3.3 Plume trajectory

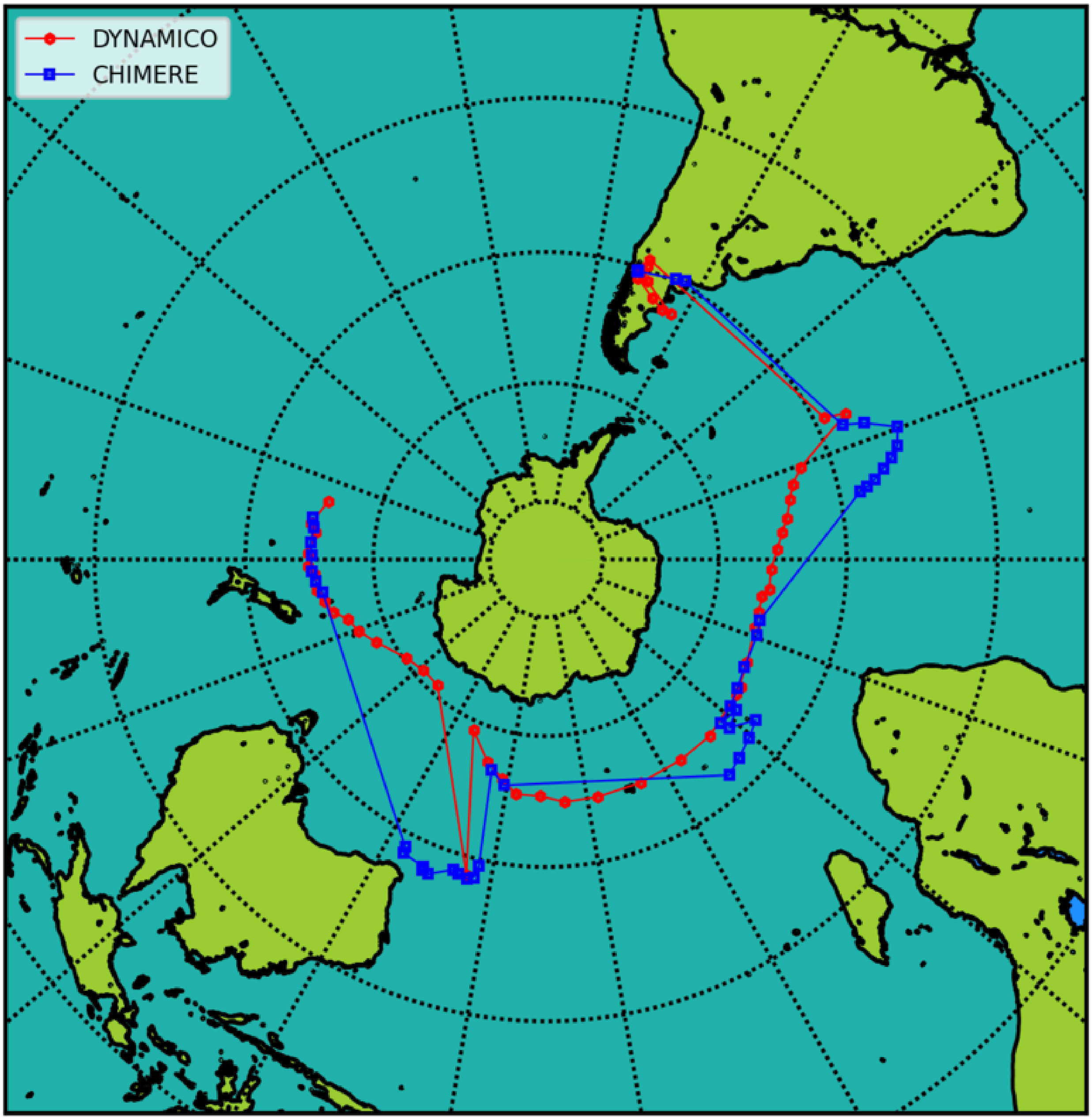

Figure 5.7: The trajectories of the maximum concentration columns of the volcanic plume following each of CHIMERE and DYNAMICO over the course of the 7 days following the eruption. Circles indicate latitudes 80, 60, 40 and 20 degrees South.

Finally, we track with time the position of the maximum of the column-integrated SO_2 over the course of 8 days (Figure 5.7). Figure 5.7 presents the resulting trajectories.

Figure 5.7 shows an initiation of the maximum-concentration column near the site of the volcanic eruption following both formulations. This is, of course, as expected. The trajectory of this column under both formulations follows a clockwise (relative to the figure) revolution around the South Pole, in an eastward direction, circumnavigating the pole.

Some discontinuities in these trajectories are visible. Also, there are periods when the maximum found in the DYNAMICO and CHIMERE simulations coincide closely, and also some intervals where they differ significantly. This can be attributed to the plume being concentrated in more than a single main region, so that the position of the maximum concentration sometimes undergoes a sudden jump, which does not occur exactly at the same time in both simulations. Nevertheless towards the end of the simulated period, both simulations produce maxima at nearby locations, as already verified with the maps presented in Figures 5.5 and 5.6.

At the end of the 7 days represented on the figure, the maximum column approaches the site of the eruption from the western side, completing 3 quarters of a revolution from its initial position.

Overall, we can conclude that the simulated plumes follow a similar evolution in both simulations. There are clear differences between the two simulations, but they remain qualitatively small even after 7 days. These differences can be attributed to the different errors incurred by each numerical method on its respective mesh. Following this qualitative verification, we now turn to a quantitative analysis of numerical diffusion in each simulation.

Numerical diffusion

To quantify the differences in diffusion between the two formulations, we track with time the half-mass volume of the plume. This volume is the minimum volume which contains half the total mass of SO_2 released in the atmosphere at any time. To compute it, we compute for each mesh cell its volume and SO_2 concentration. We then sort all mesh cells according to their SO_2 concentration. We then find the number N, such that the N cells with the highest concentrations represent half the total amount of SO_2 in the atmosphere. The half-mass volume is then the volume occupied by these N cells. The larger this volume, the more diffused the plume is.

During the eruption, the half-mass volume evolves due to injection of SO_2 into the atmosphere. However, after the end of the eruption, its increase is solely due to numerical diffusion. Since the plume is sharp, its half-mass volume represents a small fraction of the volume of the whole atmosphere. Figure 5.8 presents this fraction as a function of time during the 7 days following the eruption, for both CHIMERE and DYNAMICO simulations.

With the progression of time, the half-mass volume increases following both formulations. The slope of this increase remains positive, but decreases with the further advance in time, up to the end of the simulation. After the third simulated day, the half-plume volume following the unstructured formulation begins to increase beyond that of the structured formulation, exceeding it by a slight amount at the end of the simulation.

Thus, the main body of the plume is slightly more diffused following the unstructured formulation, though the half-mass volumes remain quite close. We can therefore conclude that, according to this measure, the two formulations are rather comparable, with some additional diffusion seen in terms of the spreading of the main body of the plume.

5.4 Summary

In this chapter, we followed the volcanic plume of the Puyehue-Cordón Caulle eruption as simulated by the advection modelling of the CHIMERE CTM and the DYNAMICO GCM in the few days following the event. We visualized these

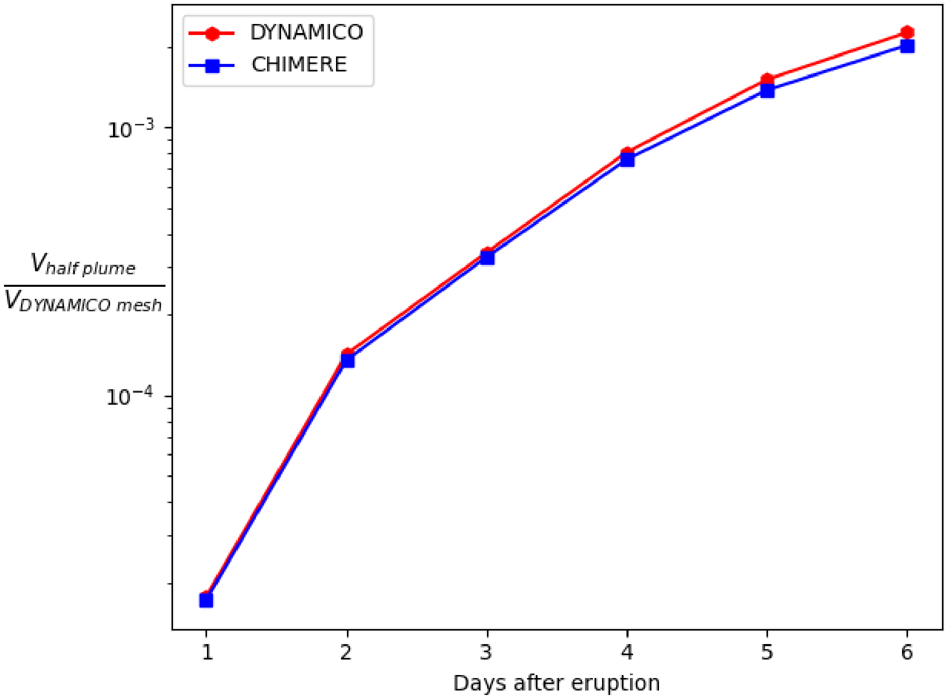

Figure 5.8: The minimum volume occupied by half of the plume's SO_2 mass in CHIMERE and DYNAMICO relative to the total volume of the full mesh over the course of the 7 days following the eruption

simulations by tracking the simulated plume as it circumnavigated the pole, and the maximum-concentration column as its position changed with numerical advection.

We found that DYNAMICO tracked the trajectory of the plume as well as CHIMERE, preserving its sharpness relative to the surrounding atmosphere. Furthermore the unstructured formulation of DYNAMICO produced only marginally more numerical diffusion than the CHIMERE Cartesian formulation.

Chapter 6

Conclusion

In this final chapter, we highlight the most significant results of the thesis. Following this summary, future work that would further establish confidence in the obtained results are considered. In a second section, the implications of the results already obtained for chemistry-transport modelling are discussed. Perspectives and future work are considered.

6.1 Main results

In this thesis, we have explored the viability of the replacement of the structured Cartesian longitude-latitude mesh of a chemistry transport model (CTM) with an unstructured hexagonal-pentagonal Voronoi mesh. Both meshes permit the numerical solution of the advection equation, which is a key component of numerical models studying atmospheric composition. This phenomenon was accordingly chosen for our research. We have identified a portfolio of numerical schemes of different order and structure formulated on two-dimensional versions of each mesh type.

In a first step, we carried out two-dimensional idealized numerical experiments (Chapter 3) and used a set of numerical metrics for each mesh-scheme pair to evaluate their stability, monotonicity, numerical diffusivity, and convergence (Chapter 4).

Some outcomes of Chapter 4 are a mere confirmation of expectations. All schemes are stable up to Courant numbers close to 1. Numerical diffusion is reduced at higher resolution and with higher-order schemes, which are also better at preserving an existing non-linear relationship between tracers. Second-order schemes converge according to theoretical expectations provided the wind field is simple enough. Upwind schemes are very diffusive on both meshes and hardly converge at the resolutions we employ.

In addition to these unsurprising outcomes, we gained some insight especially onto the second-order schemes. In terms of numerical diffusion, the hierarchy between the studied schemes is that the Cartesian PPM scheme performs best, followed by the Voronoi scheme SLFV. They are followed by Gauss-Heun (Voronoi) and Van Leer (Cartesian), which are on par. For certain wind fields, the Gauss-Heun scheme produces a large amount of un-mixing, significantly more than SLFV. In the presence of strong wind shear, only the PPM scheme produces an acceptable level of numerical diffusion, at least at the highest resolution studied.

From these observations, reinforced by a similar behavior with respect to convergence, a general trend seems to emerge: for simple, non-deformational test cases, the SLFV scheme outperforms the Van Leer [1977] scheme with its comparable linear reconstructions, and even the Colella and Woodward [1984] scheme with its parabolic reconstructions of the concentration fields. This is, by itself, quite encouraging with regards to the use of Voronoi grids and their capabilities for variable resolution as an alternative to Cartesian grids for CTMs. However, when it comes to highly deformational and sheared flows—which often occur in the atmosphere due to the appearance of cyclones and anticyclones close to each other—the Cartesian-grid PPM scheme still retains an advantage compared to the SLFV scheme.

In Chapter 5, the 2D idealized test cases were complemented by a realistic three-dimensional numerical simulation of the volcanic plume emitted by the Puyehue-Cordón Caulle eruption in Chile on June 4, 2011. The plume of this eruption was sharp, and so its advection in the atmosphere was easy to track. Our numerical setup took advantage of a previous simulation of this event [Mailler et al., 2017].

We followed the advection of this plume using CHIMERE—a state-of-the-art CTM based on a hemispheric structured Cartesian mesh—on one hand, and DYNAMICO—a general circulation model (GCM) based on a global quasi-uniform unstructured hexagonal-pentagonal Voronoi grid—on the other hand. A qualitative analysis of the overall plume trajectory and shape confirmed that, while the concentration fields simulated by both models present some differences, they are sufficiently similar to continue with a quantitative comparison in terms of numerical diffusion. The very similar time-evolution of the half-plume volume in both simulations shows that, at least for this particular event, the transition from a Cartesian mesh to a Voronoi mesh did not incur a significant increase in numerical diffusion.

While this result is not quite a breakthrough, its importance for the question of the applicability of Voronoi meshes to CTMs should not be underestimated. Indeed, it is highly probable that, with proper evaluation and experimentation, variable-resolution simulations will provide benefits compared to uniform-resolution simulations with the same numerical schemes. Therefore, it is quite important to assess the cost of the transition from one numerical method to another at a given uniform resolution. The fact that this cost is low implies that it will be necessary to compensate inferior numerics by higher resolution, so that any smarter grid construction should deliver a net gain, at least in terms of reducing numerical diffusion by transport.

6.2 Perspectives for chemistry-transport modeling

The results presented in this thesis confirm that unstructured meshes are a promising direction for chemistry transport models. Specifically, we found that—not only in idealized setups but also in a realistic case—finite-volume schemes formulated on unstructured spherical meshes deliver a performance similar to Cartesian schemes, especially with respect to numerical diffusion. These results, although incomplete, suggest that pursuing this direction, which represents an significant investment to restructure existing codes, should be worth the effort.

To fully justify such an effort, the present work should be complemented by additional investigations. For instance, it would be useful to study more realistic cases. This could include other volcanic eruptions, such as the 2012 eruption of mount Etna [Lachatre et al., 2020], or the 2010 eruption of mount Eyjafjallajökull [Colette et al., 2011], and also other localized sources of plumes such as large-scale fires [Khaykin et al., 2020].

This work can be undertaken with the second-order schemes studied in the present work, but it may also be useful to revisit the value of higher-order schemes. Indeed, our results confirm that there is quite a gap between the Van Leer scheme and PPM on the Cartesian schemes, and higher-order schemes have also been designed for spherical Voronoi meshes [Skamarock and Gassmann, 2011, Zheng et al., 2021]. It would be useful to evaluate the reduction in numerical diffusion brought by the PPM scheme in the Puyehue case and other cases as mentioned above. This would provide a basis to borrow from existing higher-order unstructured transport-schemes or to develop new ones.

In this work we have focused on horizontal advection only. However, Zhuang et al. [2018] among others have shown the importance of reducing vertical diffusion as well. This can be achieved by using, for vertical advection, higher-order schemes like PPM, or anti-diffusive schemes as explored in [Lachatre et al., 2020].

Even at uniform resolution, our results suggest that Voronoi meshes, which allow for a full meshing of the Earth, without pole singularities nor patching, provide a viable alternative for global CTMs. Beyond uniform-resolution numerical experiments, developing a methodology to take advantage of the variable-resolution capability offered by unstructured meshes represents a significant amount of future work. Indeed, it is necessary to define a refined region and how much it should be refined, generate the corresponding Voronoi mesh, and evaluate the added value of simulations using this mesh, as [Kramer et al., 2020] did for atmospheric dynamics with MPAS. For instance, in the case of the Puyehue eruption, a simple idea would be to enhance resolution within a band of latitudes containing the volcano and the plume, e.g. between 20 and 60 degrees South. Hopefully, experience gained with several real cases will lead to a methodology to define tailored variable-resolution meshes which provide a significant improvement in terms of simulation quality at an affordable computational cost.

Chapter 7

Sommaire en français

Dans ce dernier chapitre, nous mettons en évidence les résultats les plus significatifs de la thèse. Après ce résumé, les travaux futurs qui permettraient d'établir davantage la confiance dans les résultats obtenus sont envisagés. Dans une deuxième section, les implications des résultats déjà obtenus pour la modélisation chimie-transport sont discutées. Les perspectives et les travaux futurs sont envisagés.

7.1 Résultats principaux

Dans cette thèse, nous avons exploré la viabilité du remplacement du maillage cartésien structuré longitude-latitude d'un modèle de transport de la chimie (MTC) par un maillage de Voronoï hexagonal-pentagonal non structuré. Les deux maillages permettent la résolution numérique de l'équation d'advection, qui est un élément clé des modèles numériques étudiant la composition de l'atmosphère. Ce phénomène a donc été choisi pour notre recherche. Nous avons identifié un portefeuille de schémas numériques d'ordre et de structure différents formulés sur des versions bidimensionnelles de chaque type de maillage.

Dans un premier temps, nous avons réalisé des expériences numériques bidimensionnelles idéalisées (chapitre 3) et utilisé un ensemble de métriques numériques pour chaque paire maillage-schéma afin d'évaluer leur stabilité, leur monotonicité, leur diffusivité numérique et leur convergence (chapitre 4).

Certains résultats du chapitre 4 sont une simple confirmation des attentes. Tous les schémas sont stables jusqu'à des nombres de Courant proches de 1. La diffusion numérique est réduite à une résolution plus élevée et avec des schémas d'ordre supérieur, qui sont également meilleurs pour préserver une relation non linéaire existante entre les traceurs. Les schémas de second ordre convergent conformément aux attentes théoriques, à condition que le champ de vent soit suffisamment simple. Les schémas de vent ascendant sont très diffusifs sur les deux mailles et convergent à peine aux résolutions que nous employons.

En plus de ces résultats peu surprenants, nous avons obtenu quelques informations, en particulier sur les schémas de second ordre. En termes de diffusion numérique, la hiérarchie entre les schémas étudiés est que le schéma cartésien PPM est le plus performant, suivi du schéma de Voronoï SLFV. Ils sont suivis par Gauss-Heun (Voronoï) et Van Leer (cartésien), qui sont à égalité. Pour certains champs de vent, le schéma Gauss-Heun produit une grande quantité de non-mixage, nettement plus que le SLFV. En présence d'un fort cisaillement du vent, seul le schéma PPM produit un niveau acceptable de diffusion numérique, du moins à la plus haute résolution étudiée.

À partir de ces observations, renforcées par un comportement similaire en ce qui concerne la convergence, une tendance générale semble émerger : pour des cas de test simples et non déformés, le schéma SLFV surpasse le schéma Van Leer [1977] avec ses reconstructions linéaires comparables, et même le schéma Colella and Woodward [1984] avec ses reconstructions paraboliques des champs de concentration. Ces résultats sont, en soi, assez encourageants en ce qui concerne l'utilisation des grilles de Voronoï et leurs capacités de résolution variable comme alternative aux grilles cartésiennes pour les MTC. Cependant, lorsqu'il s'agit d'écoulements fortement déformés et cisaillés - ce qui se produit souvent dans l'atmosphère en raison de l'apparition de cyclones et d'anticyclones proches les uns des autres - le schéma PPM à grille cartésienne conserve un avantage par rapport au schéma SLFV.

Au chapitre 4, les cas d'essai idéalisés en 2D ont été complétés par une simulation numérique tridimensionnelle réaliste du panache volcanique émis par l'éruption de Puyehue-Cordón Caulle au Chili le 4 juin 2011. Le panache de cette éruption était net, et son advection dans l'atmosphère était donc facile à suivre. Notre configuration numérique a tiré parti d'une simulation antérieure de cet événement [Mailler et al., 2017].

Nous avons suivi l'advection de ce panache à l'aide de CHIMERE–un MTC de pointe basé sur un maillage cartésien structuré hémisphérique–d'une part, et de DYNAMICO–un modèle de circulation générale (MCG) basé sur une grille de Voronoï hexagonale-pentagonale globale quasi-uniforme non structurée–d'autre part. Une analyse qualitative de la trajectoire et de la forme globale du panache a confirmé que, si les champs de concentration simulés par les deux modèles présentent quelques différences, ils sont suffisamment similaires pour poursuivre une comparaison quantitative en termes de diffusion numérique. L'évolution temporelle très similaire du volume du demi-plume dans les deux simulations montre que, au moins pour cet événement particulier, le passage d'un maillage cartésien à un maillage de Voronoï n'a pas entraîné une augmentation significative de la diffusion numérique.

Bien que ce résultat ne constitue pas une véritable percée, son importance pour la question de l'applicabilité des maillages de Voronoï aux MTC ne doit pas être sous-estimée. En effet, il est très probable qu'avec une évaluation et une expérimentation appropriées, les simulations à résolution variable présentent des avantages par rapport aux simulations à résolution uniforme avec les mêmes schémas numériques. Par conséquent, il est très important d'évaluer le coût de la transition d'une méthode numérique à une autre à une résolution uniforme donnée. Le fait que ce coût soit faible implique qu'il sera nécessaire de compenser une numérique inférieure par une résolution plus élevée, de sorte que toute construction de grille plus intelligente devrait apporter un gain net, au moins en termes de réduction de la diffusion numérique par transport.

7.2 Perspectives pour la modélisation chimie-transport

Les résultats présentés dans cette thèse confirment que les maillages non structurés constituent une direction prometteuse pour les MTC. Plus précisément, nous avons constaté que—non seulement dans des configurations idéalisées mais aussi dans un cas réaliste–les schémas de volumes finis formulés sur des maillages sphériques non structurés offrent une performance similaire aux schémas cartésiens, en particulier en ce qui concerne la diffusion numérique. Ces résultats, bien qu'incomplets, suggèrent que la poursuite de cette direction, qui représente un investissement important pour restructurer les codes existants, devrait en valoir la peine.

Pour justifier pleinement un tel effort, le présent travail devrait être complété par des investigations supplémentaires.

Par exemple, il serait utile d'étudier des cas plus réalistes. Cela pourrait inclure d'autres éruptions volcaniques, comme l'éruption de l'Etna en 2012 [Lachatre et al., 2020], ou l'éruption de l'Eyjafjallajökull en 2010 [Colette et al., 2011], et aussi d'autres sources localisées de panaches comme les feux à grande échelle [Khaykin et al., 2020].

Ce travail peut être entrepris avec les schémas de second ordre étudiés dans le présent travail, mais il peut également être utile de revoir l'intérêt des schémas d'ordre supérieur. En effet, nos résultats confirment qu'il existe un écart important entre le schéma de Van Leer et PPM sur les schémas cartésiens, et des schémas d'ordre supérieur ont également été conçus pour les maillages de Voronoï sphériques : [Skamarock and Gassmann, 2011, Zheng et al., 2021]. Il serait utile d'évaluer la réduction de la diffusion numérique apportée par le schéma PPM dans le cas de Puyehue et dans d'autres cas mentionnés ci-dessus. Cela permettrait d'emprunter des schémas de transport non structurés d'ordre supérieur existants ou d'en développer de nouveaux.

Dans ce travail, nous nous sommes concentrés sur l'advection horizontale uniquement. Cependant, Zhuang et al. [2018] entre autres ont montré l'importance de réduire également la diffusion verticale. Ceci peut être réalisé en utilisant, pour l'advection verticale, des schémas d'ordre supérieur comme le PPM, ou des schémas anti-diffusion comme exploré dans [Lachatre et al., 2020].

Même à résolution uniforme, nos résultats suggèrent que les maillages de Voronoï, qui permettent un maillage complet de la Terre, sans singularités de pôles ni patchs, constituent une alternative viable pour les MTC globaux. Au-delà des expériences numériques à résolution uniforme, le développement d'une méthodologie permettant de tirer parti de la capacité de résolution variable offerte par les maillages non structurés représente une quantité importante de travaux futurs. En effet, il est nécessaire de définir une région raffinée et son degré de raffinement, de générer le maillage de Voronoï correspondant et d'évaluer la valeur ajoutée des simulations utilisant ce maillage, comme l'a fait [Kramer et al., 2020] pour la dynamique atmosphérique avec MPAS. Par exemple, dans le cas de l'éruption du Puyehue, une idée simple serait d'améliorer la résolution dans une bande de latitudes contenant le volcan et le panache, par exemple entre 20 et 60 degrés Sud. Avec un peu de chance, l'expérience acquise avec plusieurs cas réels conduira à une méthodologie permettant de définir des maillages à résolution variable sur mesure qui apporteront une amélioration significative en termes de qualité de simulation à un coût de calcul abordable.

Bibliography

Akio Arakawa. Computational design for long-term numerical integration of the equations of fluid motion: Two-dimensional incompressible flow. part i. *Journal of Computational Physics*, 1(1):119–143, 1966. ISSN 0021-9991. doi: https://doi.org/10.1016/0021-9991(66)90015-5. URL `https://www.sciencedirect.com/science/article/pii/0021999166900155`.

Akio Arakawa and Vivian R. Lamb. A potential enstrophy and energy conserving scheme for the shallow water equations. *Monthly Weather Review*, 109(1):18 – 36, 1981. doi: 10.1175/1520-0493(1981)109⟨0018:APEAEC⟩2.0.CO;2. URL `https://journals.ametsoc.org/view/journals/mwre/109/1/1520-0493_1981_109_0018_apeaec_2_0_co_2.xml`.

Jeffrey M Augenbaum and Charles S Peskin. On the construction of the voronoi mesh on a sphere. *Journal of Computational Physics*, 59(2):177–192, 1985. ISSN 0021-9991. doi: https://doi.org/10.1016/0021-9991(85)90140-8. URL `https://www.sciencedirect.com/science/article/pii/0021999185901408`.

Yuya Baba, Keiko Takahashi, Takeshi Sugimura, and Koji Goto. Dynamical core of an atmospheric general circulation model on a yin–yang grid. *Monthly Weather Review*, 138(10):3988 – 4005, 2010. doi: 10.1175/2010MWR3375.1. URL `https://journals.ametsoc.org/view/journals/mwre/138/10/2010mwr3375.1.xml`.

L. Bindle, R. V. Martin, M. J. Cooper, E. W. Lundgren, S. D. Eastham, B. M. Auer, T. L. Clune, H. Weng, J. Lin, L. T. Murray, J. Meng, C. A. Keller, W. M. Putman, S. Pawson, and D. J. Jacob. Grid-stretching capability for the geos-chem 13.0.0 atmospheric chemistry model. *Geoscientific Model Development*, 14(10):5977–5997, 2021. doi: 10.5194/gmd-14-5977-2021. URL `https://gmd.copernicus.org/articles/14/5977/2021/`.

C3S. Era5: Fifth generation of ecmwf atmospheric reanalyses of the global climate, 2017. data retrieved September 2021, `https://cds.climate.copernicus.eu/cdsapp#!/home`.

Richard L. Carpenter, Kelvin K. Droegemeier, Paul R. Woodward, and Carl E. Hane. Application of the piecewise parabolic method (ppm) to meteorological modeling. *Monthly Weather Review*, 118(3):586 – 612, 1990. doi: 10.1175/1520-0493(1990)118⟨0586:AOTPPM⟩2.0.CO;2. URL `https://journals.ametsoc.org/view/journals/mwre/118/3/1520-0493_1990_118_0586_aotppm_2_0_co_2.xml`.

G. Chesshire and W. D. Henshaw. Composite overlapping meshes for the solution of partial differential equations. *Journal of Computational Physics*, 90(1):1–64, 1990. ISSN 0021-9991. doi: https://doi.org/10.1016/0021-9991(90)90196-8. URL `https://www.sciencedirect.com/science/article/pii/0021999190901968`.

CNRM. MOCAGE, 2014. URL `https://www.umr-cnrm.fr/spip.php?article128&lang=fr#outil_sommaire_1`.

P. Colella and P. R. Woodward. The piecewise parabolic method (PPM) for gas-dynamical simulations. *Journal of Computational Physics*, 54(1):174 – 201, 1984. ISSN 0021-9991. doi: https://doi.org/10.1016/0021-9991(84)90143-8. URL `http://www.sciencedirect.com/science/article/pii/0021999184901438`.

Phillip Colella and Michael D. Sekora. A limiter for ppm that preserves accuracy at smooth extrema. *Journal of Computational Physics*, 227(15):7069 – 7076, 2008. ISSN 0021-9991. doi: https://doi.org/10.1016/j.jcp.2008.03.034.

Augustin Colette, Olivier Favez, Frédérik Meleux, Laura Chiappini, Martial Haeffelin, Yohann Morille, Laure Malherbe, Arnaud Papin, Bertrand Bessagnet, Laurent Menut, Eva Leoz, and Laurence Rouïl. Assessing in near real time the impact of the april 2010 eyjafjallajökull ash plume on air quality. *Atmospheric Environment*, 45(5):1217–1221, 2011. ISSN 1352-2310. doi: https://doi.org/10.1016/j.atmosenv.2010.09.064.

R. Courant, K. Friedrichs, and H. Lewy. Über die partiellen Differenzengleichungen der mathematischen Physik. *Mathematische Annalen*, 100:32–74, January 1928. doi: 10.1007/BF01448839.

E. Debayle and Malcolm Sambridge. Inversion of massive surface wave data sets: Model construction and resolution assessment. *Journal of Geophysical Research-Solid Earth*, 109, 02 2004. doi: 10.1029/2003JB002652.

R. Descartes. *La Géométrie*. 1637.

Bruno Després and Frédéric Lagoutière. Un schéma non linéaire anti-dissipatif pour l'équation d'advection linéaire. *Comptes Rendus de l'Académie des Sciences - Series I - Mathematics*, 328(10):939 – 943, 1999. ISSN 0764-4442. doi: https://doi.org/10.1016/S0764-4442(99)80301-2. URL `http://www.sciencedirect.com/science/article/pii/S0764444299803012`.

L. J. Donner, B. L. Wyman, R. S. Hemler, L. W. Horowitz, Y. Ming, M. Zhao, J.-C. Golaz, P. Ginoux, S.-J. Lin, M. D. Schwarzkopf, J. Austin, G. Alaka, W. F. Cooke, T. L. Delworth, S. M. Freidenreich, C. T. Gordon, S. M. Griffies, I. M. Held, W. J. Hurlin, S. A. Klein, T. R. Knutson, A. R. Langenhorst, H.-C. Lee, Y. Lin, B. I. Magi, S. L. Malyshev, P. C. D. Milly, V. Naik, M. J. Nath, R. Pincus, J. J. Ploshay, V. Ramaswamy, C. J. Seman, E. Shevliakova, J. J. Sirutis, W. F. Stern, R. J. Stouffer, R. J. Wilson, M. Winton, A. T. Wittenberg, and F. Zeng. The dynamical core, physical parameterizations, and basic simulation characteristics of the atmospheric component am3 of the gfdl global coupled model cm3. *Journal of Climate*, 24(13):3484 – 3519, 2011. doi: 10.1175/2011JCLI3955.1. URL `https://journals.ametsoc.org/view/journals/clim/24/13/2011jcli3955.1.xml`.

Qiang Du, Vance Faber, and Max Gunzburger. Centroidal voronoi tessellations: Applications and algorithms. *Siam Review - SIAM REV*, 41:637–676, 12 1999. doi: 10.1137/S0036144599352836.

Qiang Du, Max D. Gunzburger, and Lili Ju. Voronoi-based finite volume methods, optimal voronoi meshes, and pdes on the sphere. *Computer Methods in Applied Mechanics and Engineering*, 192(35):3933–3957, 2003. ISSN 0045-7825. doi: https://doi.org/10.1016/S0045-7825(03)00394-3. URL `https://www.sciencedirect.com/science/article/pii/S0045782503003943`.

S. Dubey, T. Dubos, F. Hourdin, and H. C. Upadhyaya. On the inter-comparison of two tracer transport schemes on icosahedral grids. *Applied Mathematical Modelling*, 39(16):4828 – 4847, 2015. ISSN 0307-904X. doi: https://doi.org/10.1016/j.apm.2015.04.015. URL `http://www.sciencedirect.com/science/article/pii/S0307904X15002516`.

T. Dubos, S. Dubey, M. Tort, R. Mittal, Y. Meurdesoif, and F. Hourdin. DYNAMICO-1.0, an icosahedral hydrostatic dynamical core designed for consistency and versatility. *Geoscientific Model Development*, 8(10):3131–3150, 2015. doi: 10.5194/gmd-8-3131-2015. URL `https://www.geosci-model-dev.net/8/3131/2015/`.

John K. Dukowicz and John W. Kodis. Accurate conservative remapping (rezoning) for arbitrary lagrangian-eulerian computations. *SIAM Journal on Scientific and Statistical Computing*, 8(3):305–321, 1987. doi: 10.1137/0908037. URL `https://doi.org/10.1137/0908037`.

S. D. Eastham and D. J. Jacob. Limits on the ability of global eulerian models to resolve intercontinental transport of chemical plumes. *Atmospheric Chemistry and Physics*, 17(4):2543–2553, 2017. doi: 10.5194/acp-17-2543-2017. URL `https://www.atmos-chem-phys.net/17/2543/2017/`.

ECMWF. Numerical methods. `https://www.ecmwf.int/node/16948`, 2002.

G. E. Fasshauer. *Meshfree approximation methods with MATLAB*, volume 6. World Scientific, 2007. URL `https://www.worldscientific.com/worldscibooks/10.1142/6437`.

Vladimir Florinski, Dinshaw Balsara, Sudip Garain, and Katharine Gurski. Technologies for supporting high-order geodesic mesh frameworks for computational astrophysics and space sciences. *Computational Astrophysics and Cosmology*, 7, 03 2020. doi: 10.1186/s40668-020-00033-7.

S. R. Freitas, L. F. Rodrigues, K. M. Longo, and J. Panetta. Impact of a monotonic advection scheme with low numerical diffusion on transport modeling of emissions from biomass burning. *Journal of Advances in Modeling Earth Systems*, 3:1–26, 2011. doi: 10.1029/2011MS000084. URL `https://www.geosci-model-dev.net/8/3131/2015/`.

J. W. Gibbs, H. A. Bumstead, and R. G. Van Name. *Scientific papers of J. Willard Gibbs*. Longmans, Green and co., 1906. URL `//catalog.hathitrust.org/Record/001477418`.

S. K. Godunov. A difference method for numerical calculation of discontinuous solutions of the equations of hydrodynamics. *Mat. Sb., Nov. Ser.*, 47:271–306, 1959.

E. Hairer. *Solving ordinary differential equations II: stiff and differential-algebraic problems*. Springer series in computational mathematics 14. Springer, Berlin, second revised edition. edition, 1996. ISBN 3-540-60452-9.

D. A. Hauglustaine, F. Hourdin, L. Jourdain, M.-A. Filiberti, S. Walters, J.-F. Lamarque, and E. A. Holland. Interactive chemistry in the laboratoire de météorologie dynamique general circulation model: Description and background tropospheric chemistry evaluation. *Journal of Geophysical Research: Atmospheres*, 109(D4), 2004. doi: https://doi.org/10.1029/2003JD003957. URL `https://agupubs.onlinelibrary.wiley.com/doi/abs/10.1029/2003JD003957`.

J.A. Herrick and R. Wunderman. Report on puyehue-cordon caulle (chile). *Bulletin of the Global Volcanism Network*, 38(9), 2013. URL `https://doi.org/10.5479/si.GVP.BGVN201309-357150`.

F. Hourdin and A. Armengaud. The Use of Finite-Volume Methods for Atmospheric Advection of Trace Species. Part I: Test of Various Formulations in a General Circulation Model. *Mon. Weather Rev.*, 127:822–837, 1999. doi: 10.1175/1520-0493(1999)127⟨0822:TUOFVM⟩2.0.CO;2.

F. Hourdin, I. Musat, S. Bony, P. Braconnot, F. Codron, J.-L. Dufresne, L. Fairhead, M.-A. Filiberti, P. Friedlingstein, J.-Y. Grandpeix, G. Krinner, P. Levan, Z.-X. Li, and F. Lott. The LMDZ4 general circulation model: climate performance and sensitivity to parametrized physics with emphasis on tropical convection. *Climate Dynamics*, 19:3445–3482, August 2006. doi: 10.1007/s00382-006-0158-0. URL `https://hal.archives-ouvertes.fr/hal-00113202`.

A. Kasahara. Computational aspects of numerical models for weather prediction and climate simulation. 17:1–66, 1977.

Sergey Khaykin, Bernard Legras, Silvia Bucci, Pasquale Sellitto, Lars Isaksen, Florent Tencé, Slimane Bekki, Adam Bourassa, Landon Rieger, Daniel Zawada, Julien Jumelet, and Sophie Godin-Beekmann. The 2019/20 Australian wildfires generated a persistent smoke-charged vortex rising up to 35 km altitude. *Communications Earth & Environment*, 1(1):22, September 2020. ISSN 2662-4435. doi: 10.1038/s43247-020-00022-5.

Lars Klüser, Thilo Erbertseder, and Julian Meyer-Arnek. Observation of volcanic ash from puyehue-cordón caulle with iasi. *Atmospheric Measurement Techniques Discussions*, 5:4249–4283, 06 2012. doi: 10.5194/amtd-5-4249-2012.

M. Kramer, D. Heinzeller, Hartmann, W. van den Berg, and G.-J Steeneveld. Assessment of mpas variable resolution simulations in the grey-zone of convection against wrf model results and observations. *Clim. Dyn.*, 55:253–276, 2020. doi: 10.1007/s00382-018-4562-z.

M. Lachatre, S. Mailler, L. Menut, S. Turquety, P. Sellitto, H. Guermazi, G. Salerno, T. Caltabiano, and E. Carboni. New strategies for vertical transport in chemistry transport models: application to the case of the mount etna eruption on 18 march 2012 with chimere v2017r4. *Geoscientific Model Development*, 13(11):5707–5723, 2020. doi: 10.5194/gmd-13-5707-2020. URL `https://gmd.copernicus.org/articles/13/5707/2020/`.

P. Lauritzen and J. Thuburn. Evaluating transport schemes using interrelated tracers, scatter plots and numerical mixing diagnostics. *AGU Fall Meeting Abstracts*, 138:0170–, 04 2012. doi: 10.1002/qj.986.

P. Lauritzen, W. Skamarock, M. Prather, and M. Taylor. A standard test case suite for two-dimensional linear transport on the sphere. *Geoscientific Model Development*, 5:887–901, 06 2012. doi: 10.5194/gmd-5-887-2012.

H. Le Treut, Z.-X. Li, and M. Forichon. Sensitivity of the lmd general circulation model to greenhouse forcing associated with two different cloud water parameterizations. *Journal of Climate*, 7:1827–1841, 1994.

H. Le Treut, M. Forichon, O. Boucher, and Z.-X. Li. Sulfate aerosol indirect effect and co2 greenhouse forcing: Equilibriumresponse of the lmd gcm and associated cloud feedbacks. *Journal of Climate*, 11:1673–1684, 1998.

G. W. Leibniz. Nova Methodus pro Maximis et Minimi. *Acta Eruditorum*, pages 467–473, 1684.

G. W. Leibniz. Supplementum Geometrie Dimensoriæ. *Acta Eruditorum*, pages 385–391, 1693.

Shian-Jiann Lin and Richard B. Rood. Multidimensional flux-form semi-lagrangian transport schemes. *Monthly Weather Review*, 124(9):2046 – 2070, 1996. doi: 10.1175/1520-0493(1996)124⟨2046:MFFSLT⟩2.0.CO;2. URL `https://journals.ametsoc.org/view/journals/mwre/124/9/1520-0493_1996_124_2046_mffslt_2_0_co_2.xml`.

S. Mailler, L. Menut, D. Khvorostyanov, M. Valari, F. Couvidat, G. Siour, S. Turquety, R. Briant, P. Tuccella, B. Bessagnet, A. Colette, L. Létinois, K. Markakis, and F. Meleux. CHIMERE-2017: from urban to hemispheric chemistry-transport modeling. *Geoscientific Model Development*, 10(6):2397–2423, 2017. doi: 10.5194/gmd-10-2397-2017. URL `https://gmd.copernicus.org/articles/10/2397/2017/`.

S. Mailler, R. Pennel, L. Menut, and M. Lachâtre. Using the després and lagoutière (1999) antidiffusive transport scheme: a promising and novel method against excessive vertical diffusion in chemistry-transport models. *Geoscientific Model Development*, 14(4):2221–2233, 2021. doi: 10.5194/gmd-14-2221-2021. URL `https://gmd.copernicus.org/articles/14/2221/2021/`.

J. Meloen, P. Siegmund, P. Velthoven, H. Kelder, M. Sprenger, H. Wernli, A. Kentarchos, G.-J Roelofs, J. Feichter, C. Land, C. Forster, A. Stohl, W. Collins, and P. Cristofanelli. Stratosphere-troposphere exchange: A model and method intercomparison. *Journal of Geophysical Research Atmospheres*, 108, 06 2003. doi: 10.1029/2002JD002274.

L. Menut, B. Bessagnet, D. Khvorostyanov, M. Beekmann, N. Blond, A. Colette, I. Coll, G. Curci, G. Foret, A. Hodzic, S. Mailler, F. Meleux, J.-L. Monge, I. Pison, G. Siour, S. Turquety, M. Valari, R. Vautard, and M. G. Vivanco. CHIMERE 2013: a model for regional atmospheric composition modelling. *Geoscientific Model Development*, 6(4):981–1028, 2013. doi: 10.5194/gmd-6-981-2013. URL `https://gmd.copernicus.org/articles/6/981/2013/`.

D. R. Nair and P. H. Lauritzen. A class of deformational flow test cases for linear transport problems on the sphere. *Journal of Computational Physics*, 229(23):8868 – 8887, 2010. ISSN 0021-9991. doi: https://doi.org/10.1016/j.jcp.2010.08.014. URL `http://www.sciencedirect.com/science/article/pii/S0021999110004511`.

I. Newton. *De Methodis Serierum et Fluxionum*. London - H. Woodfall, 1736.

J. S. Perez Guerrero, L. C. G. Pimentel, T. H. Skaggs, and M. T. van Genuchten. Analytical solution of the advection–diffusion transport equation using a change-of-variable and integral transform technique. *International Journal of Heat and Mass Transfer*, 52(13):3297–3304, 2009. ISSN 0017-9310. doi: https://doi.org/10.1016/j.ijheatmasstransfer.2009.02.002. URL `https://www.sciencedirect.com/science/article/pii/S0017931009000817`.

Michael J. Prather. Numerical advection by conservation of second-order moments. *Journal of Geophysical Research: Atmospheres*, 91(D6):6671–6681, 1986. doi: https://doi.org/10.1029/JD091iD06p06671. URL `https://agupubs.onlinelibrary.wiley.com/doi/abs/10.1029/JD091iD06p06671`.

Graciela Raga, Darrel Baumgardner, Ana Ulke, Marcela Torres Brizuela, and Beata Kucienska. The environmental impact of the puyehue-cordon caulle 2011 volcanic eruption on buenos aires. *Natural Hazards and Earth System Sciences*, 1:1507–1534, 04 2013. doi: 10.5194/nhessd-1-1507-2013.

S. A. Rauscher and T. D. Ringler. Impact of variable-resolution meshes on midlatitude baroclinic eddies using CAM-MPAS-A. *Monthly Weather Review*, 142(11):4256 – 4268, 2014. doi: 10.1175/MWR-D-13-00366.1. URL `https://journals.ametsoc.org/view/journals/mwre/142/11/mwr-d-13-00366.1.xml`.

T.D. Ringler, J. Thuburn, J.B. Klemp, and W.C. Skamarock. A unified approach to energy conservation and potential vorticity dynamics for arbitrarily-structured c-grids. *Journal of Computational Physics*, 229(9):3065–3090, 2010.

ISSN 0021-9991. doi: https://doi.org/10.1016/j.jcp.2009.12.007. URL `https://www.sciencedirect.com/science/article/pii/S0021999109006780`.

Maria Ripodas, Almut Gassmann, J. Forstner, D. Majewski, Marco Giorgetta, P. Korn, Luis Kornblueh, Hui Wan, G. Zangl, Luca Bonaventura, and Thomas Heinze. Icosahedral shallow water model (icoswm): results of shallow water test cases and sensitivity to model parameters. *Geoscientific Model Development, v.2, 231-251 (2009)*, 2, 12 2009. doi: 10.5194/gmdd-2-581-2009.

Alan Robock. Volcanic eruptions and climate. *Reviews of Geophysics*, 38(2):191–219, 2000. doi: https://doi.org/10.1029/1998RG000054. URL `https://agupubs.onlinelibrary.wiley.com/doi/abs/10.1029/1998RG000054`.

C. Ronchi, R. Iacono, and P.S. Paolucci. The “cubed sphere”: A new method for the solution of partial differential equations in spherical geometry. *Journal of Computational Physics*, 124(1):93–114, 1996. ISSN 0021-9991. doi: https://doi.org/10.1006/jcph.1996.0047. URL `https://www.sciencedirect.com/science/article/pii/S0021999196900479`.

R. Sadourny. Compressible model flows on the sphere. *Journal of the Atmospheric Sciences*, 32:2103–2110, 1975a.

R. Sadourny and K. Laval. *January and July performance of the LMD general circulation model. In: Berger, A. and Nicolis, C. (eds) New perspectives in climate modeling.*, page 173–197. Elsevier, 1984. ISBN 0444422951 (U.S). doi: https://doi.org/10.1002/joc.3370040513.

R. Sadourny, A. Arakawa, and Y. Mintz. Integration of the nondivergent barotropic vorticity equation with an icosahedral-hexagonal grid for the sphere. *Monthly Weather Review*, 96(6):351 – 356, 1968. doi: 10.1175/1520-0493(1968)096⟨0351:IOTNBV⟩2.0.CO;2. URL `https://journals.ametsoc.org/view/journals/mwre/96/6/1520-0493_1968_096_0351_iotnbv_2_0_co_2.xml`.

Robert Sadourny. Conservative finite-difference approximations of the primitive equations on quasi-uniform spherical grids. *Monthly Weather Review*, 100(2):136 – 144, 1972. doi: 10.1175/1520-0493(1972)100⟨0136:CFAOTP⟩2.3.CO;2. URL `https://journals.ametsoc.org/view/journals/mwre/100/2/1520-0493_1972_100_0136_cfaotp_2_3_co_2.xml`.

Robert Sadourny. The dynamics of finite-difference models of the shallow-water equations. *Journal of Atmospheric Sciences*, 32(4):680 – 689, 1975b. doi: 10.1175/1520-0469(1975)032⟨0680:TDOFDM⟩2.0.CO;2. URL `https://journals.ametsoc.org/view/journals/atsc/32/4/1520-0469_1975_032_0680_tdofdm_2_0_co_2.xml`.

M. Satoh, Hirofumi Tomita, Hisashi Yashiro, Hiroaki Miura, Chihiro Kodama, Tatsuya Seiki, Akira T Noda, Yohei Yamada, Daisuke Goto, Masahiro Sawada, Takemasa Miyoshi, Yosuke Niwa, Masayuki Hara, Tomoki Ohno, Shin ichi Iga, Takashi Arakawa, Takahiro Inoue, and Hiroyasu Kubokawa. The non-hydrostatic icosahedral atmospheric model: description and development. *Prog. in Earth and Planet. Sci.*, 1, 2014a. doi: 10.1186/s40645-014-0018-1.

Masaki Satoh, Hirofumi Tomita, Hisashi Yashiro, Hiroaki Miura, Chihiro Kodama, Tatsuya Seiki, Akira Noda, Yohei Yamada, Daisuke Goto, Masahiro Sawada, Takemasa Miyoshi, Yosuke Niwa, Masayuki Hara, Tomoki Ohno, Shin-ichi Iga, Takashi Arakawa, Takahiro Inoue, and Hiroyasu Kubokawa. The non-hydrostatic icosahedral atmospheric model: description and development. *Progress in Earth and Planetary Science*, 1:18, 10 2014b. doi: 10.1186/s40645-014-0018-1.

J. H. Seinfeld and S. N. Pandis. *Atmospheric chemistry and physics: From air pollution to climate change*. Wiley-Interscience, 1997.

B. Sič, L. El Amraoui, V. Marecal, B. Josse, J. Arteta, J. Guth, M. Joly, and P. Hamer. Modelling of primary aerosols in the chemical transport model mocage: development and evaluation of aerosol physical parameterizations. *Geoscientific Model Development*, 8, 02 2015. doi: 10.5194/gmd-8-381-2015.

W. C. Skamarock, J. B. Klemp, M. G. Duda, L. D. Fowler, S.-H. Park, and T. D. Ringler. A multiscale nonhydrostatic atmospheric model using centroidal voronoi tesselations and C-grid staggering. *Monthly Weather Review*, 140(9): 3090 – 3105, 2012. doi: 10.1175/MWR-D-11-00215.1. URL `https://journals.ametsoc.org/view/journals/mwre/140/9/mwr-d-11-00215.1.xml`.

William C. Skamarock and Almut Gassmann. Conservative transport schemes for spherical geodesic grids: High-order flux operators for ode-based time integration. *Mon. Weather Rev.*, 2011. doi: 10.1175/MWR-D-10-05056.1.

William C. Skamarock, Michael G. Duda, Soyoung Ha, and Sang-Hun Park. Limited-area atmospheric modeling using an unstructured mesh. *Mon. Weather Rev.*, 2018. doi: 10.1175/MWR-D-18-0155.1.

Ivan Suarez, Chad Leidy, Gabriel Téllez, Guillaume Gay, and Andres Gonzalez Mancera. Slow sedimentation and deformability of charged lipid vesicles. *PloS one*, 8:e68309, 07 2013. doi: 10.1371/journal.pone.0068309.

Christiane Textor, Hans-F. Graf, Claudia Timmreck, and Alan Robock. Emissions from volcanoes. In Claire Granier, Paulo Artaxo, and Claire E. Reeves, editors, *Emissions of Atmospheric Trace Compounds*, pages 269–303, Dordrecht, 2004. Springer Netherlands. ISBN 978-1-4020-2167-1.

J. Thuburn, T. D. Ringler, W. C. Skamarock, and J. B. Klemp. Numerical representation of geostrophic modes on arbitrarily structured c-grids. *Journal of Computational Physics*, 228(22):8321–8335, 2009. ISSN 0021-9991. doi: https://doi.org/10.1016/j.jcp.2009.08.006. URL `https://www.sciencedirect.com/science/article/pii/S0021999109004434`.

J. Thuburn, C. J. Cotter, and T. Dubos. A mimetic, semi-implicit, forward-in-time, finite volume shallow water model: comparison of hexagonal–icosahedral and cubed-sphere grids. *Geoscientific Model Development*, 7(3):909–929, 2014. doi: 10.5194/gmd-7-909-2014. URL `https://gmd.copernicus.org/articles/7/909/2014/`.

Hirofumi Tomita. A stretched icosahedral grid by a new grid transformation. *Journal of the Meteorological Society of Japan*, pages 107–119, 2008.

S Twomey. *Atmospheric aerosols*. Elsevier Science Pub Co, 1977. URL `https://www.osti.gov/biblio/6747246`.

Paul Ullrich. A global finite-element shallow-water model supporting continuous and discontinuous elements. *Geoscientific Model Development*, 7, 12 2014. doi: 10.5194/gmd-7-3017-2014.

Alfred Uwitonze, Jiaqing Huang, Yuanqing Ye, Wenqing Cheng, and Zongpeng Li. Exact and heuristic algorithms for space information flow. *PLOS ONE*, 13:e0193350, 03 2018. doi: 10.1371/journal.pone.0193350.

T. Vadsaria, L. Li, G. Ramstein, and J.-C. Dutay. Development of a sequential tool, lmdz-nemo-med-v1, to conduct global-to-regional past climate simulation for the mediterranean basin: an early holocene case study. *Geoscientific Model Development*, 13(5):2337–2354, 2020. doi: 10.5194/gmd-13-2337-2020. URL `https://gmd.copernicus.org/articles/13/2337/2020/`.

B. Van Leer. Towards the ultimate conservative difference scheme. iv. a new approach to numerical convection. *Journal of Computational Physics*, 23(3):276 – 299, 1977. ISSN 0021-9991. doi: https://doi.org/10.1016/0021-9991(77)90095-X. URL `http://www.sciencedirect.com/science/article/pii/002199917790095X`.

C. J. Walcek. Minor flux adjustment near mixing ratio extremes for simplified yet highly accurate monotonic calculation of tracer advection. *Journal of Geophysical Research*, 105:9335–9348, 04 2000. doi: 10.1029/1999JD901142.

Ning Wang and Jin-Luen Lee. Geometric properties of the icosahedral-hexagonal grid on the two-sphere. *SIAM Journal on Scientific Computing*, 33(5):2536–2559, 2011. doi: 10.1137/090761355. URL `https://doi.org/10.1137/090761355`.

H. Weller, H. G. Weller, and A. Fournier. Voronoi, delaunay, and block-structured mesh refinement for solution of the shallow-water equations on the sphere. *Monthly Weather Review*, 137(12):4208 – 4224, 2009. doi: 10.1175/2009MWR2917.1.

David L. Williamson. The evolution of dynamical cores for global atmospheric models. *Journal of the Meteorological Society of Japan. Ser. II*, 85B:241–269, 2007. doi: 10.2151/jmsj.85B.241.

T. Zheng, S. Feng, K. J. Davis, S. Pal, and J.-A. Morguí. Development and evaluation of co_2 transport in mpas-a v6.3. *Geoscientific Model Development*, 14(5):3037–3066, 2021. doi: 10.5194/gmd-14-3037-2021.

Y. Zhou, Y. Zhang, J. Li, R. Yu, and Z. Liu. Configuration and evaluation of a global unstructured mesh atmospheric model (grist-a20.9) based on the variable-resolution approach. *Geoscientific Model Development*, 13(12):6325–6348, 2020. doi: 10.5194/gmd-13-6325-2020. URL `https://gmd.copernicus.org/articles/13/6325/2020/`.

J. Zhuang, D. J. Jacob, and S. D. Eastham. The importance of vertical resolution in the free troposphere for modeling intercontinental plumes. *Atmospheric Chemistry and Physics*, 18(8):6039–6055, 2018. doi: 10.5194/acp-18-6039-2018. URL `https://www.atmos-chem-phys.net/18/6039/2018/`.

C. Zoppou and J. H. Knight. Analytical solutions for advection and advection-diffusion equations with spatially variable coefficients. *Journal of Hydraulic Engineering*, 123(2):144–148, 1997. doi: 10.1061/(ASCE)0733-9429(1997)123:2(144). URL `https://ascelibrary.org/doi/abs/10.1061/`.

Nomenclature

Physical Quantities

α	Tilt angle	m
$\mathcal{N}$	Set of cell vertices	unitless
Φ	Tracer concentration	kg/m^3
ϕ	Tracer mixing ratio	unitless
Ψ	Stream function	m^2/s
ρ	Fluid density	kg/m^3
A	Area	m^2
a	Planetary radius	m
b	Background mixing ratio	unitless
C	Courant number	unitless
c	Cosine-bell maximum contribution to mixing ratio	unitless
E_k	Set of cell edges	unitless
K	Amplitude of vortical flow	m/s
l, d	Length	m
n	Edge orientation	unitless, ± 1
R	Cosine-bell radius	rad
S	Entropy	kg/m
U	Scale of flow speed	m/s
u	Zonal speed	m/s
V	Control volume	

v	Meridional speed	m/s

Vector Quantities

$\boldsymbol{e_r}$	Unit vector along the radial axis	
$\boldsymbol{e_x}$	Unit vector along the x Cartesian axis	
$\boldsymbol{e_y}$	Unit vector along the y Cartesian axis	
$\boldsymbol{e_\alpha}$	Unit vector along the tilted rotation axis	
$\boldsymbol{G}$	Gradient vectors	
$\boldsymbol{n}$	Normal vectors	
$\boldsymbol{u}$	Fluid velocity	m/s
$\boldsymbol{x}$	Position vectors	
Γ	Perimeter of a dual cell	

Indices

crit	critical	subscript
SB	Solid-body part	subscript
vortex	Vortex part	subscript
e	Current cell edge	subscript
i	Arbitrary cell index	subscript
j	Arbitrary cell index	subscript
k	Current cell index	subscript
n	Current time step	superscript
p	Order of accuracy	superscript
v	Volumic	subscript

Functions and Operators

∂_t	operator for the partial derivative with respect to time, $\frac{\partial}{\partial t}$	
f	Arbitrary function	
h	Shape function	

Coordinates

λ	Longitude	rad
θ	Latitude	rad

Acronyms

CFL Courant-Friedrichs-Lewy. 25

CTM chemistry transport model. 25, 26, 28, 29, 42, 83, 87, 89, 98, 101–103

DOFs degrees of freedom. 35

GCM general circulation model. 26–28, 89, 98, 102

GCMs general circulation models. 19

GCS Geographic Coordinate System. 17

INCA Interaction with Chemistry and Aerosols. 26

IVP initial-value problem. 35, 38

LMD Laboratoire de Météorologie Dynamique. 26

LMDZ Laboratoire de Météorologie Dynamique–Zoom. 22, 26, 27

LSCE Laboratoire des Science du Climat et de l'Environment. 26

MOCAGE *Modèle de Chimie Atmosphérique de Grande Echelle*. 25

MPAS Model for Prediction Across Scales. 27, 28, 103

NICAM Non-hydrostatic Icosahedral Atmospheric Model. 27

ODEs ordinary differential equations. 38

PDE partial differential equation. 16, 38

ppb parts per billion. 15

PPM Piece-wise Parabolic Method. 26, 43, 64, 66, 84, 101–103

RMSE root-mean-square error. 55, 56, 80, 81, 83–85

SLFV Semi-Lagrangian Finite-Volume. 41–43, 83, 84, 90, 101, 102

ECOLE
DOCTORALE

Titre : Vers le Transport Multi-Échelles de Panaches Fins

Mots clés : Modélisation numérique, maillage, modèle de chimie-transport, atmosphère, DYNAMICO, CHIMERE

Résumé : La distribution d’aérosols et de gaz trace dans l’atmosphère résulte de l’émission d’espèces gazeuses et particulaires primaires, ainsi que de leur transport, de leur sédimentation et de leurs transformations (photo)chimiques. La modélisation de ces processus dans l’atmosphère peut s’aborder au travers de modèles de chimie-transport d’échelle globale ou régionale.

Le modèle CHIMERE, développé en grande partie au LMD [Mailler et al., 2017], est un modèle de chimie-transport régional, récemment étendu aux échelles hémisphériques, qui permet d’aborder ces phénomènes sur une grande gamme d’échelles, allant de l’échelle d’une ville à celle d’un hémisphère. Il est toutefois difficile d’utiliser ce modèle pour représenter les interactions entre phénomènes de petite échelle (pollution de la couche limite urbaine) et de grande échelle (transport à l’échelle continentale ou hémisphérique) de panaches fins de gaz et d’aérosols, issus par exemple d’émissions de panaches volcaniques, de feux de forêt, ou d’aérosols désertiques. Cette limitation est un effet de l’impossibilité d’utiliser le modèle sous sa forme actuelle avec un domaine à maille non structurée, seul type de maillage permettant une réelle variation de la résolution en fonction de zones d’intérêt définies par le modélisateur (zones urbaines, zones d’émission). Cette limitation est commune à la totalité des modèles de chimie-transport existants à l’heure actuelle, pouvoir la lever serait donc un important pas en avant pour la compréhension des interactions d’échelle dans le domaine de la chimie atmosphérique.

Une façon de lever ces limitations serait de remplacer le maillage cartésien de CHIMERE par un maillage non-structuré. En effet les maillages non-structurés permettent de faire varier la résolution dans l’espace et de concentrer les ressources de calcul dans les quelques régions clés (p.ex. près d’une éruption volcanique) où une haute résolution spatiale est réellement nécessaire. Introduire une telle flexibilité multi-échelle représenterait un pas important pour la modélisation des interactions d’échelles en chimie atmosphérique, et permettrait potentiellement des percées dans la compréhension de ces interactions.

DYNAMICO, le modèle de circulation générale atmosphérique développé récemment au LMD et au LSCE [Dubos et al., 2015] est basé sur des maillages de Voronoi non-structurés sphériques. L’objectif de cette thèse est de contribuer à l’évaluation de méthods numériques empruntées à DYNAMICO pour le transport à grand échelle de panaches fins. A cette fin nous comparons la performance numérique de schémas de transport formulés sur maillage non-structuré [Dubey et al., 2015] à celle de schémas similaires formulés sur un maillage cartésien sphérique évitant les pôles. Des schémas d’ordre varié et avec différents intégrations temporelles sont implémentés pour chacun des deux types de maillage. Un jeu de cas-test est utilisé pour évalué propriétés des paires maillage-schéma. Différentes métriques permettent d’étudier les propriétes de stabilité, monotonocité, convergence et diffusion numérique.

Alors que l’on pouvait s’attendre à une meilleure performance des schémas cartésiens par rapport à aux schémas non-structurés de complexité similaire, nous trouvons qu’un schéma de la famille des schémas de Van Leer a une performance comparable à un schéma similaire sur maillage cartésien, schéma qui est proposé par défaut par le modèle CHIMERE de façon opérationnelle. Au-delà de ces expériences numériques bidimensionnelles idéalisées, nous comparons la performance de ces deux schémas dans un contexte tridimensionnel réaliste inspiré de l’éruption du volcan Puyehue en 2011. Ce nécessaire jalon doit être complété par des expérience à résolution variable pour mener à une évaluation complète des mérites de la modélisation multi-échelles pour les applications en chimie-transport.

Title: Towards Multi-Scale Transport of Sharp Plumes

Keywords: Numerical modeling, meshes, chemistry-transport model, atmosphere, DYNAMICO, CHIMERE

Abstract: The distribution of aerosols and trace gases in the atmosphere results from the emission of primary gaseous and particulate matter, their transport, sedimentation and (photo-)chemical transformations. Understanding and quantifying these processes in the atmosphere can be addressed through the use of global- or regional-scale chemistry-transport numerical models.

CHIMERE is a chemistry-transport model developed mainly at LMD [Mailler et al., 2017]. Initially targeted to urban and regional scales, it was recently extended to hemispheric scales in order to address these processes on a wider range. While theoretically possible, it is impractical to use this model to represent interactions between small-scale processes (e.g. pollution in the urban atmospheric boundary layer) and large-scale processes (e.g. intercontinental transport) controlling sharp plumes of gas and aerosols, resulting for instance from massive emissions by volcanic eruptions, forest fires and desert aerosol tempests. Indeed such studies requiring both large domains and high resolution have a prohibitive numerical cost due to the formulation of CHIMERE on a regular Cartesian mesh. This limitation is shared by all currently operational chemistry-transport models (CTMs). Additionally, traditional Cartesian longitude-latitude meshes pose a numerical singularity at the poles, where the longitude lines converge.

One way to lift these limitations would be to replace CHIMERE’s Cartesian mesh by a fully unstructured mesh. Unstructured meshes support variable resolution in space, allowing computational resources to be focused in those few key regions (e.g. volcanic eruption) where high spatial resolution is really required. Allowing such multi-scale capacity would be a significant step forward in the modelling of scale interactions in atmospheric chemistry, and would potentially allow breakthrough for the understanding of such interactions.

DYNAMICO, the atmospheric general circulation model recently developed at LMD and LSCE [Dubos et al., 2015] supports unstructured spherical Voronoi meshes. It is the goal of this PhD project to contribute to the assessment of the viability of numerical methods borrowed from DYNAMICO for large-scale transport of sharp plumes. To this end, we compare the numerical performance of transport schemes formulated on spherical unstructured meshes [Dubey et al., 2015] with schemes formulated on Cartesian spherical meshes avoiding the poles. Schemes of various order and different treatments of time integration are implemented in each mesh framework. A suite of test cases is used to evaluate different properties of the mesh-scheme pairings. Various metrics are used to study stability, monotonicity, convergence and numerical diffusion. While it could be anticipated that Cartesian schemes perform better than their unstructured counterpart of similar complexity, we find that a scheme of the Van Leer family on the unstructured mesh has a comparable performance to a similar scheme on a Cartesian mesh, which is the default scheme used operationally by CHIMERE. Beyond these idealized two-dimensional numerical experiments, we compare the performance of the two schemes in a realistic, three-dimensional setting mimicking the eruption of the Puyehue volcano in 2011. This necessary milestone is to be complemented by experiments with variable-resolution meshes leading to a full assessment of the merits of multi-scale-modelling chemistry-transport applications.

Institut Polytechnique de Paris
91120 Palaiseau, France